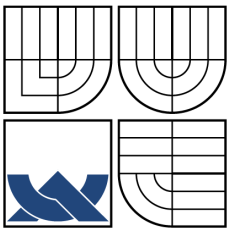

BRNO UNIVERSITY OF TECHNOLOGY
VYSOKÉ UČENÍ TECHNICKÉ V BRNĚ

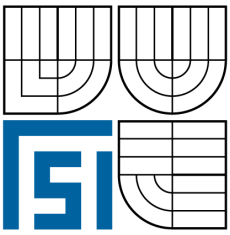

FACULTY OF MECHANICAL ENGINEERING
INSTITUTE OF PHYSICAL ENGINEERING

FAKULTA STROJNÍHO INŽENÝRSTVÍ
ÚSTAV FYZIKÁLNÍHO INŽENÝRSTVÍ

PLASMONIC ANTENNAS
PLAZMONICKÉ ANTÉNY

DOCTORAL THESIS
DISERTAČNÍ PRÁCE

AUTHOR
AUTOR PRÁCE

Ing. MICHAL KVAPIL

SUPERVISOR
VEDOUCÍ PRÁCE

prof. RNDr. TOMÁŠ ŠIKOLA, CSc.

BRNO 2015

Summary
This doctoral thesis deals with plasmonic antennas. The resonant properties of plasmonic antennas have been studied both theoretically and experimentally. Theoretical calculations have been made using the finite-difference time-domain numerical method in Lumerical FDTD Solutions software. For the experiments, antennas were fabricated by electron beam lithography. Resonant properties of the fabricated antennas have been studied by Fourier transform infrared spectroscopy. The thesis is aimed at the investigation of the resonant properties of plasmonic antennas, when situated on a film of nanocrystalline diamond. Also, the application of antennas as a plasmon-based sensor functionalized to streptavidin sensing has been investigated. Finally, an antenna with the shape of the letter V has been introduced. Due to the reduced symmetry of the V-antenna, the incident light of wavelength close to an antenna quadrupole mode is unidirectionally scattered.

Abstrakt
Tato disertační práce pojednává o plazmonických anténách. Rezonanční vlastnosti plazmonických antén jsou studovány teoreticky i experimentálně. Teoretické výpočty jsou prováděny v programu Lumerical FDTD Solutions užitím numerické metody konečných diferencí v časové doméně. Pro experimentální studium byly antény vyrobeny pomocí elektronové litografie. Rezonanční vlastnosti vyrobených antén jsou studovány fourierovskou infračervenou spektroskopií. Práce se zaměřuje na studium rezonančních vlastností antén vyrobených na vrstvě nanokrystalického diamantu. Dále zkoumá možnost využití antén jako plazmonického senzoru funkcionalizovaného k detekci streptavidinu. Nakonec je představena anténa tvaru písmene V, u které dochází v důsledku porušení symetrie antény ke směrovému rozptylu dopadajícího světla. Tato směrovost se ovšem projevuje jen na vlnových délkách blízkých kvadrupólovému módu antény.

Keywords
plasmonic antennas, nanocrystalline diamond, functionalization, unidirectional antennas

Klíčová slova
plazmonické antény, nanokrystalický diamant, funkcionalizace, směrové antény

KVAPIL, M. *Plasmonic Antennas.* Brno: Brno University of Technology, Faculty of Mechanical Engineering, Institute of Physical Enginnering, 2015. Doctoral thesis. 104 p. Supervisor Prof. Tomáš Šikola.

Prohlašuji, že jsem tuto disertační práci vypracoval samostatně pod odborným vedením prof. RNDr. Tomáše Šikoly, CSc. a s použitím odborné literatury a dalších informačních zdrojů, které jsou uvedeny na konci práce v seznamu literatury.

Ing. Michal Kvapil

I would like to express my gratitude to my supervisor **Prof. Tomáš Šikola** for leading of the project. I want to give my dearest thanks to **Assoc. Prof. Radek Kalousek** and **Prof. Jiří Spousta** for consultations and valuable suggestions. My thanks also go to **Prof. Petr Dub** and **Dr. Vlastimil Křápek** for their comments on the text of this thesis. I also want to express my thanks to all other colleagues and friends from the plasmonic group of Institute of Physical Engineering for frequent discussions not only before, during and after the regular plasmonic meetings. Last but not least I thank **Dr. Lisa Vaccari** and **Dr. Loredana Casalis** from Elettra Synchrotron facility for the assistance with antennas fuctionalization and measurements and **Dr. Pieter Neutens** and **Dries Vercruysse** from IMEC research institute for the sample fabrication and assistance with experimental setup measurements and modifications. Finally, I must not forget to mention the great support I received during my studies from **Petra** and whole **my family**.

Ing. Michal Kvapil

Contents

1 Introduction

Plasmonics is a major part of the field of nanophotonics. It deals with the interaction of electromagnetic radiation with conduction electrons at metal-dielectric interfaces including spatially limited (localized) interfaces of metallic micro and nanostructures. When proper conditions are met, conduction electrons of metals respond collectively to the incoming radiation, oscillate collectively and transform incident spatial electromagnetic waves into surface electromagnetic waves.

Propagation of surface electromagnetic waves along the metal-dielectric interface was investigated as early as in 1900s [1], [2]. Quasi-particles corresponding to propagating surface electromagnetic waves are called surface plasmon polaritons (SPPs). They were first observed, albeit unknowingly as a significant *anomalous* drop in the intensity of light, by Wood in 1902 during light diffraction experiments with metallic gratings [3]. It took another 40 years until Fano connected Wood's observation with the excitation of surface electromagnetic waves [4]. Similar loss of signal intensity was also observed by Ritchie during experiments with electron diffraction at thin metallic foils [5]. Later, Ritchie also connected his observations with excitation of surface electromagnetic waves [6]. At the end of 1960s surface electromagnetic waves were excited at optical frequencies by a combination of prism coupling and frustrated total reflection [7], [8]. Since then, the research on SPPs has been conducted mainly in the visible region of the electromagnetic spectrum. Although it is more than 100 years since first discoveries in the field of SPPs, the real boom started around 2000, when micro and nanofabrication tools became widespread.

When the metal-dielectric interface is spatially limited to the dimensions below the wavelength of applied electromagnetic radiation, surface plasmons are confined to such limited interface; they are *localized*. The localized surface electromagnetic waves coupled to the conduction electron oscillations are called localized surface plasmons (LSPs). Upon the illumination, standing electromagnetic waves arise in these subwavelength structures which leads to significant resonant effects at specific wavelengths – the enhancement of electric field in close vicinity of the structures and the enhancement of the light scattered by the structure. The latter has been widely utilized, albeit without any deep understanding of this effect, for staining glass since the times of ancient Roman Empire.

When structures exhibit the resonance of LSP due to external illumination, the incident electromagnetic field is concentrated by the structure to a small zone around the structure. This feature makes them very similar to classical macroscopic electromagnetic antennas which are designed to concentrate the propagating electromagnetic radiation into a small and well confined space, where the power of radiation is either received or released by the antenna [9]. That is the reason why these resonant plasmonic structures are usually called *plasmonic antennas*.

In 1908 Gustav Mie published his seminal paper on light scattering and absorption by spherical metallic particles [10]. In the paper, Mie developed a complete analytical theory for the description of interaction of metallic sphere with incoming electromagnetic radiation and used this to solve one of the early 20^{th} century physical stumper – he managed to explain the colour of gold colloid particles. The size of gold nanoparticles exhibiting LSP resonance in the visible spectral region is between tens and approx. 180 nanometres

(detached from a substrate), so these dimensions were far below the resolution limit of the best available observation equipment of Mie's time – the bright field optical microscope (approx. 400 nm). So these particles remained hidden from direct observations. The only instrument which could make these particles visible was the *ultramicroscope*, the invention of Richard Zsigmondy, Henry Siedentopf and Zeiss Company. The observation part of this instrument was an ordinary microscope, the new approach was the way of sample illumination. Colloid particles were illuminated by a bright focused solar light beam coming perpendicularly to the direction of observation. The light scattered by the particles produced Airy disks, which were then seen in the observation microscope. By this method it was possible to register the presence of particles, but not to estimate their dimensions. An extreme caution had to be taken during experiments to prevent eye damage from sunlight coming into the observation microscope. However, in this way it was possible for the first time to detect the presence of particles as small as 4 nm [11]. Today, a slight modification of illumination configuration used in the ultramicroscope is common in optical microscopes and is known as the dark-field illumination.

The presented doctoral thesis deals with subwavelength plasmonic antennas. The work involves numerical computations and experimental studies of plasmonic antennas, their electromagnetic field in the near- and far-field as well as the description of fabrication techniques and used materials. This thesis is divided into several chapters. Fundamental theory of electromagnetic field which is presented in Chapter 2 is followed by the introduction of surface plasmon polaritons and localized surface plasmons in Chapters 3 and 4. Chapter 5 succeeds with the description of the finite-difference time-domain numerical method which has been used in numerical calculations of antennas resonant properties. Chapter 6 then deals with main experimental techniques which were used for the fabrication of plasmonic antennas and the following evaluation and measurements of their resonant properties. Also, the properties of all the substrates on which plasmonic antennas were fabricated are shortly discussed in this chapter. Author's work in the field of plasmonic is then shown in the following chapters. Chapter 7 is devoted to the study of influence of a nanocrystalline diamond thin film on the resonant properties of plasmonic antennas using numerical calculations. The functionalization of antennas for the purpose of biosensing application is shown in Chapter 8. Finally, a special type of antennas with reduced symmetry which results in directional light scattering is shown in Chapter 9.

2 Theory of electromagnetic field

In this chapter, the properties of electromagnetic field in the linear, isotropic and homogenous medium will be introduced. All, but quantum, electromagnetic phenomena can be described by a set of equations named after British physicist James Clerk Maxwell.

2.1 Maxwell's equations

Classical electromagnetic field can be described by Maxwell's equations which is a set of four equations, where two scalar equations describe the nature of electromagnetic field and other two vector equations describe time and spatial interdependence of the electric and magnetic component of electromagnetic field. We show the differential form of Maxwell's equations in matter:

$$\nabla \cdot \vec{D} = \rho_{\mathrm{f}}, \tag{2.1}$$

$$\nabla \cdot \vec{B} = 0, \tag{2.2}$$

$$\nabla \times \vec{E} = -\frac{\partial \vec{B}}{\partial t}, \tag{2.3}$$

$$\nabla \times \vec{H} = \vec{J}_{\mathrm{f}} + \frac{\partial \vec{D}}{\partial t}. \tag{2.4}$$

In these equations $\vec{E}$ represents the electric field, $\vec{B}$ magnetic induction, ρ_{f} and $\vec{J}_{\mathrm{f}}$ represent the density of free charge and the density of free current, respectively. The electric displacement $\vec{D}$ and magnetic field $\vec{H}$ are connected with $\vec{E}$ and $\vec{B}$ by following relations[1]:

$$\vec{D} = \varepsilon_0 \vec{E} + \vec{P}, \tag{2.5}$$

$$\vec{H} = \frac{1}{\mu_0}\vec{B} - \vec{M}, \tag{2.6}$$

where ε_0 and μ_0 are the vacuum permitivity[2] and permeability[3], respectively. Quantities $\vec{P}$ and $\vec{M}$ represent electric polarization[4] and magnetization[5]. Equations (2.5) and (2.6) presumes that higher order moments (e.g. quadrupole) are negligible in comparison with dipole moment. As the quantities $\vec{P}$ and $\vec{M}$ are connected with the medium under consideration, in free space (vacuum) these quantities vanishes.

Equations (2.1)–(2.6) must be also supplemented with the following constitutive relations[6]:

$$\vec{J}_{\mathrm{f}} = \sigma \vec{E}, \tag{2.7}$$

$$\vec{B} = \mu_0 \mu \vec{H}, \tag{2.8}$$

[1] Assuming instant response of the medium to the external field.
[2] $\varepsilon_0 \approx 8.854 \cdot 10^{-12}$ F $\cdot$ m^{-1}
[3] $\mu_0 \approx 1.257 \cdot 10^{-6}$ H $\cdot$ m^{-1}
[4] An average electric dipole moment per unit volume
[5] An average magnetic dipole moment per unit volume
[6] We still assume that the response of the medium to the external field is instant.

$$\vec{P} = \varepsilon_0 \chi \vec{E}, \tag{2.9}$$

where σ represents the electric conductivity, μ relative permeability and χ electric susceptibility. By inserting (2.9) into (2.5) we get

$$\vec{D} = \varepsilon_0(1+\chi)\vec{E} = \varepsilon_0 \varepsilon \vec{E}, \tag{2.10}$$

where $\varepsilon = 1 + \chi$ is relative permittivity, also called as dielectric constant or dielectric function.

In our assumption, the *proportional* coefficients σ, μ and χ depends on the medium under consideration, but otherwise they are independent of the field magnitudes, position and direction[7]. Now, using the procedure from [12, p. 13], we will now show that these coefficients cannot be considered independent of frequency.

Let us look closer on Equation (2.9). An isolated piece of matter is unpolarized ($\vec{P} = 0$). When placed into external electric field $\vec{E}$ which is assumed to be time-harmonic[8], the external field induces a net dipole moment and material becomes polarized ($\vec{P} \neq 0$). In this equation χ represents a material coefficient of proportion between electric field $\vec{E}$ and polarization $\vec{P}$, so χ may be interpreted as a response to the unit external (or driving) field. As it is known from the theory of mechanical harmonic oscillators, the response of the oscillator to the periodic driving force is frequency dependent. This piece of matter under consideration can be represented as a set of harmonic oscilators[9], therefore using this analogy, it is reasonable to assume that all material coefficients (σ, μ_r and χ) and also the material connected quantities as $\vec{P}$ and $\vec{M}$ are functions of frequency.

2.2 Time-harmonic electromagnetic field

General time-harmonic field $\vec{F}(\vec{r}, t)$ can be described as

$$\vec{F}(\vec{r}, t) = \vec{a}(\vec{r}) \cos \omega t + \vec{b}(\vec{r}) \sin \omega t, \tag{2.11}$$

where $\vec{r}$ is the position vector and ω angular frequency. Real vector amplitudes $\vec{a}(\vec{r})$ and $\vec{b}(\vec{r})$ are time-independent, but can depend on position. Time-harmonic field $\vec{F} = \vec{F}(\vec{r}, t)$ can also be expressed as a real part of complex vector $\vec{F} = \Re\{\vec{F}_\mathrm{c}\}$, where

$$\vec{F}_\mathrm{c} = \vec{c} \exp(-\mathrm{i}\omega t), \qquad \vec{c} = \vec{a} + \mathrm{i}\vec{b}. \tag{2.12}$$

Vector $\vec{F}_\mathrm{c}$ is a complex representation of real field $\vec{F}$. When all operations on this time-harmonic field are linear, then it is usually more convenient to work with its complex representation. Let $\mathcal{Q}$ be a linear operator. Then this operator $\mathcal{Q}$ can be applied on real vector field (2.11) by operating on its complex representation (2.12) and then considering the real part of the result, i.e.

[7] As it was stated above, the medium is considered linear, homogeneous and isotropic.
[8] This will be introduced in Section 2.2.
[9] As will be shown later in Section 2.5.

$$\mathcal{Q}\vec{F} = \mathcal{Q}\Re\{\vec{F}_{\mathrm{c}}\} = \Re\{\mathcal{Q}\vec{F}_{\mathrm{c}}\} \tag{2.13}$$

Vector field [Eq. (2.11)] can also be expressed as $\vec{F} = \Re\{\vec{F}_{\mathrm{c}}^{*}\}$, where $\vec{F}_{\mathrm{c}}^{*} = \vec{c}^{*}\exp(\mathrm{i}\omega t)$ and $\vec{c}^{*}$ is a complex conjugate to $\vec{c}$. So, in complex representation of vector harmonic field we have two possible choices of time-dependent factor; $\exp(\mathrm{i}\omega t)$ or $\exp(-\mathrm{i}\omega t)$. There is no real difference which choice we made, because the quantities of physical meanings are always real [12, p. 14], but once the sign convention choice has been made it has to be used consistently everywhere. As a time-dependent factor we choose the more common $\exp(-\mathrm{i}\omega t)$.

If we assume time-dependence $\exp(-\mathrm{i}\omega t)$ and if we insert equations (2.7)–(2.9) into Maxwell equations (2.1)–(2.4) we get

$$\nabla \cdot \vec{D} = \rho_{\mathrm{f}}, \tag{2.14}$$

$$\nabla \cdot \vec{B} = 0, \tag{2.15}$$

$$\nabla \times \vec{E} = \mathrm{i}\omega\vec{B}, \tag{2.16}$$

$$\nabla \times \vec{H} = \vec{J}_{\mathrm{f}} - \mathrm{i}\omega\vec{D}. \tag{2.17}$$

When we insert equations (2.7), (2.9) a (2.10) into equation (2.4) we get

$$\nabla \times \vec{H} = \sigma\vec{E} + \frac{\partial}{\partial t}(\varepsilon_0\vec{E} + \varepsilon_0\chi\vec{E}) \tag{2.18}$$

By partial derivative with respect to time t and following adjustment of the result we get an equation for complex permittivity $\hat{\varepsilon}$:

$$\hat{\varepsilon} = \varepsilon_0(1+\chi) + \mathrm{i}\frac{\sigma}{\omega}. \tag{2.19}$$

The relative permittivity (or dielectric function) ε is then

$$\varepsilon = \hat{\varepsilon}/\varepsilon_0 = 1 + \chi + \mathrm{i}\frac{\sigma}{\varepsilon_0\omega}. \tag{2.20}$$

2.3 Electromagnetic wave equation

Electromagnetic wave equation describes the propagation of electromagnetic waves through the medium. It is a second order partial differential equation. To derive it, we consider a homogeneous medium ($\nabla\varepsilon = 0$) without free charge and current densities ($\rho_{\mathrm{f}} = 0$, $\vec{J}_{\mathrm{f}} = 0$). We come out the equation for Faraday law (2.3) and from the left, we apply operator $\nabla\times$ on it

$$\nabla \times \nabla \times \vec{E} = -\frac{\partial(\nabla \times \vec{B})}{\partial t}. \tag{2.21}$$

The right side of this equation resembles the Ampere-Maxwell law expressed by equation (2.4). It has been set $\vec{J}_\mathrm{f} = 0$, so it is possible by substitution in (2.4) to rewrite this equation into following form

$$\nabla \times \nabla \times \vec{E} = -\mu_0 \frac{\partial^2 \vec{D}}{\partial t^2}. \tag{2.22}$$

Using the identity $\nabla \times \nabla \times \vec{E} \equiv \nabla(\nabla \cdot \vec{E}) - \nabla^2 \vec{E}$ and using the formula for differentiation of product $\nabla \cdot (\varepsilon \vec{E}) \equiv \vec{E} \cdot \nabla\varepsilon + \varepsilon \nabla \cdot \vec{E}$ it is possible to rewrite equation (2.22)[10] into form

$$\nabla \left(-\frac{1}{\varepsilon} \vec{E} \cdot \nabla\varepsilon \right) - \nabla^2 \vec{E} = -\mu_0 \varepsilon_0 \varepsilon \frac{\partial^2 \vec{E}}{\partial t^2}, \tag{2.23}$$

which can be transformed into final equation for electromagnetic wave

$$\nabla^2 \vec{E} - \frac{\varepsilon}{c^2} \frac{\partial^2 \vec{E}}{\partial t^2} = 0, \tag{2.24}$$

where $c^2 = 1/(\varepsilon_0 \mu_0)$.

We assume a time-harmonic electromagnetic field expressed by $\vec{E}(\vec{r}, t) = \vec{E}(\vec{r}) \exp(-i\omega t)$. By inserting to (2.24) we get the time-independent electromagnetic wave equation, known as Helmholtz equation

$$\nabla^2 \vec{E} + k_0^2 \varepsilon \vec{E} = 0, \tag{2.25}$$

where $k_0 = \omega/c$ is a wave vector of the electromagnetic wave in vacuum.

There is relative permittivity ε in both of electromagnetic wave equations (2.24) and (2.25). This means, that the equations have to be solved separately for regions of constant values of ε and the solutions than connected together using appropriate conditions for boundaries between the regions of different values of ε. Electromagnetic field in regions of different ε (marked by indices 1 and 2) is matched at the interface between the regions by the following boundary conditions [13, p. 18]:

$$(\vec{D}_2 - \vec{D}_1) \cdot \vec{n} = \sigma, \tag{2.26}$$

$$(\vec{B}_2 - \vec{B}_1) \cdot \vec{n} = 0, \tag{2.27}$$

$$\vec{n} \times (\vec{E}_2 - \vec{E}_1) = \vec{0}, \tag{2.28}$$

$$\vec{n} \times (\vec{H}_2 - \vec{H}_1) = \vec{K}, \tag{2.29}$$

where σ and $\vec{K}$ are the surface charge and current densities at the interface between the regions, respectively and $\vec{n}$ is a unit vector normal to the interface.

2.4 Time dependent quantities

Complex permittivity $\hat{\varepsilon}$ which has been derived in section 2.2 depends, in general, on angular frequency ω. In the equation for complex permittivity $\hat{\varepsilon}$ (2.19), ω is presented

[10] Assuming still $\rho_\mathrm{f} = 0$, and so $\nabla \cdot \vec{D} = 0$.

directly and also through the presence of conductivity σ and susceptibility χ which are both functions of ω. As the quantities $\hat{\varepsilon}$, σ and χ describes the response of the medium to external stimulus (electromagnetic field) and as all of them are the functions of ω, it can be expected that the response of the medium to the stimulus varies with frequency. To find the response of the medium to incoming wave radiation at specific wavelength we need to use a mathematical tool known as Fourier transform.

2.4.1 Fourier transform

Fourier transform is a specific case of integral transform. According to [14, p. 7], Fourier transform is usually defined using three non-zero constants A, B and k. Let there exist function $f(\vec{x})$ and its Fourier transform $\mathrm{FT}\{f(\vec{x})\} = \mathcal{F}(\vec{X})$. The Fourier transform is then defined as:

$$\mathrm{FT}\{f(\vec{x})\} = \mathcal{F}(\vec{X}) = A^N \int_{-\infty}^{\infty} \cdots \int f(\vec{x}) \exp(-ik\vec{X}\cdot\vec{x})\,\mathrm{d}^N\vec{x}. \tag{2.30}$$

Inverse Fourier transform $\mathrm{FT}^{-1}\{\mathcal{F}(\vec{X})\} = f(\vec{x})$ is then defined in similar way as:

$$\mathrm{FT}^{-1}\{\mathcal{F}(\vec{X})\} = f(\vec{x}) = B^N \int_{-\infty}^{\infty} \cdots \int \mathcal{F}(\vec{X}) \exp(ik\vec{X}\cdot\vec{x})\,\mathrm{d}^N\vec{X}. \tag{2.31}$$

It is expected that functions $f(\vec{x})$ and $\mathcal{F}(\vec{X})$ are absolutely integrable, piecewise smooth, complex functions of real variables $\vec{x}$ and $\vec{X}$ which belongs to N-dimensional space. Constants A and B are always chosen real and positive and constant k is then given by following condition

$$AB = \frac{|k|}{2\pi}. \tag{2.32}$$

In different fields, where Fourier transform is used, the values of constants A, B and k are chosen differently. We will follow that common in solid state physics and we choose following values: $A = 1$, $B = 1/2\pi$ a $k = 1$.

Let us consider a real time-dependent function $f(t)$. Fourier transform $\mathcal{F}(\omega)$ of $f(t)$ is according to [12, p. 15] given by integral[11]

$$\mathrm{FT}\{f(t)\} = \mathcal{F}(\omega) = \int_{-\infty}^{+\infty} f(t) \exp(-\mathrm{i}\omega t)\,\mathrm{d}t. \tag{2.33}$$

Inverse Fourier transform is then defined by integral

$$\mathrm{FT}^{-1}\{\mathcal{F}(\omega)\} = f(t) = \frac{1}{2\pi}\int_{-\infty}^{+\infty} \mathcal{F}(\omega) \exp(\mathrm{i}\omega t)\,\mathrm{d}\omega. \tag{2.34}$$

[11] We substitute $\vec{x} \to t, \vec{X} \to \omega, k = 1$ and we insert it into the core of Fourier transform, then we get $\exp(\pm\mathrm{i}k\vec{X}\cdot\vec{x}) \to exp(\pm\mathrm{i}\omega t)$.

By Fourier transform of Maxwell's Equations (2.1)-(2.4) for medium without free charges ($\rho_\mathrm{f} = 0$) and with assuming that the order of differentiation and integration can be interchanged we get

$$\nabla \cdot \vec{\mathcal{D}}(\omega) = 0, \tag{2.35}$$

$$\nabla \cdot \vec{\mathcal{B}}(\omega) = 0, \tag{2.36}$$

$$\nabla \times \vec{\mathcal{E}}(\omega) = i\omega\vec{\mathcal{B}}(\omega), \tag{2.37}$$

$$\nabla \times \vec{\mathcal{H}}(\omega) = \vec{\mathcal{J}}_\mathrm{f}(\omega) - i\omega\vec{\mathcal{D}}(\omega), \tag{2.38}$$

where $\vec{\mathcal{D}}(\omega)$, $\vec{\mathcal{B}}(\omega)$, $\vec{\mathcal{E}}(\omega)$, $\vec{\mathcal{H}}(\omega)$ and $\vec{\mathcal{J}}_\mathrm{f}(\omega)$ are Fourier transforms of the displacement field $\vec{D}$, magnetic induction $\vec{B}$, electric field $\vec{E}$, magnetic field $\vec{H}$ and free current density $\vec{J}_\mathrm{f}$, respectively.

Even for Fourier transforms of foregoing quantities, there are constitutive relations similar to those expressed by Equations (2.7)-(2.9):

$$\vec{\mathcal{J}}_\mathrm{f}(\omega) = \sigma(\omega)\vec{\mathcal{E}}(\omega), \tag{2.39}$$

$$\vec{\mathcal{B}}(\omega) = \mu(\omega)\vec{\mathcal{H}}(\omega), \tag{2.40}$$

$$\vec{\mathcal{P}}(\omega) = \varepsilon_0\chi(\omega)\vec{\mathcal{E}}(\omega), \tag{2.41}$$

where $\vec{\mathcal{P}}(\omega)$ is a Fourier transform of polarization $\vec{P}$. We can notice that in Equations (2.39)-(2.41) the quantities $\vec{\mathcal{J}}_\mathrm{f}(\omega)$, $\vec{\mathcal{B}}(\omega)$ and $\vec{\mathcal{P}}(\omega)$ are always expressed as a product of two Fourier transforms. In the following paragraph, we will look closer on this product of two Fourier transform.

2.4.2 Convolution of linear system

Equations (2.39)-(2.41) express a product of two Fourier transforms. Let us look closer at one of them: Equation (2.41) expressing the Fourier transform of polarization. In this equation, there is a product of two Fourier transforms, $\chi(\omega)$ and $\vec{\mathcal{E}}(\omega)$. According to convolution theorem [14, p. 77-81], the product of those two Fourier transforms is proportional to convolution of functions $\chi(t)$ and $\vec{E}(t)$.

In general, convolution of functions $f_1(t)$ and $f_2(t)$ is function $f(t) = f_1(t) * f_2(t)$ which is given by integral

$$f(t) = f_1(t) * f_2(t) = \int_{-\infty}^{\infty} f_1(t')f_2(t-t')\,\mathrm{d}t'. \tag{2.42}$$

Further according to [14, p. 79], there are following relations between the Fourier transform and convolution:

$$FT\{f_1(t) * f_2(t)\} = \frac{1}{A}[(F_1(\omega)F_2(\omega)], \tag{2.43}$$

$$FT\{f_1(t)f_2(t)\} = B[F_1(\omega) * F_2(\omega)]. \tag{2.44}$$

Knowing all of this, we can apply the convolution theorem on Equation (2.41). According to [12, p. 17] we get

$$\vec{P}(t) = \varepsilon_0 \int_{-\infty}^{\infty} G(t-t')\vec{E}(t')\mathrm{d}t, \tag{2.45}$$

where

$$G(t) = \frac{1}{2\pi}\int_{-\infty}^{\infty} \chi(\omega)\exp(-i\omega t)\mathrm{d}\omega. \tag{2.46}$$

The function $G(t-t')$ is an impulse response function which characterized the response of the matter to external stimulus. The main consequence of the equations (2.45) and (2.46) is that polarization $\vec{P}$ in time t depends on the electric field $\vec{E}$ in all previous times t'. For clarification, let us imagine that a constant external electric field starts to interact with a non-polarized matter. The matter is not instantly fully polarized, the response simply takes some time, so instead the matter is gradually polarized and after some time it is fully polarized. Also, when the external field vanishes, the polarization of the matter will gradually decrease to zero. Therefore, the polarization state of the matter in time t is given by all the states of external electric field $\vec{E}$ in all previous times, not by instantaneous value $\vec{E}(t)$. Another, quite logical, consequence is that with increasing time-difference $t-t'$ the contribution of electric field $\vec{E}(t')$ to polarization $\vec{P}(t)$ decreases, so the biggest influence on matter polarization in time t has electric field in times $t' \to t$.

For $\vec{B}$ and $\vec{J}_\mathrm{f}$, it is possible to get equations which are similar to (2.45) and (2.46) by application of convolution theorem on equations (2.39) and (2.40). The phenomenon described above, i.e. temporal delocalization of response to stimulus, is actually quite common and it is called the temporal dispersion, and occurs for all the matter-connected electromagnetic quantities ($\vec{D}, \vec{H}, \vec{J}_\mathrm{f}$ ...).

The less common phenomenon is spatial dispersion. It means spatial delocalization of matter response to stimulus, so the values of quantities at specific point are affected by values of the same quantities in all the surrounding space. Nevertheless, in the field of our interest, i.e. light-matter interaction in plasmonic antennas, the response of matter to external stimulus is spatially localized up to the ultraviolet frequencies of stimulus [15, p. 9]. Therefore, we will no longer discuss spatial delocalization and we settle with the knowledge that material response functions are function of frequency only.

2.5 Dielectric function of matter

By optical properties of medium, we usually mean, how the medium affects the propagation of electromagnetic wave at optical wavelengths. There are two quantities which are usually used for description of optical properties. One is complex index of refraction $N = n + \mathrm{i}k$ and the other is complex dielectric function $\varepsilon = \varepsilon' + \mathrm{i}\varepsilon''$ which is also known as relative permittivity. These two quantities are interrelated by following relations [16, p. 11]:

$$N = n + \mathrm{i}k = \sqrt{\varepsilon} = \sqrt{\varepsilon' + \mathrm{i}\varepsilon''}, \tag{2.47}$$

$$\varepsilon' = n^2 - k^2, \tag{2.48}$$

$$\varepsilon'' = 2nk, \tag{2.49}$$

$$n = \sqrt{\frac{\sqrt{\varepsilon'^2 + \varepsilon''^2} + \varepsilon'}{2}}, \tag{2.50}$$

$$k = \sqrt{\frac{\sqrt{\varepsilon'^2 + \varepsilon''^2} - \varepsilon'}{2}}. \tag{2.51}$$

Quantities N a ε describe optical properties of medium. However, one of them is often preferred when describing optical phenomena. For example, complex index of refraction N is used in the relations for Fresnel reflection or transmission coefficients. Also, when we investigate the electromagnetic wave propagation in the medium, we use real part of refraction index n in the relation for phase velocity and imaginary part k for the description of damping of the wave during the propagation. On the other hand, for description of electromagnetic scattering by small particles as well as in the description of microscopic optical phenomena the dielectric function ε is preferentially used.

Several models (either classical or quantum) have been introduced to describe the interaction of electromagnetic radiation with matter. Despite the fact that classical models do not consider any quantum effects, they are fully adequate in most cases. We will show two classical models, Drude model and Lorentz model. The first one, introduced by Paul Drude in 1900 [17], is suitable to describe the transport properties in metals, the latter, introduced in 1906 by Hendrik Antoon Lorentz [18], extends Drude model to dielectrics. Therefore, from the present point-of-view Drude model can be considered as a simplification of Lorentz model.

2.5.1 Lorentz model

Lorentz model is a classical model for the description of optical properties of matter. In this model ions and electrons of the matter are considered as simple harmonic oscillators which interact with applied electromagnetic field. We assume that the matter consist of a collection of identical, independent, isotropic harmonic oscilators[12].

According to the model, an electron (an oscillator) of mass m and charge e is coupled with nucleus by an attractive force $-m\omega_0^2\vec{x}$ (also known as restoring force), where $\vec{x}$ is the spatial displacement from equilibrium and ω_0 is the oscillator eigenfrequency. The damping of the oscillator is represented by damping force $b\dot{\vec{x}}$, where b is a damping constant. The last force which acts upon the oscillator is the driving force which is produced by the electric field $\vec{E}$. The equation of motion of such oscillator is

$$m\ddot{\vec{x}} + b\dot{\vec{x}} + m\omega_0^2\vec{x} = -e\vec{E}. \tag{2.52}$$

Assuming that the electric field $\vec{E}$ is harmonic with frequency ω, so $\vec{E}(t) = \vec{E}_0 \exp(-\mathrm{i}\omega t)$, then the stationary solution of the previous equation is[13]:

$$\vec{x}(t) = \frac{-(e/m)}{\omega_0^2 - \omega^2 - \mathrm{i}\gamma\omega}\vec{E}(t), \tag{2.53}$$

[12] This is the simplest version of Lorentz model, fully sufficient to describe the optical properties of ideal matter. The model itself can also be expanded using multiple different oscillators or anisotropic oscillators.

[13] The transient part of the solution vanishes because of the damping. The frequency of oscillations is the same as the frequency of the driving electric field.

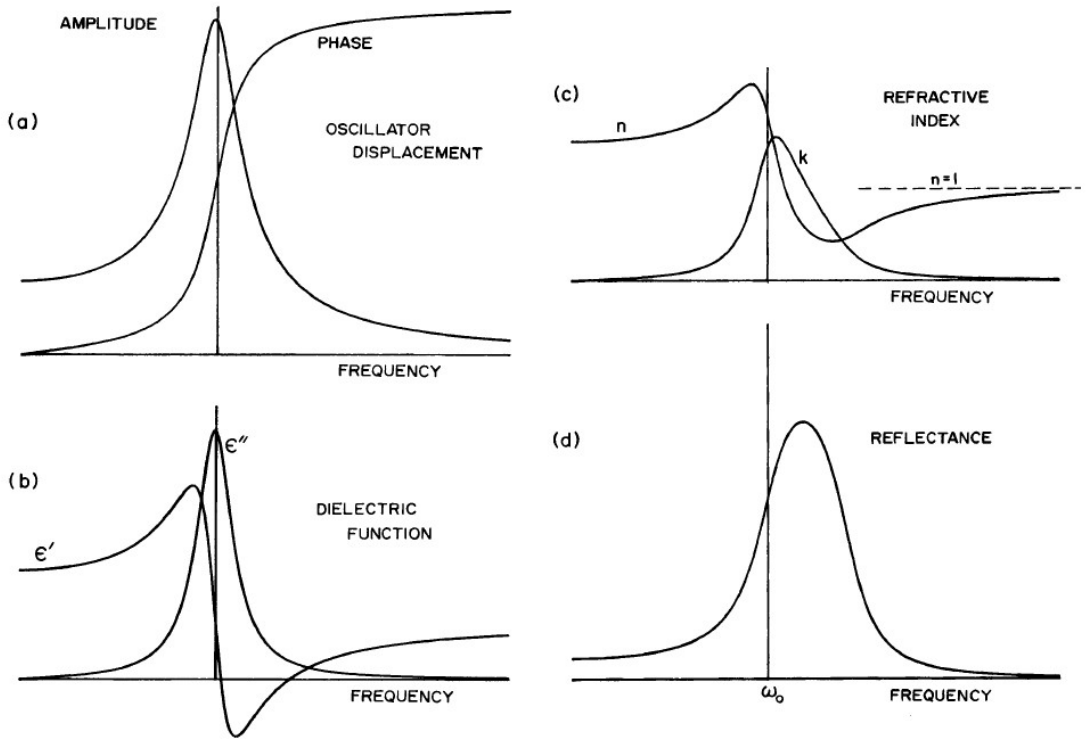

Figure 2.1: Characteristics of one oscillator Lorentz model, (a) amplitude and phase of oscillator displacement, (b) dielectric function, (c) refractive index, (d) reflectance. Taken from [12].

where $\gamma = b/m$. When oscillations are damped, i.e. when $\gamma > 0$, then the proportionality factor between the displacement x and the driving field E is complex. This means that the $\vec{x}(t)$ and $\vec{E}(t)$ are not, in general, in phase. This is evident when we rewrite the complex result using the geometrical representation of complex number $x = (eE/m)A\exp(\mathrm{i}\Theta)$. Then the amplitude A and the phase angle Θ are [12, p. 229]

$$A = \frac{1}{\sqrt{(\omega_0^2 - \omega^2)^2 + \gamma^2\omega^2}}, \tag{2.54}$$

$$\Theta = \tan^{-1}\frac{\gamma\omega}{\omega^2 - \omega^2}. \tag{2.55}$$

As it can be seen in Figure 2.1a the amplitude reaches its maximum at $\omega \simeq \omega_0$, where also phase change occurs. For frequencies ω far below the resonant frequency ω_0 the oscillator responds in phase with the driving force, for frequencies far above the resonance the response of the oscillator shifted in phase by $180\,^\circ$ (or by π) with respect to the driving force. The other characteristics of Lorentz model oscillator, like dielectric function or refraction index, are also shown in Figure 2.1.

Electric field $\vec{E}(t)$ displaces electrons out of equilibrium, therefore the dielectric becomes polarized. Dipole moment of a single oscillating electron is $\vec{p} = -e\vec{x}$. If $\mathcal{N}$ is a number

of such oscillators in volume unit[14], the polarization[15] $\vec{P} = \mathcal{N}\vec{p} = -\mathcal{N}e\vec{x}$. Then by substitution in Equation (2.53) we get

$$\vec{P} = \frac{\omega_p^2}{\omega_0^2 - \omega^2 - \mathrm{i}\gamma\omega}\varepsilon_0\vec{E}, \tag{2.56}$$

where $\omega_p = \sqrt{\mathcal{N}e^2/m\varepsilon_0}$ is known as the plasma frequency.

By comparison of Equations (2.56) and (2.9) we get

$$\chi(\omega) = \frac{\omega_p^2}{\omega_0^2 - \omega^2 - \mathrm{i}\gamma\omega}. \tag{2.57}$$

If we proceed from the constitutive relation (2.10) and insert Equation (2.57) into it, we get a dielectric function of our system of simple oscillators:

$$\varepsilon(\omega) = 1 + \chi(\omega) = 1 + \frac{\omega_p^2}{\omega_0^2 - \omega^2 - \mathrm{i}\gamma\omega}. \tag{2.58}$$

Real ε' and imaginary ε'' part of the dielectric function ε then are:

$$\varepsilon'(\omega) = 1 + \chi'(\omega) = 1 + \frac{\omega_p^2(\omega_0^2 - \omega^2)}{(\omega_0^2 - \omega^2)^2 + \gamma^2\omega^2}, \tag{2.59}$$

$$\varepsilon''(\omega) = \chi''(\omega) = \frac{\omega_p^2\gamma\omega}{(\omega_0^2 - \omega^2)^2 + \gamma^2\omega^2}. \tag{2.60}$$

2.5.2 Drude model

Drude model describes optical properties of metals. In fact, the model can be considered as a special case of Lorentz model, where electrons are not bonded to the atom cores, so in the reaction to the external field they can move freely. Equation of motion equation of these free electrons then differs from Lorentz-model motion equation (2.52) only by missing part representing the electron-core bond[16]. Therefore, the Drude model equation of motion is following:

$$m\ddot{\vec{x}} + m\gamma\dot{\vec{x}} = -e\vec{E}. \tag{2.61}$$

If we consider, as in the case of the Lorentz model, that the external electric field is time-harmonic, so $\vec{E}(t) = \vec{E}_0\exp(-\mathrm{i}\omega t)$, the solution of the motion equation (2.61) is the following time dependency of electron displacement $\vec{x}$:

$$\vec{x}(t) = \frac{(e/m)}{\omega^2 + \mathrm{i}\gamma\omega}\vec{E}(t), \tag{2.62}$$

[14] This corresponds to charge carrier concentration.

[15] Polarization is an average electric dipole moment in volume unit

[16] $m\omega_0^2 K = 0$

Due to the external electric field, electrons in the matter are displaced with respect to the position of atom cores and the matter becomes polarized. Polarization $\vec{P}$ is then

$$\vec{P} = \mathcal{N}e\vec{x} = \frac{\omega_p^2}{\omega^2 + \mathrm{i}\gamma\omega}\vec{E}, \tag{2.63}$$

where $\mathcal{N}$ is the number of free electron in a volume unit.

Using the same approach as in the case of the Lorentz model we get an equation describing the dielectric function

$$\varepsilon(\omega) = 1 - \frac{\omega_p^2}{\omega^2 + \mathrm{i}\gamma\omega}. \tag{2.64}$$

Again, the dielectric function $\varepsilon(\omega)$ is, in general, complex. The real and imaginary parts are

$$\varepsilon'(\omega) = 1 - \frac{\omega_p^2}{\omega^2 + \gamma^2}, \tag{2.65}$$

$$\varepsilon''(\omega) = \frac{\omega_p^2\gamma}{\omega(\omega^2 + \gamma^2)}. \tag{2.66}$$

Analysis of the free-electrons movement shows that the damping constant is related to relaxation time τ as $\gamma = 1/\tau$ [12, p. 245]. By substitution of γ by τ in (2.65) and (2.66) we get dielectric function in the following form:

$$\varepsilon'(\omega) = 1 - \frac{\omega_p^2\tau^2}{1 + \omega^2\tau^2}, \tag{2.67}$$

$$\varepsilon''(\omega) = \frac{\omega_p^2\tau}{\omega(1 + \omega^2\tau^2)}. \tag{2.68}$$

Although it might seem from the preceding description, the real part ε' and imaginary part ε'' of dielectric function are not independent on each other. The dependence of one part on the other is described by Kramers-Kronig relations, which will be described in the following paragraph.

2.5.3 Kramers-Kronig relations

In this section, the mutual relation between the real and imaginary part of a dielectric function, known as the Kramers-Kronig relations will be shown. The Kramers-Kronig (KK) relations are, in general, the bidirectional relations between real and imaginary part of any analytical function which satisfies certain conditions. KK relations are based on Cauchy's theorem.

Let us assume that there is a function $g(\Omega)$, where $\Omega = \Omega' + \mathrm{i}\Omega''$ (eventually $\omega = \omega' + \mathrm{i}\omega''$), which is analytical on and inside a closed contour $\mathcal{C}$. The Kramers-Kronig relations between the real and imaginary part of the complex function $g(\Omega)$ exist, if the function $g(\Omega)$ satisfies the following conditions [19, p. 309]:

- The poles of the function $g(\Omega)$ are all below the real axis.

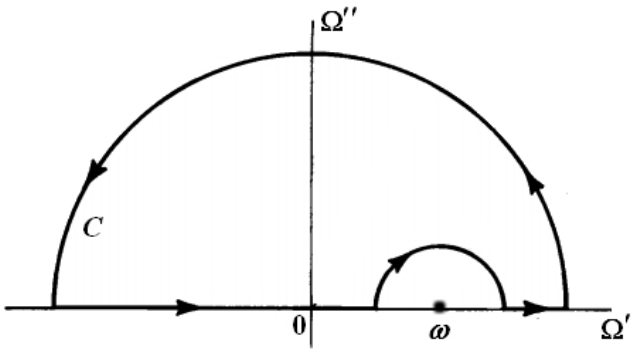

Figure 2.2: Contour $\mathcal{C}$ for the Cauchy pricipal value integral in the complex Ω-plane.

- $\oint \frac{g(\omega)}{\omega} \mathrm{d}\omega$ vanishes when taken around an infinite semicircle in upper half-plane of the complex Ω-plane.
- The real part $g'(\Omega)$ is even and the imaginary part $g''(\Omega)$ is odd with respect to real ω, i.e. $g'(\Omega') = g'(-\Omega')$ and $g''(-\Omega') = -g''(\Omega')$.

These conditions are met also by functions describing other physical phenomena such as refractive index, electrical conductivity or permeability. In the derivation of KK relations we will proceed according to [16, p.30-34]. Using the Cauchy theorem on function $g(\omega)$ we get

$$\oint_{\mathcal{C}} \frac{g(\Omega)}{\Omega - \omega} \, \mathrm{d}\Omega = 0, \tag{2.69}$$

assuming ω lies outside the contour $\mathcal{C}$. The integral contour $\mathcal{C}$ is selected according to the visualization in Figure 2.2, point ω lies on real axis Ω' outside contour $\mathcal{C}$. We assume that for $|\Omega| \to \infty$ function $g(\Omega)$ acts as function $\Omega^{-\alpha}$, where $\alpha \geq 1$. Then

$$\mathcal{P} \int_{-\infty}^{\infty} \frac{g(\Omega')}{\Omega' - \omega} \, \mathrm{d}\Omega' = \mathrm{i}\pi g(\omega), \tag{2.70}$$

where $\mathcal{P}$ denotes the Cauchy principal value. Function $g(\omega)$ is, in general, complex, so it can be written as a summation of the real and imaginary part

$$g(\Omega) = \Re\{g(\Omega)\} + \mathrm{i}\Im\{g(\Omega)\}. \tag{2.71}$$

By inserting (2.70) into (2.71), we get:

$$\Im\{g(\omega)\} = -\frac{1}{\pi} \mathcal{P} \int_{-\infty}^{\infty} \frac{\Re\{g(\Omega')\}}{\Omega' - \omega} \, \mathrm{d}\Omega', \tag{2.72}$$

$$\Re\{g(\omega)\} = \frac{1}{\pi} \mathcal{P} \int_{-\infty}^{\infty} \frac{\Im\{g(\Omega')\}}{\Omega' - \omega} \, \mathrm{d}\Omega'. \tag{2.73}$$

If condition $\Re\{g(-\omega)\} = \Re\{g(\omega)\}$ and $\Im\{g(-\omega)\} = -\Im\{g(\omega)\}$ is satisfied then (2.72) and (2.73) transform into

$$\Im\{g(\omega)\} = -\frac{2\omega}{\pi} \mathcal{P} \int_{0}^{\infty} \frac{\Re\{g(\Omega')\}}{\Omega'^2 - \omega^2} \, \mathrm{d}\Omega', \tag{2.74}$$

$$\Re\{g(\omega)\} = \frac{2}{\pi} \mathcal{P} \int_{0}^{\infty} \frac{\Im\{g(\Omega')\}}{\Omega'^2 - \omega^2} \, \mathrm{d}\Omega'. \tag{2.75}$$

Susceptibility $\chi(\omega)$ satisfies the conditions imposed on function $g(\omega)$, so it can be directly inserted into the KK relations. However, the dielectric function and refraction index satisfy all but one condition. For $\omega \to \infty$, neither dielectric function ε nor refractive index N vanishes as requested, but $\lim_{\omega\to\infty} \varepsilon(\omega) = 1$ and $\lim_{\omega\to\infty} N(\omega) = 1$. But this is a small complication which can be easily overcome. $\chi(\omega) = \varepsilon(\omega) - 1$, hence function $\varepsilon(\omega) - 1$ also satisfies even the high frequency limit condition. Therefore, to get the KK relations for dielectric function, $\varepsilon(\omega) - 1$ is inserted into the KK relations (2.74) and (2.75)[12, p. 28]. The final form of the KK relations for the dielectric function is

$$\varepsilon''(\omega) = -\frac{2\omega}{\pi}\mathcal{P}\int_0^\infty \frac{\varepsilon'(\Omega) - 1}{\Omega^2 - \omega^2}\,\mathrm{d}\Omega, \tag{2.76}$$

$$\varepsilon'(\omega) - 1 = \frac{2}{\pi}\mathcal{P}\int_0^\infty \frac{\Omega\varepsilon''(\Omega)}{\Omega^2 - \omega^2}\,\mathrm{d}\Omega. \tag{2.77}$$

By a similar process the refractive index N can be *shifted by 1* and function $N(\omega) - 1$ used in the KK relations for refractive index $N = n + ik$. The KK relations for the refractive index then have the following form:

$$k(\omega) = -\frac{2\omega}{\pi}\mathcal{P}\int_0^\infty \frac{n(\Omega) - 1}{\Omega^2 - \omega^2}\,\mathrm{d}\Omega, \tag{2.78}$$

$$n(\omega) - 1 = \frac{2}{\pi}\mathcal{P}\int_0^\infty \frac{\Omega k(\Omega)}{\Omega^2 - \omega^2}\,\mathrm{d}\Omega. \tag{2.79}$$

2.5.4 Sellmeier equation

Sellmeier equation is a consequence of interdependence of dispersion and absorption in the matter which is expressed in (2.79) [16, p. 34]. Sellmeier equation is an empirical relation between the real part of refraction index and wavelength.

Usually, it is introduced in one of these two forms:

$$n(\lambda) = A\ + \frac{B_1}{\lambda^2} + \frac{B_2}{\lambda^4}, \tag{2.80}$$

$$n(\lambda) = 1 + \frac{B_1\lambda^2}{\lambda^2 - C_1} + \frac{B_2\lambda^2}{\lambda^2 - C_2}, \tag{2.81}$$

where A, B_1, B_2, C_1, C_2 are empirical constants. Sellmeier equation introduced by one of these equations describes the dependence of refractive index on wavelength for a medium which has no absorption.

As refractive index N and dielectric function ε are connected by equation (2.47), it is possible to modify the Sellmeier equation to express dielectric function as a function of wavelength. For the material with non-zero absorption the Sellmeier equation for dielectric function is

$$\varepsilon(\lambda) = \varepsilon' + \varepsilon'' = 1 + \frac{A\lambda^2}{\lambda^2 - B^2 - \mathrm{i}\,2C\lambda}, \tag{2.82}$$

where A, B, C are empirical constants [20]. If the material exhibits no absorption, the imaginary part of (2.82) vanishes.

3 Surface plasmon polaritons

Despite the fact that this thesis is aimed at plasmonic antennas and localized surface plasmons, the other fundamental plasmonic excitations, surface plasmon polaritons (SPP) are introduced for completeness. SPPs are electromagnetic waves which propagate along the interface between conductor and dielectric. These electromagnetic surface waves are evanescently confined in the direction perpendicular to the interface. SPPs emerge from the coupling of external electromagnetic field and conductive electrons in metals which results in collective oscillations of free electron gas in metals. SPPs will be derived using the approach from [15].

3.1 Electromagnetic wave at interface

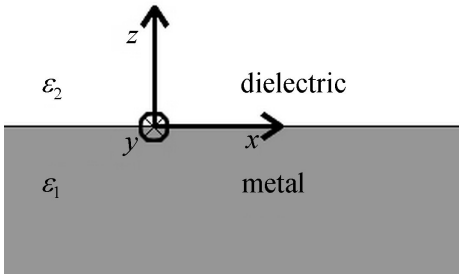

Figure 3.1: An interface between metal and dielectric. Optical properties of both media are described by dielectric functions ε_1 and ε_2.

Now, we focus on conditions which enable the propagation of electromagnetic waves along the interface between metal and dielectric. For simplicity this will be shown on elementary example in Cartesian coordinate system. The scheme of geometry of this interface is shown in Figure 3.1. As mentioned before, SPP is a surface wave, so we expect that an electromagnetic wave propagates in x-direction along the interface ($z = 0$) between dielectric and metal. This wave is described as $\vec{E}(x,z) = \vec{E}(z)\exp(\mathrm{i}\beta x)$. Complex parameter β acts as propagation constant of the propagating wave and corresponds to the component of the wave vector in the direction of propagation. By inserting of this expression of the electromagnetic wave into Helmholtz Equation (2.25) we get electromagnetic wave equation in form

$$\frac{\partial^2 \vec{E}(x,z)}{\partial z^2} + (k_0^2\varepsilon - \beta^2) = 0. \tag{3.1}$$

Similar equation also exists for the description of magnetic field $\vec{H}$.

In order to use the wave equation for the determination of spatial distribution of electromagnetic field, it is necessary to express the components of the fields $\vec{E}$ and $\vec{H}$. This can be done applying curl operator on Maxwell's equations (2.3) and (2.4) [15, p. 23]. For the time-harmonic field ($\exp(-\mathrm{i}\omega t)$, therefore $\frac{\partial}{\partial t} = -\mathrm{i}\omega$) we get following system of equations:

$$\frac{\partial E_z}{\partial y} - \frac{\partial E_y}{\partial z} = \mathrm{i}\omega\mu_0 H_x, \tag{3.2}$$

$$\frac{\partial E_x}{\partial z} - \frac{\partial E_z}{\partial x} = \mathrm{i}\omega\mu_0 H_y, \tag{3.3}$$
$$\frac{\partial E_y}{\partial x} - \frac{\partial E_x}{\partial y} = \mathrm{i}\omega\mu_0 H_z, \tag{3.4}$$
$$\frac{\partial H_z}{\partial y} - \frac{\partial H_y}{\partial z} = -\mathrm{i}\omega\varepsilon_0\varepsilon E_x, \tag{3.5}$$
$$\frac{\partial H_x}{\partial z} - \frac{\partial H_z}{\partial x} = -\mathrm{i}\omega\varepsilon_0\varepsilon E_y, \tag{3.6}$$
$$\frac{\partial H_y}{\partial x} - \frac{\partial H_x}{\partial y} = -\mathrm{i}\omega\varepsilon_0\varepsilon E_z. \tag{3.7}$$

In our problem, we consider surface wave propagating in x-direction ($\frac{\partial}{\partial x} = \mathrm{i}\beta$) and material homogenity in y-direction ($\frac{\partial}{\partial y} = 0$). Then the foregoing system of equations transforms into:

$$\frac{\partial E_y}{\partial z} = -\mathrm{i}\omega\mu_0 H_x, \tag{3.8}$$
$$\frac{\partial E_x}{\partial z} - \mathrm{i}\beta E_z = \mathrm{i}\omega\mu_0 H_y, \tag{3.9}$$
$$\mathrm{i}\beta E_y = \mathrm{i}\omega\mu_0 H_z, \tag{3.10}$$
$$\frac{\partial H_y}{\partial z} = \mathrm{i}\omega\varepsilon_0\varepsilon E_x, \tag{3.11}$$
$$\frac{\partial H_x}{\partial z} - \mathrm{i}\beta H_z = -\mathrm{i}\omega\varepsilon_0\varepsilon E_y, \tag{3.12}$$
$$\mathrm{i}\beta H_y = -\mathrm{i}\omega\varepsilon_0\varepsilon E_z. \tag{3.13}$$

It can be shown that this system of equations has two possible solutions which differs in the polarization properties of propagating waves. The first solution is a wave with transverse magnetic polarization (TM or p-polarization), where only field components E_x, E_z and H_y differ from zero. The other solution represents a wave with transverse electric polarization (TE or s-polarization), where only field components H_x, H_z and E_y are non-zero.

For TM polarization of the wave, the system of equations (3.8)-(3.13) is reduced to

$$E_x = -\mathrm{i}\frac{1}{\omega\varepsilon_0\varepsilon}\frac{\partial H_y}{\partial z}, \tag{3.14}$$
$$E_z = -\frac{\beta}{\omega\varepsilon_0\varepsilon}H_y, \tag{3.15}$$

and the wave equation for TM polarization has form

$$\frac{\partial^2 H_y}{\partial z^2} + (k_0^2\varepsilon - \beta^2)H_y = 0. \tag{3.16}$$

Similarly, for TE polarization of the wave, the system (3.8)-(3.13) is reduced to

$$H_x = \mathrm{i}\frac{1}{\omega\mu_0}\frac{\partial E_y}{\partial z}, \tag{3.17}$$
$$H_z = \frac{\beta}{\omega\mu_0}E_y, \tag{3.18}$$

and the wave equation for TE polarization is in following form

$$\frac{\partial^2 E_y}{\partial z^2} + (k_0^2 \varepsilon - \beta^2) E_y = 0. \tag{3.19}$$

3.2 Surface plasmon polaritons at single interface

The simplest possible geometry for the description of SPP is a single flat interface (shown in Figure 3.1. It is the interface between a dielectric ($z > 0$), with no absorption[1] and which is described by a real dielectric constant ε_2, and a metal ($z < 0$), which is described by complex[2] dielectric function $\varepsilon_1(\omega)$ with negative real part $\Re\{\varepsilon_1(\omega)\} < 0$. We look for the solution of a wave propagating along the interface in the direction of x axis.

For TM polarization, equations (3.14)-(3.16) get form

$$\begin{aligned} H_y(z) &= A_2 \exp(\mathrm{i}\beta x) \exp(-k_2 z), & (3.20)\\ E_x(z) &= \mathrm{i} A_2 \frac{1}{\omega \varepsilon_0 \varepsilon_2} k_2 \exp(\mathrm{i}\beta x) \exp(-k_2 z), & (3.21)\\ E_z(z) &= -A_2 \frac{\beta}{\omega \varepsilon_0 \varepsilon_2} \exp(\mathrm{i}\beta x) \exp(-k_2 z), & (3.22) \end{aligned}$$

for $z > 0$ and

$$\begin{aligned} H_y(z) &= A_1 \exp(\mathrm{i}\beta x) \exp(k_1 z), & (3.23)\\ E_x(z) &= -\mathrm{i} A_1 \frac{1}{\omega \varepsilon_0 \varepsilon_1} k_1 \exp(\mathrm{i}\beta x) \exp(k_1 z), & (3.24)\\ E_z(z) &= -A_1 \frac{\beta}{\omega \varepsilon_0 \varepsilon_1} \exp(\mathrm{i}\beta x) \exp(k_1 z), & (3.25) \end{aligned}$$

for $z < 0$. k_1 and k_2 are the components of wave vectors perpendicular to the interface which characterizes decay of the wave with increasing distance from the interface. Their reciprocal values $\delta_1 = 1/k_1$ and $\delta_2 = 1/k_2$ define the exponential decay length[3] of field when going perpendicularly from the interface and quantify the confinement of the wave to the interface.

The condition of the continuity of D_z and H_y components at the interface requires $A_1 = A_2$ and also

$$\frac{k_2}{k_1} = -\frac{\varepsilon_2}{\varepsilon_1}. \tag{3.26}$$

[1] We expect that the medium exhibits no absorption only in limited spectral region we are interested in ($\Im\{\varepsilon_2(\omega)\} = 0$ for $\omega \in < \omega_1; \omega_2 >$, where $0 \ll \omega_1 < \omega_2 \ll \infty$). Otherwise, if no absorption was expected for all the frequencies, the striking consequence of Kramers-Kronig relations (2.76) and (2.77) would be not only no frequency dispersion of $\Re\{\varepsilon_2\}$ ($\Re\{\varepsilon_2\} =$ constant), but also $\Re\{\varepsilon_2\} = 1$ for all the frequencies.

[2] As we expect losses in the metal during oscillations of conductive electrons (in the form of Joule's heat resulting from electric resistance of metal), the dielectric function has to have non-zero imaginary part, at least in some interval of frequencies. The consequence of this [from Kramers-Kronig relations expressed by Equation (2.77)] is that the real part of metallic dielectric function has to be a function of frequency.

[3] The length, where the perpendicular field component E_z drops to the value 1/e of its maximum.

The consequence of this equation (taking into account that $k_1 > 0$ and $k_2 > 0$), is that the surface wave exists only at the interface between the materials with the opposite signs of the real part of their dielectric functions, i.e. between metal and dielectric. Furthermore, the component H_y has still to fulfill the wave equation (3.16), so it is necessary that

$$k_1^2 = \beta^2 - k_0^2\varepsilon_1, \tag{3.27}$$
$$k_2^2 = \beta^2 - k_0^2\varepsilon_2. \tag{3.28}$$

Combining these two conditions with condition expressed by equation (3.26) we get crucial expression of propagation constant β

$$\beta = k_0\sqrt{\frac{\varepsilon_1\varepsilon_2}{\varepsilon_1+\varepsilon_2}} = k_0 N_{\text{eff}}, \tag{3.29}$$

where N_{eff} is the effective refraction index at the interface between two media $\varepsilon_1(\omega)$ and ε_2.

For TE polarization equations (3.17)-(3.19) get the following form

$$E_y(z) = A_2\exp(\mathrm{i}\beta x)\exp(-k_2 z), \tag{3.30}$$
$$H_x(z) = -\mathrm{i}A_2\frac{1}{\omega\mu_0}k_2\exp(\mathrm{i}\beta x)\exp(-k_2 z), \tag{3.31}$$
$$H_z(z) = A_2\frac{\beta}{\omega\mu_0}\exp(\mathrm{i}\beta x)\exp(-k_2 z), \tag{3.32}$$
$$\tag{3.33}$$

for $z > 0$ and

$$E_y(z) = A_1\exp(\mathrm{i}\beta x)\exp(k_1 z), \tag{3.34}$$
$$H_x(z) = \mathrm{i}A_1\frac{1}{\omega\mu_0}k_1\exp(\mathrm{i}\beta x)\exp(k_1 z), \tag{3.35}$$
$$H_z(z) = A_1\frac{\beta}{\omega\mu_0}\exp(\mathrm{i}\beta x)\exp(k_1 z), \tag{3.36}$$
$$\tag{3.37}$$

for $z < 0$. The condition of the continuity of E_y and H_x components at the interface requires

$$A_1(k_1 + k_2) = 0. \tag{3.38}$$

Because k_1 and k_2 are always positive and non-zero, this condition is fulfilled only for $A_1 = 0$ and so $A_1 = A_2 = 0$. Thus for TE polarization there no surface waves exist. Therefore, surface plasmon polaritons exist only for TM polarization. Propagation constant of SPP is complex in general, $\beta = \beta' + i\beta''$. The real and imaginary parts are (for a dielectric with no absorption)

$$\beta' = \frac{\omega}{c}\sqrt{\frac{\varepsilon_1'\varepsilon_2}{\varepsilon_1'+\varepsilon_2}}, \tag{3.39}$$
$$\beta'' = \frac{\omega}{c}\sqrt{\left(\frac{\varepsilon_1'\varepsilon_2}{\varepsilon_1'+\varepsilon_2}\right)^3}\frac{\varepsilon_1''}{2\varepsilon_1'^2}. \tag{3.40}$$
$$\tag{3.41}$$

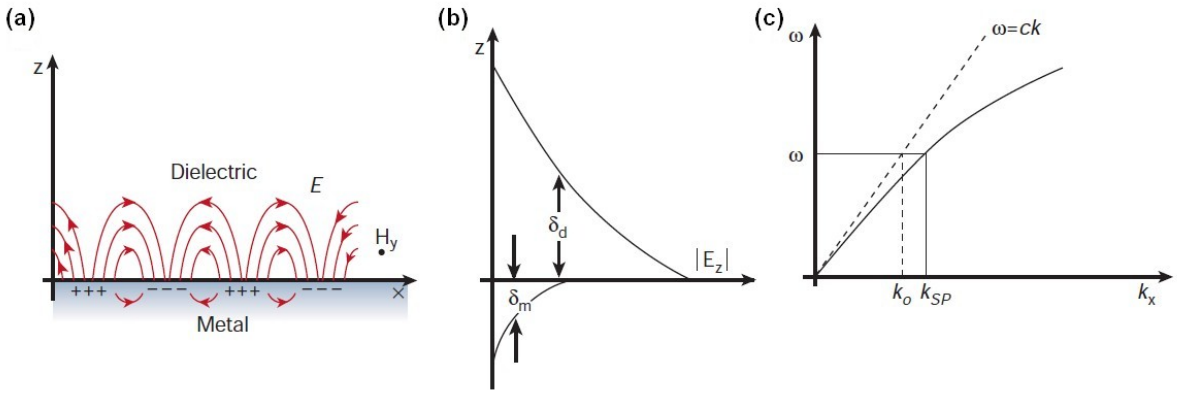

Figure 3.2: (a) Surface plasmon polaritons (SPP) at the interface between a metal and a dielectric, (b) length of SPP confinement (decay length) in a metal δ_m and in a dielectric δ_d, (c) disperse relation for light (dashed line) and for SPP (full line). Taken from [21].

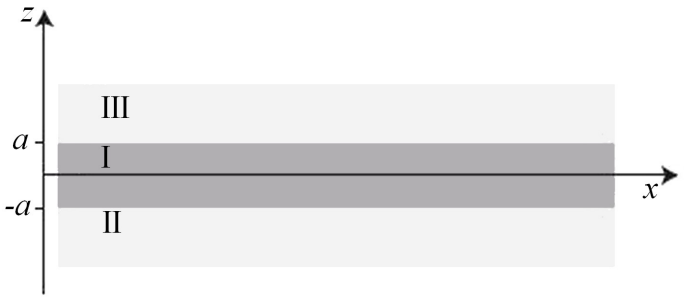

Figure 3.3: A scheme of a system of three layers. A thin metallic film I is surrounded by dielectric layers II and III.

3.3 SPP on insulator-metal-insulator multilayer

Objects of our interest, plasmonic resonant antennas, are metallic stripes situated at a dielectric substrate and surrounded by air or by other dielectric. Their geometry resembles a model of dielectric-metal-dielectric multilayer, which is more often called the insulator-metal-insulator (IMI).

At IMI multilayer which geometry is shown in Figure 3.3, both interfaces can sustain bound SPPs. When the separation between the interfaces is smaller then SPPs' decay length in metal δ_m, SPPs at both interfaces interact with each other and coupled modes rise.

As was shown in Section 3.2, SPPs exist only as TM polarized modes. We start with a description of TM modes by equations(3.14)-(3.16). For $z > a$ the field components are given by [15, p.30]

$$H_y = A \exp(\mathrm{i}\beta x) \exp(-k_3 z), \tag{3.42}$$

$$E_x = \mathrm{i}A \frac{1}{\omega\varepsilon_0\varepsilon_3} k_3 \exp(\mathrm{i}\beta x) \exp(-k_3 z), \tag{3.43}$$

$$E_z = -A\frac{\beta}{\omega\varepsilon_0\varepsilon_3} \exp(\mathrm{i}\beta x) \exp(-k_3 z). \tag{3.44}$$

For $z < -a$ we get

$$H_y = B\exp(\mathrm{i}\beta x)\exp(k_2 z), \tag{3.45}$$

$$E_x = -\mathrm{i}B\frac{1}{\omega\varepsilon_0\varepsilon_2}k_2\exp(\mathrm{i}\beta x)\exp(k_2 z), \tag{3.46}$$

$$E_z = -B\frac{\beta}{\omega\varepsilon_0\varepsilon_2}\exp(\mathrm{i}\beta x)\exp(k_2 z). \tag{3.47}$$

Finally for $-a < z < a$ we get

$$H_y = C\exp(\mathrm{i}\beta x)\exp(k_1 z) + D\exp(\mathrm{i}\beta x)\exp(-k_1 z), \tag{3.48}$$

$$E_x = -\mathrm{i}C\frac{1}{\omega\varepsilon_0\varepsilon_1}k_1\exp(\mathrm{i}\beta x)\exp(k_1 z) + \mathrm{i}D\frac{1}{\omega\varepsilon_0\varepsilon_1}k_1\exp(\mathrm{i}\beta x)\exp(-k_1 z), \tag{3.49}$$

$$E_z = C\frac{\beta}{\omega\varepsilon_0\varepsilon_1}\exp(\mathrm{i}\beta x)\exp(k_1 z) + D\frac{\beta}{\omega\varepsilon_0\varepsilon_1}\exp(\mathrm{i}\beta x)\exp(-k_1 z). \tag{3.50}$$

The condition of continuity of field components H_y a E_x at the interfaces leads to boundary conditions

$$A\ \exp(-k_3 a) = C\exp(k_1 a) + D\exp(-k_1 a), \tag{3.51}$$

$$\frac{A}{\varepsilon_3}k_3\exp(-k_3 a) = -\frac{C}{\varepsilon_1}k_1\exp(k_1 a) + \frac{D}{\varepsilon_1}k_1\exp(-k_1 a), \tag{3.52}$$

for interface $z = a$ and

$$B\exp(-k_2 a) = C\exp(-k_1 a) + D\exp(k_1 a), \tag{3.53}$$

$$-\frac{B}{\varepsilon_2}k_2\exp(-k_2 a) = -\frac{C}{\varepsilon_1}k_1\exp(-k_1 a) + \frac{D}{\varepsilon_1}k_1\exp(k_1 a), \tag{3.54}$$

for interface $z = -a$ and furthermore H_y has again to fulfill wave Equation (3.16) in all three regions. This is satisfied by

$$k_i^2 = \beta^2 - k_0^2\varepsilon_i, \tag{3.55}$$

where $i = 1, 2, 3$.

The solution of this system of linear equations is a dispersion relation which links propagation constant β with angular frequency ω [15, p. 31]

$$\exp(-4k_1 a) = \frac{k_1/\varepsilon_1 + k_2/\varepsilon_2}{k_1/\varepsilon_1 - k_2/\varepsilon_2}\,\frac{k_1/\varepsilon_1 + k_3/\varepsilon_3}{k_1/\varepsilon_1 - k_3/\varepsilon_3}. \tag{3.56}$$

Assuming $k_1 = k_3$ and $\varepsilon_1 = \varepsilon_3$, this dispersion relation simplifies to

$$\tanh(k_1 a) = -\frac{k_2\varepsilon_1}{k_1\varepsilon_2}, \tag{3.57}$$

$$\tanh(k_1 a) = -\frac{k_1\varepsilon_2}{k_2\varepsilon_1}. \tag{3.58}$$

It can be shown that Equation (3.57) describes a situation, when $E_x(z)$ is expressed by odd function and H_y and E_z by even functions, and Equation (3.58) describes a situation, when $E_x(z)$ is expressed by even function and H_y and E_z by odd functions.

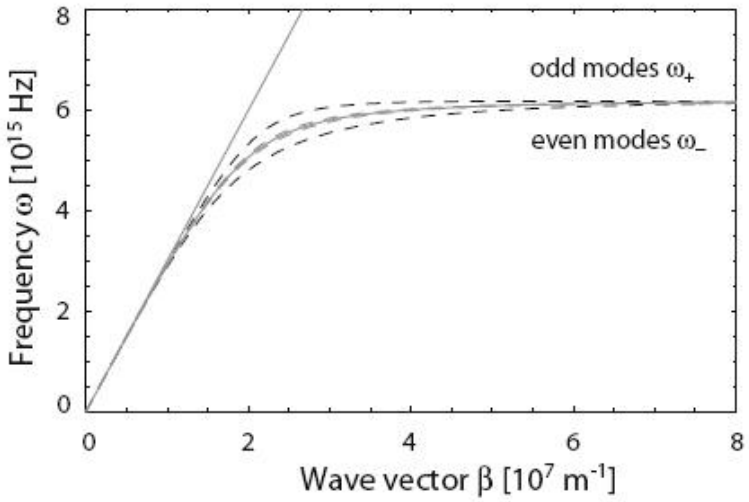

Figure 3.4: Dispersion relation for odd (ω_+) and even (ω_-) modes of SPPs (dashed lines) for the air-silver-air multilayer. Thickness of the silver layer is 50 nm. The grey curve is the dispersion relation for SPPs at the interface between silver and air. Taken from [15].

Now, let us consider a multilayer insulator-metal-insulator, where metallic layer ($\varepsilon_1(\omega)$ of thickness $2a$ is surrounded from both sides by the dielectric of real and positive dielectric constant ε_2 (see figure 3.3). Using the dispersion relations (3.57) and (3.58) we find that this multilayer allows to emerge two modes of SPPs, odd and even modes[4] [15].

In the Figure 3.4, there is a dispersion relation of odd and even SPP modes for a multilayer air-silver-air. As can be seen, the frequency of odd SPP modes ω_+ is higher than the corresponding frequency of SPP at a single interface air-sliver. On the contrary, the frequency of even modes ω_- is lower than the corresponding frequency of SPP at a single interface air-silver. For high values of propagation constant β we get limiting frequencies

$$\omega_+ = \frac{\omega_p}{\sqrt{1+\varepsilon_2}}\sqrt{1+\frac{2\varepsilon_2\exp(-2\beta a)}{1+\varepsilon_2}}, \tag{3.59}$$

$$\omega_- = \frac{\omega_p}{\sqrt{1+\varepsilon_2}}\sqrt{1-\frac{2\varepsilon_2\exp(-2\beta a)}{1+\varepsilon_2}}. \tag{3.60}$$

[4]However, the nomenclature for identifying the modes varies greatly throughout the literature [22].

4 Localized surface plasmon polaritons

In Section 3.3, the propagation of SPPs at the interfaces of an insulator-metal-insulator (IMI) multilayer was described. There was stated that the plasmonic resonant antennas are a specific case of IMI multilayer which is spatially limited. The x and y dimensions of IMI multilayer in Section 3.3 was considered infinite. However the dimensions of plasmonic resonant antennas are finite in all directions. Now, we will investigate what happens when the x dimension of IMI multilayer is finite (see Figure 4.1).

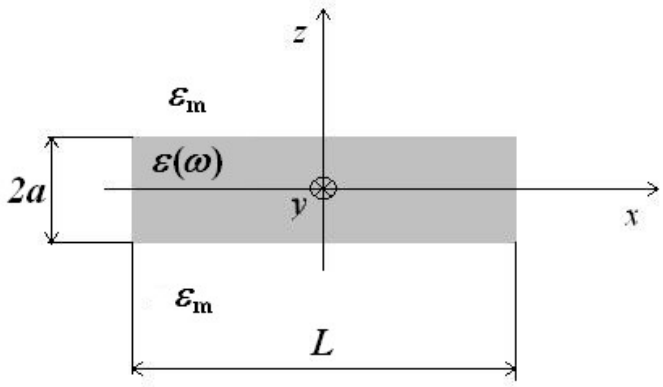

Figure 4.1: Insulator-metal-insulator multilayer. The interfaces are situated at $z = \pm a$ and $x = \pm L/2$. The y dimension of the multilayer is infinite.

Now, let us assume that surface plasmon polaritons propagates along the interface between metal and dielectric in the x direction. However, x dimension of the interface is now finite, so at the end of the interface ($x = \pm L/2$) these modes reflect back. The reflection at the end of the interface can be in ideal case described as a wave reflection at the fixed end. Therefore, from the analogy with a mechanical wave on a string we can expect that standing electromagnetic wave emerge for specific wavelengths. Therefore, collective oscillations of conductive electrons do not propagate further off the finite interface, instead they are localized only in the region between $-L/2 \leq x \leq L/2$. The optical properties of these localized modes differ from the properties of propagating SPPs, therefore to distinguish between these two modes, those spatially localized have been called the *localized surface plasmon polaritons* or shorter *localized surface plasmons* (LSPs).

Spatial localization of collective oscillations of conductive electrons (LSP) has some serious consequences. First, the excitation of LSPs is a natural effect of light scattering by small sub-wavelength conductive particles. Therefore, in contrast to the excitation of SPPs[1], no special techniques are required for excitation of LSPs, as they arise naturally upon illumination.

[1]It can be seen from Figures 3.2c and 3.4 that there exist a mismatch between the wavevector of light and SPPs of the same frequency. SPPs can be excited by light only, when this wavevector mismatch is compensated. This can be done by proper excitation technique that gives the light an extra wavevector (prism coupling, grating coupling, illumination of sharp tip, etc.).

Another consequence is that for specific wavelengths of illuminating light, standing electromagnetic waves are formed in the particle and localized surface plasmons resonance (LSPR) occurs. The condition of resonance[2] is given by the existence of standing wave and for rod-like[3] particles it can be expressed as [23]

$$\lambda_{\mathrm{r},j} \cong \frac{2n_{\mathrm{eff}}L}{j}, \tag{4.1}$$

where λ_r is the resonant wavelength, n_{eff} is the effective refractive index (real part), L is length of the particle and $j = 1, 2, 3, \ldots$ denotes the mode of resonance. It should be emphasized that this equation is valid only in spectral region, where materials of particles (metals) have good metallic properties ($\Re\{\varepsilon_1\} \ll 0$) Otherwise, the situation is more complicated and sophisticated analytical models which will be shown later in this chapter have been developed to describe the resonance effects of rod-like particles.

There are two main effects of LSPR resonance. One is the electric field enhancement inside and in the near-field zone outside the particle. The other is the enhancement of light absorption and scattering by the particle [15, p. 65]. In systems described in this thesis, the LSPR resonance occurs at optical (i.e. visible or infrared) wavelengths. At these wavelengths metals are lossy materials. Therefore, unless a special treatment of substrate [24] or arrangement of particle ensemble [25] is used, the resonance peaks are broad and the resonant effects are noticeable in relatively broad interval of wavelengths (full width at half maximum of resonant peak varies from approx. 100 nm in visible to units of μm in mid-infrared (mid-IR) region).

We have shortly introduced LSPR resonance and relating phenomena and now we turn our attention at the electric near-field enhancement and light scattering in more detail using the quasi-static approximation.

4.1 Quasi-static approximation

Interaction of particles of dimension a with electromagnetic wave $\vec{E}_0$ of wavelength λ can be described by the quasi-static approximation method, with the assumption that the typical particle dimension a is much smaller than wavelength of an incoming wave, i.e. $a \ll \lambda$. For such particles it is possible to assume that the phase of the field is constant over the whole volume of the particle and therefore any retardation effects inside the particle can be neglected.

However, for particles of bigger dimensions, it is no longer possible to neglect the retardation effects, because the phase of the field over the whole volume of the particle is no longer constant. For these particles Mie theory [10] has to be used. Unfortunately, the analytical approach of Mie theory can describe only the interaction of electromagnetic field with particles of spherical or ellipsoidal shape. Plasmonic antennas usually have the

[2]It should be noted here that as *resonance* we mean the fulfillment of conditions necessary for the existence of standing wave. Later in this chapter, we will mention *material resonance* condition, known as Fröhlich condition.

[3]One dimension (length) of the particle is significantly bigger than others.

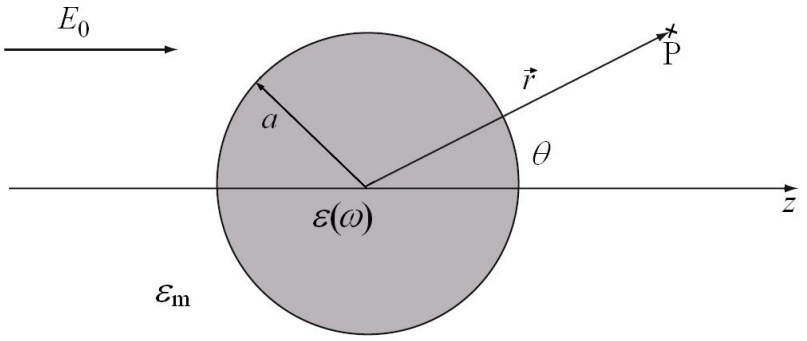

Figure 4.2: Homogeneous sphere of radius a in an electrostatic field. Taken from[15].

shape of rods or bars, so their interaction with electromagnetic field cannot be analytically described using this theory.

In following, we will describe the electric field around metallic spherical particle [$\varepsilon(\omega)$] located in isotropic non-absorbing dielectric medium (ε_m) using quasi-static approximation approach from [15, p. 66-72] which exploits boundary value problem in dielectric from [13, p. 154-159]. The arrangement of the situation is shown in Figure 4.2, where particle of radius a is illuminated from $-z$ direction by electromagnetic wave of amplitude E_0 and wavelength λ. As in the quasi-static approximation, we have assumed that $a \ll \lambda$, the phase is constant over the volume of particle which converts this situation to the task in electrostatics. This simplification can be used for the description of light-particle interaction in case of particles of dimensions approximately up to 100 nm [15, p. 66].

In order to find the electric field distribution around the particle, we are interested in the solution of Laplace equation for the electric potential $\nabla^2\Phi = 0$ which enables us to find the electric field $\vec{E} = -\nabla\Phi$. As the problem has azimuthal symmetry, solution is in form of the Legendre polynomials [13, p. 157]

$$\Phi(r,\theta) = \sum_{l=0}^{\infty}[A_l r^l + B_l r^{-l+1}]P_l(\cos\theta), \tag{4.2}$$

where $P_l(\cos\theta)$ are the Legendre polynomials of order l and θ is the angle between position vector $\vec{r}$ and z axis. Applying the requirement of finite potential at the origin, potentials inside Φ_{in} and outside Φ_{out} the spherical particle can be described in following way

$$\Phi_{\text{in}}(r,\theta) = \sum_{l=0}^{\infty} A_l r^l P_l(\cos\theta), \tag{4.3}$$

$$\Phi_{\text{out}}(r,\theta) = \sum_{l=0}^{\infty}[B_l r^l + C_l r^{-l+1}]P_l(\cos\theta). \tag{4.4}$$

Coefficients A_l, B_l and C_l can be determined from the boundary conditions at infinity ($r \to \infty$) and at the particle surface ($r = a$). Applying the boundary conditions (2.26) and (2.28) expressed for potential (see [13, p. 157]) together with the requirement that $\Phi_{\text{out}} \to -E_0 z = -E_0 r\cos\theta$ for $r \to \infty$ leads to [13, p. 158]

$$\Phi_{\text{in}} = -\frac{3\varepsilon_{\text{m}}}{\varepsilon + 2\varepsilon_{\text{m}}} E_0 r\cos\theta, \tag{4.5}$$

$$\Phi_{\text{out}} = -E_0 r\cos\theta + \frac{\varepsilon-\varepsilon_{\text{m}}}{\varepsilon+2\varepsilon_{\text{m}}}E_0 a^3\frac{\cos\theta}{r^2}. \tag{4.6}$$

Equation (4.6) describes the superposition of the applied external field with the field of the dipole located at the centre of the particle. The relation for Φ_{out} can be rewritten by introduction of the dipole moment $\vec{p}$ as

$$\vec{p} = 4\pi\varepsilon_0\varepsilon_{\text{m}}a^3\frac{\varepsilon-\varepsilon_{\text{m}}}{\varepsilon+2\varepsilon_{\text{m}}}\vec{E_0}, \tag{4.7}$$

$$\Phi_{\text{out}} = -E_0 r\cos\theta + \frac{\vec{p}\cdot\vec{r}}{4\pi\varepsilon_0\varepsilon_{\text{m}}r^3}. \tag{4.8}$$

We see that the applied field $\vec{E_0}$ induces a dipole moment $\vec{p}$ inside the sphere. The magnitude of $\vec{p}$ is proportional to E_0. By rewriting dipole moment $\vec{p}$ using the quantity of polarizability

$$\alpha = 4\pi a^3\frac{\varepsilon-\varepsilon_{\text{m}}}{\varepsilon+2\varepsilon_{\text{m}}}, \tag{4.9}$$

we get $\vec{p} = \varepsilon_0\varepsilon_{\text{m}}\alpha\vec{E_0}$. The equation (4.9) expresses static polarizability of the sub-wavelength sphere. From the denominator of (4.9) it is apparent that the polarizability has resonant enhancement when the denominator $|\varepsilon+2\varepsilon_m|$ reaches its minimum. This can be simplified for materials with slowly-varying $\Im\{\varepsilon\}$, when this resonant condition[4] can be rewritten into the Fröhlich condition

$$\Re\{\varepsilon(\omega)\} = -2\varepsilon_{\text{m}}. \tag{4.10}$$

The electric field inside and outside the particle $\vec{E} = -\nabla\Phi$ can be expressed from (4.5) and (4.6) in following form

$$\vec{E}_{\text{in}} = \frac{3\varepsilon_{\text{m}}}{\varepsilon+2\varepsilon_{\text{m}}}\vec{E_0}, \tag{4.11}$$

$$\vec{E}_{\text{out}} = \vec{E_0} + \frac{3\vec{n}(\vec{n}\cdot\vec{p})-\vec{p}}{4\pi\varepsilon_0\varepsilon_{\text{m}}}\frac{1}{r^3}, \tag{4.12}$$

where $\vec{n}$ is the unit vector in the direction of position vector ($\vec{n} = \vec{r}/|\vec{r}|$).

The maximum of their polarizability α implies the resonance of dipole moment and also the resonance of dipolar electric field inside and outside the particle which is therefore the consequence of LSPR. In the case of gold and silver, the resonance of polarizability falls in the visible region of the electromagnetic spectrum [15, p. 65] which makes these materials suitable for applications based both, on utilizing LSPR induced dipolar field and scattering enhancement.

Now, still using the quasi-static approximation, we will describe the dipolar electromagnetic field radiated from the spherical particle of radius $a \ll \lambda$ at its plasmon resonance.

[4]The resonant condition mentioned here is the *material* one. This means that the resonance (maximum of polarizability α, dipole moment $\vec{p}$, potential Φ_{in} and electric field $\vec{E}_{\text{in}}$ inside and outside the particle Φ_{out} and $\vec{E}_{\text{out}}$) is governed by the dielectric functions of media.

The particle is illuminated by plane wave $\vec{E}(\vec{r},t) = \vec{E}_0 \exp(-\mathrm{i}\omega t)$ which induces dipolar moment $\vec{p}(t) = \varepsilon_0 \varepsilon_\mathrm{m} \alpha \vec{E}_0 \exp(\mathrm{i}\omega t)$ in the particle. The radiation of this dipole leads to the scattering of the incident plane wave by the particle. The total time-harmonic electromagnetic field ($\vec{H}(t) = \vec{H}\exp(-\mathrm{i}\omega t), \vec{E}(t) = \vec{E}\exp(-\mathrm{i}\omega t)$) associated with the oscillating dipole are following [15, p. 69]

$$\vec{H} = \frac{ck^2}{4\pi\sqrt{\varepsilon_\mathrm{m}}}(\vec{n}\times\vec{p})\frac{\exp(\mathrm{i}kr)}{r}\left(1-\frac{1}{\mathrm{i}kr}\right), \tag{4.13}$$

$$\vec{E} = \frac{1}{4\pi\varepsilon_0\varepsilon_\mathrm{m}}\left\{k^2(\vec{n}\times\vec{p})\times\vec{n}\frac{\exp(\mathrm{i}kr)}{r} + [3\vec{n}(\vec{n}\cdot\vec{p})-\vec{p}]\left(\frac{1}{r^3}-\frac{\mathrm{i}k}{r^2}\right)\exp(\mathrm{i}kr)\right\}, \tag{4.14}$$

where $k = 2\pi/\lambda$. In the near zone of the particle (i.e. $kr \ll 1$), the fields (4.13) and (4.14) can be rewritten in the following form

$$\vec{E} \cong \frac{3\vec{n}(\vec{n}\cdot\vec{p})-\vec{p}}{4\pi\varepsilon_0\varepsilon_\mathrm{m}}\frac{1}{r^3}, \tag{4.15}$$

$$\vec{H} \cong \frac{\mathrm{i}\omega}{4\pi}(\vec{n}\times\vec{p})\frac{1}{r^2}. \tag{4.16}$$

In the far radiation zone ($kr \gg 1$) the dipolar fields (4.13) and (4.14) has the form of a spherical wave

$$\vec{H} \cong \frac{ck^2}{4\pi\sqrt{\varepsilon_\mathrm{m}}}(\vec{n}\times\vec{p})\frac{\exp(\mathrm{i}kr)}{r}, \tag{4.17}$$

$$\vec{E} \cong \sqrt{\frac{\mu_0}{\varepsilon_0\varepsilon_\mathrm{m}}}\vec{H}\times\vec{n}. \tag{4.18}$$

In the foregoing text, the electromagnetic field in and nearby the particle at LSPR has been dealt with. From the optical point-of-view, the other consequence of LSPR, the enhancement of particle-light interaction is more interesting and will be now briefly mentioned. The ability of particles to interact with electromagnetic radiation and thus to scatter or absorb the radiation is expressed by cross sections for scattering C_sca, absorption C_abs or extinction C_ext. The cross sections are calculated from the density of power flux (expressed by Poynting vector $\vec{S} = \vec{E}\times\vec{H}$, where $\vec{E}$ and $\vec{H}$ are given by equations (4.13) and (4.14)) in the vicinity of the particle [12, p. 140], [15, p. 71]

$$C_\mathrm{sca} = \frac{k^4}{6\pi}|\alpha|^2 = \frac{8\pi}{3}k^4a^6\left|\frac{\varepsilon-\varepsilon_\mathrm{m}}{\varepsilon+2\varepsilon_\mathrm{m}}\right|^2, \tag{4.19}$$

$$C_\mathrm{abs} = k\,\Im\{\alpha\} = 4\pi k\,a^3\Im\left\{\frac{\varepsilon-\varepsilon_\mathrm{m}}{\varepsilon+2\varepsilon_\mathrm{m}}\right\}, \tag{4.20}$$

$$C_\mathrm{ext} = C_\mathrm{abs} + C_\mathrm{sca} \approx C_\mathrm{abs} = 9\frac{\omega}{c}\varepsilon_\mathrm{m}^{3/2}V\frac{\Im\{\varepsilon\}}{[\Re\{\varepsilon\}+2\varepsilon_\mathrm{m}]^2+\Im\{\varepsilon\}^2}. \tag{4.21}$$

The Fröhlich condition can be seen again in the denominators of cross sections, this implies that the cross sections have maximum values when the particle polarizability is at its maximum, i.e. at LSPR. The scattering efficiency scales with a^6, while the absorbtion

scales with a^3. The consequence of this is that for particles with radius $a \ll \lambda$ absorption dominates over scattering and therefore it is difficult to detect the scattering signal from very small particles during experimental measurements and measurements of extinction are usually more useful.

4.2 Mie theory

One of the stumpers of early 20$^{\text{th}}$ century physics was the explanation of different colours of gold colloids. Several theories were published to explain it [11], but all had a common weakness; they were able to explain one or more colours of gold colloids, but not all of them. In 1908, Gustav Mie published his seminal paper on light scattering and absorption by a small spherical particle [10]. In the paper, Mie had built complete analytical theory (nowadays called the Mie theory) describing the interaction of light with a spherical particle and used it to explain all the colours of gold colloids.

As it has been already mentioned before, Mie theory can only be used for exact analytical description of the interaction of light with particles of spherical or ellipsoidal shape. All the plasmonic antennas presented in this thesis has rod-like shape[5], when one dimension (length) is significantly bigger than the other two. For none of these antennas Mie theory can be applied without approximations. Therefore, instead of introducing the Mie theory in detail (which can be, for example, seen in [12, p. 83–114]), we will settle with a very brief qualitative description.

The Mie theory represents a rigorous electrodynamic approach to the problem of light scattering by a sphere. The approach of the Mie theory is to utilize vector spherical harmonic functions (odd and even) for the expression of electric and magnetic components of the field using the *generating function* which satisfies the electromagnetic wave equation in spherical coordinates. To describe the interaction of applied light plane-wave with the sphere, the incoming plane wave is expanded into an infinite series of vector spherical harmonics and also the internal and scattered electric and magnetic field is expanded in the same way. The terms of the series then represent so-called *normal modes* of the sphere. The quasi-static approximation results can be then recovered by a power series expansion of absorption and scattering coefficients and retaining only the first term of the expansion [15, p. 73].

4.3 Plasmonic antennas

As we have already mentioned in Chapter 1 the structures which exhibit the resonance of localized surface plasmons due to the external illumination are often called plasmonic *antennas*, due to its similarity to macroscopic electromagnetic antennas.

An optical plasmonic antenna can effectively convert the energy of propagating radiation into the localized energy and vice versa. From microscopic point-of-view, the optical antenna effectively replaces a focusing lens (or an objective), as it concentrates the incident

[5] Only in a few *extreme* cases, the antennas have similar dimensions or they have cubic shape.

radiation to dimensions much smaller than diffraction limit. Unlike most of its radio- and microwave counterparts, the optical antenna can act both as a receiver for localizing of the incoming energy and as a transmitter for emitting of the optical response in the same time [9].

The main challenge of an efficient antenna design is the coupling of electromagnetic power flow between the near- and far-field of the source (or receiver). One of the most efficient antenna designs for optical frequencies are rod-like half-wave dipole antennas [26] and bow-tie antennas [23]. However, when one is interested in LSPR, then any metallic nanostructure can be viewed as an optical antenna [9]. For spectral regions, where metals act as a good conductor, the LSPR wavelength λ_r of half-wave dipole antennas can be estimated by modified formula for half-wave dipole (Eq. 4.1, where $j = 1$)

Several reviews have been published on plasmonic antennas in last few years [27], [28], [29] which proof the interest of scientific community in this field. With the development of sophisticated fabrication techniques and instruments which allow a precise fabrication and a good reproducibility of fabricated structures, optical plasmonic antennas became utilized both for their near-field enhancement and scattering (absorption) properties in near-field optical microscopy [30], [31], [32], Raman spectroscopy [33], [34], [35], [36], infrared spectroscopy [37], [38], sensing applications [39], [40], [41], photovoltaics [42], [43], optical device architectures [44], [45], [46], light coupling [47], [48], luminescence enhancement [49], optical trapping [50], [51] and even cancer therapy [52].

4.3.1 Resonant properties of plasmonic antennas

Now, we will shortly discuss the resonant properties of plasmonic antennas. In the foregoing text on localized surface plasmons we introduced two resonant conditions; *material* (Fröhlich) condition (Eq. 4.10) and *geometrical* condition of existence of standing waves in the rod-like antenna (Eq. 4.1). The latter means that for rod-like plasmonic antennas, there always exists the wavelength for which light scattering by the antenna as well as electric field in the antenna near zone is enhanced due to LSPR. Simultaneous fulfillment of Fröhlich condition (4.10) then increases the resonant effects, but it is not essential for the existence of LSPR in the antennas.

Therefore, by the term *resonant properties* of antenna we mean the wavelength of standing waves corresponding to dipolar polarization of antenna, i.e. the wavelength of LSPR, the value of antenna scattering cross section at LSPR and the value of enhancement of electric field in the close vicinity of the antenna at LSPR.

4.3.2 Analytical models for resonance of rod-like plasmonic antennas

A classical antenna design assumes no time lag between the reactions of conductive electrons on incoming electromagnetic field. A consequence of this assumption is no penetration of electromagnetic field into the metal (no skin effect). However, at optical frequencies, the electromagnetic field penetrates into metals and skin effect cannot be neglected. The main result of this feature is that LSPR wavelength is no longer a simple function of the antenna geometry, like the one expressed by equation (4.1). Therefore,

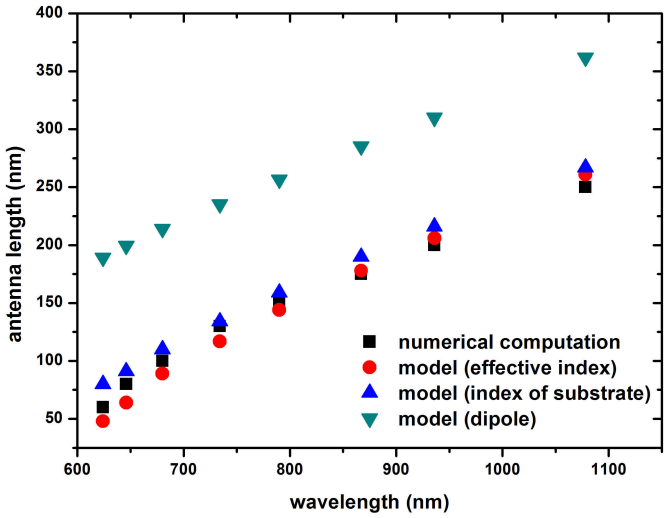

Figure 4.3: Antenna length as a function of the specific LSPR wavelength - comparison of models for a single rod-like gold antenna on a silica substrate. The black squares show the results of numerical computation, red circles the results of an analytical model according to [53] using the effective refractive index in the model, blue triangles show the results of the same model using the refractive index of the substrate (silica) instead of the effective index and turquoise triangles correspond to the results for a classic half-wave dipole model according to Equation (4.1), with $j = 1$. Antenna designed in our numerical computations has the shape of a bar with both width and height of 60 nm, thus the corresponding radius R used in computation according to Novotny's model [53] was $R = 30\,\mathrm{nm}$. With the exception of the smallest antennas, where the condition $R \ll L$ required by the model is not satisfied, both models based on [53] and our numerical computation give similar results, while the dipole approach fails.

antenna dimensions cannot be directly scaled down from the radio- or microwave region to the optical one. The solution of this issue is possible by implementation of one of several analytical models like those in [53], [54].

In model of Novotny [53], the waveguide theory is applied on the problem of plasmonic antenna resonance. According to Novotny, the resonance of very thin antennas (length L, radius R, $R \ll L$) does not occur at the *predicted* wavelength[6] λ_r, but rather at the effective wavelength λ_eff which is linearly scaled with λ_r. The scaling rule of resonant wavelength in Novotny's model is

$$\lambda_\mathrm{eff} = a_1 + \frac{a_2}{\lambda_\mathrm{p}}\lambda_\mathrm{r}, \tag{4.22}$$

where λ_p is plasma wavelength[7] of antenna material and a_1 and a_2 are coefficients (with a dimension of length) which depends on antenna geometry (length and radius) and dielectric properties of surrounding medium. The exact relation for calculation the values of a_1 and a_2 can be found in [53].

[6] Equation (4.1), $j = 1 \rightarrow \lambda_r = 2n_\mathrm{eff}L$.

[7] Plasma wavelength corresponds to plasma frequency ω_p, $\lambda_\mathrm{p} = 2\pi c/\omega_\mathrm{p}$, where c is the speed of light in vacuum.

Model of Kalousek [54] uses different approach to find the resonant wavelength λ_r of very thin antennas[8] upon normal illumination. Using the quasi-static approximation (requesting $R \ll \lambda$) together with the assumption of uniform charge distribution over the transversal antenna cross section[9], the density of free-electron Lagrangian is calculated and then used in Euler-Lagrange equation, from which the wave equation is derived. From the wave equation, the phase velocity of longitudinal free-electron density waves (i.e. surface plasmons) is calculated and subsequently used for the determination of localized surface plasmon eigenfrequencies, i.e. frequencies of standing electromagnetic waves in the antenna. The final relation for resonant wavelength of a very thin antenna is then

$$\lambda_{\mathrm{r},j} = \frac{2\lambda_\mathrm{p}}{j\pi}\frac{L}{R}\left[\ln\left(\vartheta\frac{L}{R}\right)\right]^{-1/2}, \tag{4.23}$$

where $j = 1, 2, 3, \ldots$ is the mode of resonance and $\vartheta = 2\mathrm{e}^{-1/2}$. Moreover, model of Kalousek also deals with polarizability of thin antennas at resonance which is then used for the analytical expression of antenna near-field.

The fail of classical half-wave dipole model (Eq. 4.1, $j = 1$) is obvious in Figure 4.3, where the result given by classical model are compared with the results of Novotny's model [53] and result given by numerical calculation in commercial solver[10].

Despite the issues with direct scaling down of antenna geometry, existing antenna designs can still inspire the design of their optical counterparts as can be seen from the application of well-known Yagi-Uda antenna design for antennas at optical frequencies [47], [55], [56], [57].

[8] Radius R of the antennas is smaller than the skin depth of the metal.

[9] Here, the cross section of the antenna is transversal, i.e. perpendicular to the main symmetry (length) axis of the antenna. Definitely, it should not be confused with geometrical cross section of the antenna which is sometimes used in quantification of scattering, absorption or extinction effect of the antenna.

[10] The method of numerical calculation, as well as the solver which was used, will be introduced in the following chapter.

5 Numerical computations

In Chapter 4, we used quasi-static approximation to present the analytical approach for expression of subwavelength spherical particle response to illumination. In addition, we introduced two analytical models for the description of the response of very thin rod-like antennas. However, when no analytical approach is possible to use (which happens very often), then numerical calculations represent a powerful tool to determine the response of structures of different dimensions and shapes. One of numerical methods for solving Maxwell's equations is the Finite-Difference Time-Domain (FDTD) method.

5.1 Finite-Difference Time-Domain method

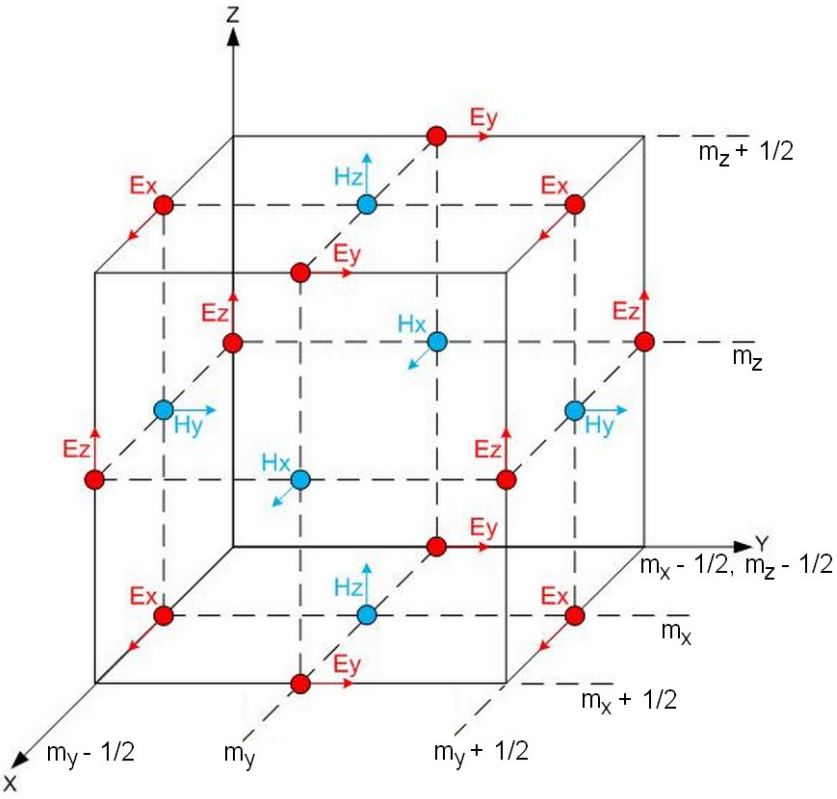

Figure 5.1: A visualization of an usual 3D Yee cell of spatial indices (m_x, m_y, m_z). Magnetic components of the field are computed at the centre of cell faces, electric components at the centre of cell edges. Taken from [58]. It is also possible (but unusual) to calculate the magnetic components at the centre of edges and the electric components at the centre of faces; the FDTD method then works in the exactly same way [59].

An algorithm of FDTD computation method was developed by Yee in 1966 [60]. However the designation *finite-difference time-domain* was firstly used by Taflove in 1980 [59]. Nowadays, the FDTD computation method has become a widespread method for the solution of Maxwell's equations in complex geometry [61], [62]. The FDTD method is based on a temporal and spatial discretization of the following two curl Maxwell's

equations (i.e. on the replacement of the derivatives by finite differences) and an electric field material equation for a non-magnetic medium:

$$\frac{\partial \vec{D}}{\partial t} = \nabla \times \vec{H}, \tag{5.1}$$

$$\frac{\partial \vec{H}}{\partial t} = -\frac{1}{\mu_0} \nabla \times \vec{E}, \tag{5.2}$$

$$\vec{D}(\omega) = \varepsilon_0 \varepsilon_r(\omega) \vec{E}(\omega). \tag{5.3}$$

The space is discretized using an ensemble of block shape cells, known as Yee cells [60]. One of them is shown in Figure 5.1. The block shape of cells, together with the spatial and temporal interleaving of cell points, where electric- and magnetic field is calculated (see Figure 5.1), ensure that conditions given by other two divergence Maxwell's equations (2.1) and (2.2) are implicitly met [63], and therefore they are not calculated.

Using the approach from [61], we are going to demonstrate the principles of FDTD method on a simple one-dimensional example of electric wave propagation. Let us assume that there exists a linearly polarized electromagnetic wave which propagates in the positive direction of z axis. The electric field vector $\vec{E}$ oscillates in the direction of x axis and magnetic field vector $\vec{H}$ in y axis direction. First, we carry out the spatial and temporal discretization. We introduce indices m and n, which we utilize in discretization of space and time in such way that m^{th} spatial step and n^{th} temporal step will be connected to absolute position z and time t as follows:

$$z_m = m\Delta z, \tag{5.4}$$

$$t_n = n\Delta t. \tag{5.5}$$

A proper settings of spatial and temporal step sizes Δz and Δt is important. A size of the spatial step is usually governed by the wavelength of illuminating radiation. In general, the size of the spatial step should be smaller that one tenth of the wavelength, but when one is interested in calculations of the field from subwavelength structures, then the size of the spatial step has to be reduced well below the dimensions of the structures. Also, for the modeling of a curved surface, it is often necessary to refine the block-shaped mesh of cells by the reduction of spatial step Δz.

The size of temporal step Δt is governed by the Courant stability condition. The expression of temporal step, which is linked to size step Δz, is following

$$\Delta z \leq \frac{\lambda}{10}, \tag{5.6}$$

$$\Delta t \leq \frac{\Delta z}{2c}, \tag{5.7}$$

where λ is the wavelength of the illuminating radiation and c is speed of light in vacuum. While the refinement of the spatial discretization usually results in more accurate results, the refinement of the temporal discretization below the stability condition (5.7) has, in most cases, no such effect.

For both the spatial and temporal discretization of electromagnetic field, we will use the central difference method. Partial spatial and temporal derivatives then can be expressed as

$$\frac{\partial E}{\partial z} \rightarrow \frac{\Delta E}{\Delta z} = \frac{E(m+\frac{1}{2}) - E(m-\frac{1}{2})}{\Delta z}, \tag{5.8}$$

$$\frac{\partial E}{\partial t} \rightarrow \frac{\Delta E}{\Delta t} = \frac{E(n+\frac{1}{2}) - E(n-\frac{1}{2})}{\Delta t}. \tag{5.9}$$

We use the same procedure for the discretization of magnetic field.

When we substitute Equations (5.8) and (5.9) into Maxwell's equations (5.1) and (5.2), we get Maxwell's equations in the following form

$$\frac{E_x^{n+\frac{1}{2}}(m) - E_x^{n-\frac{1}{2}}(m)}{\Delta t} = -\frac{H_y^n(m+\frac{1}{2}) - H_y^n(m-\frac{1}{2})}{\varepsilon_0 \Delta z}, \tag{5.10}$$

$$\frac{H_y^{n+1}(m+\frac{1}{2}) - H_y^n(m+\frac{1}{2})}{\Delta t} = -\frac{E_x^{n+\frac{1}{2}}(m+1) - E_x^{n+\frac{1}{2}}(m)}{\mu_0 \Delta z}. \tag{5.11}$$

Then, Equations (5.10) and (5.11) are alternatively solved in spatial and temporal steps. As it can be seen from these equations, the temporal development of one field in subsequent step is computed from the spatial development of the other field in previous step and vice versa. It is possible to calculate the field in a specific point in every time step from the values of the field in previous time step. To make this more evident we express the field in time step[1] of $(n+1)$ and $(n+\frac{1}{2})$. The Equations (5.10) and (5.11) has the following form

$$E_x^{n+\frac{1}{2}}(m) = E_x^{n-\frac{1}{2}}(m) - \frac{\Delta t}{\varepsilon_0 \Delta z}\left[H_y^n\left(m+\frac{1}{2}\right) - H_y^n\left(m-\frac{1}{2}\right)\right], \tag{5.12}$$

$$H_y^{n+1}\left(m+\frac{1}{2}\right) = H_y^n\left(m+\frac{1}{2}\right) - \frac{\Delta t}{\mu_0 \Delta z}\left[E_x^{n+\frac{1}{2}}(m+1) - E_x^{n+\frac{1}{2}}(m)\right]. \tag{5.13}$$

As FDTD belongs to time-domain methods, performing the Fourier transform during or after the calculations enables to obtain the solutions of the equations also in frequency or wavelength domain. Therefore, with FDTD method one can also calculate a full range of useful quantities as a normalized reflection or transmission, a complex Poynting vector and a far-field projections.

5.2 Lumerical FDTD Solutions package

All the simulations presented in this thesis were performed with Lumerical FDTD Solutions software, which utilizes the FDTD numerical method for the solution of Maxwell's equations in non-magnetic media. It is capable to analyze the interaction of UV, visible, and IR radiation with complicated structures employing wavelength scale features [64].

[1] Due to the temporal interleaving of the field, one field is calculated in time $t = (n+1)\Delta t$ and the other in $t = (n+\frac{1}{2})\Delta t$.

It would be pointless to discuss all the shapes, materials, radiation sources which can be modeled in this software as well as other features of Lumerical. The explanation of all the features of Lumerical can be found in the Lumerical knowledge base [63]. Specific features of Lumerical applied in the simulations presented in this thesis will be mentioned later in chapters devoted to simulations results. Now, we will discuss only two important features - continuous wave (CW) normalization and total-field scattered-field (TFSF) radiation source.

5.2.1 Continuous wave normalization

Sources of electromagnetic radiation in Lumerical FDTD solutions always inject a broadband pulse into the simulation area, even when one is interested in data for single specific wavelength or in the response of simulated system to continuous wave (CW) illumination. Therefore, the raw data of the electromagnetic field from the simulation are calculated in the time domain. To convert the data to the frequency domain (steady state corresponding to illumination by a continuous wave) a mathematical operation (called CW normalization) is employed to recalculate the response of the system to pulse illumination to the response to CW illumination.

To explain how CW normalization works we will use the Lumerical knowledge database [63]. Let us assume a harmonic modulated (monochromatic) Gaussian light pulse $s(t)$ shown in Figure 5.2

$$s(t) = \sin[\omega_0(t - t_0)] \exp\left(-\frac{(t - t_0)^2}{2(\Delta t)^2}\right) \tag{5.14}$$

and its Fourier transform $\mathcal{S}(\omega)$

$$\mathrm{FT}\{s(t)\} = \mathcal{S}(\omega) = \int_{-\infty}^{\infty} \exp(-\mathrm{i}\omega t) s(t) \mathrm{d}t. \tag{5.15}$$

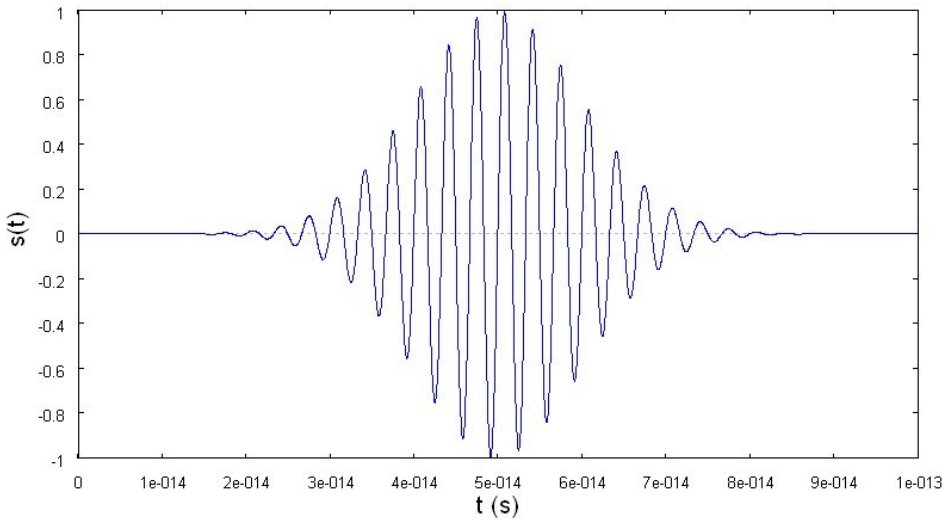

Figure 5.2: A visualization of a harmonic modulated Gaussian light pulse $s(t)$ given by Equation (5.14) for $\omega_0 = 1.885 \cdot 10^{15}\,\mathrm{s}^{-1}$ (which corresponds to $\lambda = 1\,\mu\mathrm{m}$), $t_0 = 50\,\mathrm{fs}$ and $\Delta t = 10\,\mathrm{fs}$. Plotted in a computer algebra system Maxima [65].

ω_0 represents the angular frequency of the incoming light, t_0 the temporal offset of the pulse (i.e. time, when the Gaussian envelope of the pulse reaches its maximum) and Δt is proportional to pulse length. Pulse $s(t)$ is similar to typical pulses employed by the Lumerical FDTD Solutions. However, Lumerical pulses are broadband (polychromatic), thus, they have a form of wave packets.

The power monitors of Lumerical FDTD solutions returns the response of simulated system to $s(t)$ as a function of frequency, so the electric field is expressed as

$$\vec{\mathcal{E}}(\omega) = \int_{-\infty}^{\infty} \exp(-\mathrm{i}\omega t)\vec{E}(t)\mathrm{d}t. \tag{5.16}$$

The response of the system is not only a function of angular frequency ω, but also a function of pulse $s(t)$. To get rid of the dependence of the response on pulse $s(t)$, the spectral response $\vec{\mathcal{E}}(\omega)$ has to be divided by spectral profile of the pulse $\mathcal{S}(\omega)$

$$\vec{\mathcal{E}}_{\mathrm{imp}}(\omega) = \vec{\mathcal{E}}(\omega)/\mathcal{S}(\omega). \tag{5.17}$$

By this approach, the field corresponding to pulse illumination is converted to the field, which would exist if CW light source, where all the frequencies have the same constant amplitude, was used. Therefore, the CW normalized data of the field $\vec{\mathcal{E}}_{\mathrm{imp}}$ shows the spectral response of the system which is independent on pulse shape or length. CW normalized data sets therefore return the impulse response of the simulated system [63].

To conclude, the electric field at the source injection plane is following

$$E(x, y, z, t) = E_0(x, y, z)s(t). \tag{5.18}$$

When CW normalization is applied, the results of simulation are recalculated to correspond to the following expression of the electric field at the source injection plane

$$E(x, y, z, \omega) = E_0(x, y, z), \tag{5.19}$$

so CW normalization removes any frequency dependence due to the finite pulse length of the source.

5.2.2 Total-field scattered-field source

Lumerical FDTD Solutions allows to employ several types of electromagnetic radiation sources. In most of the simulations, whose results are presented later in this thesis, the total-field scattered-field (TFSF) source was employed in the design of simulations as a source of electromagnetic radiation. Therefore, the basic principle of this source is worth of short introduction.

When TFSF source in employed as the light source in the simulation design, the simulation area is separated by TFSF boundary to two distinct regions, one containing *total field*, i.e. the sum of the incident field and scattered field, and the other containing only the scattered field (see Figure 5.3). The incident electromagnetic field has a shape of a plane-wave with the propagation vector perpendicular to the injection surface [63]. The injection surface represents one of TFSF boundaries.

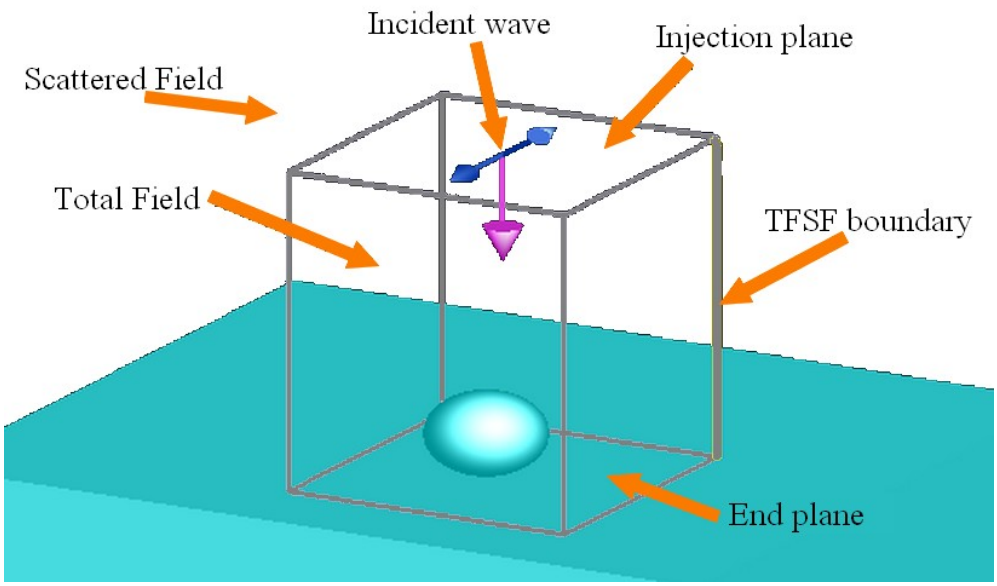

Figure 5.3: Illustration of a simulation area divided by the TFSF source (grey block). The total field is calculated inside the grey block, while outside the block, only the scattered field is calculated. The purple arrow shows the direction of propagation of the incident wave, while the blue arrows indicate its polarization. Taken from [63] and modified.

The incident plane-wave propagates from the injection surface through the area of TFSF source towards the side of TFSF boundary which is opposite to the injection side. At this opposite side of TFSF boundary, the incident plane-wave is subtracted from the total field, therefore, only the field scattered by defined structures inside the TFSF boundary propagates outside. The ability of TFSF source to distinguish between the total and the scattered field is especially valuable, when calculating the scattering effects of small structures like plasmonic antennas.

When the wavefront of propagating plane-wave is not parallel to the axis of mesh cells many numerical artifacts associated with plane-wave propagation in FDTD mesh can arise. These artifacts then cause errors in the field values and leakage of total field across the boundary of TFSF source. However, with the improvements of the definition of TFSF source as well as TFSF boundary, the leakage of total field across the boundary drops to 100 dB for obliquely orientation incident wavefront to axes of mesh cells. When special attention is paid to the design of FDTD mesh, the leakage can further drop even to 180 dB [66]. Such TFSF source improvement is included in the Lumerical code, therefore, the angle of illumination of the structure by TFSF source can be arbitrary [63].

6 Experimental techniques and materials

In this chapter, we will discuss the principal fabrication and measurement techniques which we used. The fabrication technique is represented by a multi-step technique of electron beam lithography (EBL). Here the substrate is coated by a film of electron sensitive substance which is patterned by electron beam, covered with desired material and dissolved in solvent. In final, only desired structures remain on substrate. The measurement technique belongs to Fourier transform infrared spectroscopy.

Last but not least, we will comment on the materials which were used as substrates for plasmonic antennas. In addition, some optical or mechanical features of these materials will be mentioned, especially how they influence the fabrication or measurement process.

6.1 Electron beam lithography

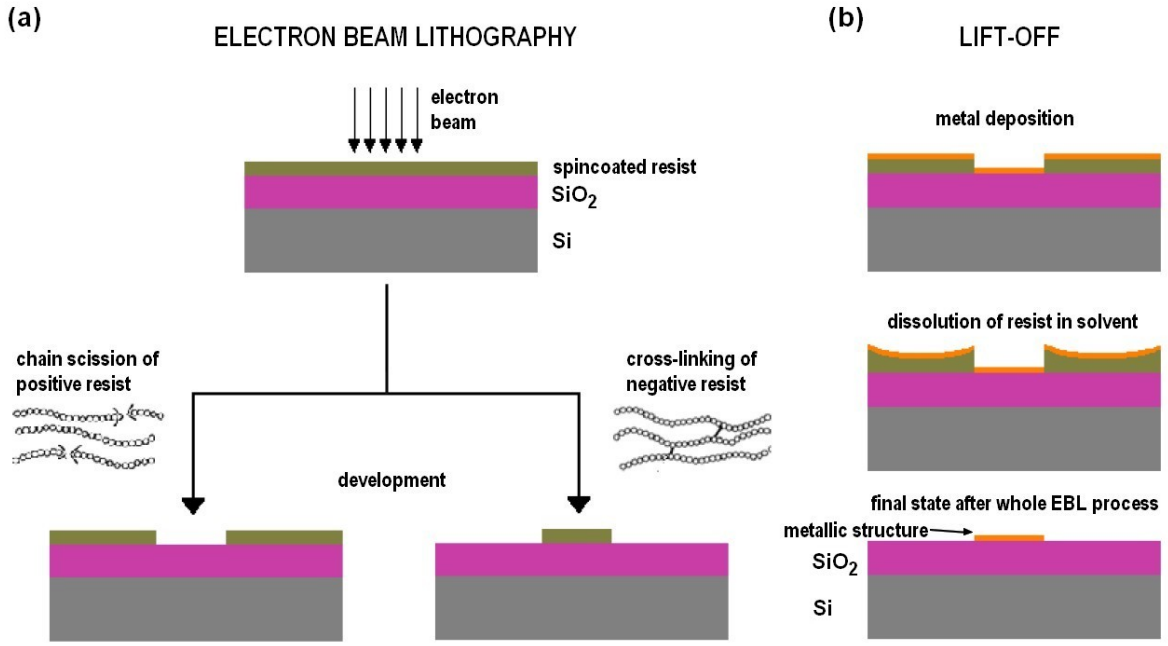

Figure 6.1: A scheme illustrating electron beam lithography using a positive or negative resist on a silicon substrate (a) and lift-off process after the metallization of exposed samples (b). Taken from [67] and modified.

In general, the EBL technique consists of several partial steps. The first step represents a spin-coating of a lithographic resist (usually an electron sensitive polymer) on a substrate which is later exposed to an electron beam in areas precisely defined by the mask drawn in a lithographic software. The electron beam interacts with a resist, this leads to a polymer chain scission for positive resists or to a polymer crosslinking for negative resists.

The next step is the development, when the sample is immersed into the developer. The developer causes the dissolution and removal of the exposed areas of resist (for positive resists) or non-exposed areas (for negative resists). During the development a resist mask is created at the substrate surface.

The final step of EBL can be represented either by a transfer of the pattern from the mask to the substrate by a wet or dry etching, or structures can be fabricated on the substrate surface by material deposition techniques which is then followed by the dissolution (lift-off) of the remaining resist.

The size limit of fabricated structures is mainly determined by the limited spatial resolution of used lithographic resist and by the grain size of the deposited material (usually a metal). When the size of fabricated metallic structures is very small (e.g. tens of nanometres), these polycrystalline structures consist of a few grains only and therefore can be easily damaged during the lift-off proces. The electron beam spot size can be as small as a few units of nanometres (in conventional scanning electron microscopes), which is far below the spatial resolution of resists. The area exposed by the electron beam is in reality bigger than the size of the beam spot due to the proximity effect [68]. However, the dimensions of fabricated slab-like structures which are presented later in Chapters 8 and 9 are hundreds of nanometers and more. Therefore, the beam shape and proximity effect do not posses a serious issue for fabrication of these structures.

6.1.1 EBL implementation

We used several materials as a substrate; silicon (Si), nanocrystalline diamond (NCD) film on fused silica (SiO_2) and calcium fluoride (CaF_2). The properties of all these substrates are discussed later in this chapter. Substrates were pre-baked on a hot plate at 180 °C. We used 4% solution of polymethyl methacrylate (PMMA) in anisole as a lithographic resist. The relative molecular weight of used PMMA was $4.95 \cdot 10^5$. The bad resist adhesion to CaF_2 substrates was improved by spin-coating (2000 rpm for 30 s) of MicroChem (MCC) Primer 80/20 prior to PMMA. The spin-coating of the resist on substrate was realized by Laurell 400 spin-coating device. The parameters of the spin-coating were 4000 rpm for 30 s for Si and NCD substrates, and 2000 rpm for 30 s for CaF_2. The presence of coated thin film changed the visual appearance of Si and NCD substrates, therefore, the naked eye inspection was sufficient to confirm the successful coating. However in case of transparent substrates like CaF_2, no change of an appearance is usually observed. Thus, we used a reflectometric technique to confirm the presence of the resist. The estimated thicknesses of spin-coated films were 170 nm for Si and NCD and 210 nm for CaF_2 substrates [69]. Coated substrates were baked again at 180 °C for 90 s to harden the resist film. To prevent charging of non-conductive substrates (CaF_2) during the EBL the resist was covered by a thin film of conductive polymer Espacer 300z (2000 rpm for 30 s).

During the EBL, substrates were exposed to 30 keV electron beam in a conventional scanning electron microscope (SEM) Tescan Vega2 or Tescan Lyra3. After a series of tests, the optimal electron dosage was determined to 265 $\mu C/cm^2$. Exposed samples were developed for 90 s in a mixture of methyl isobutyl ketone (MIBK) and isopropanol (IPA)

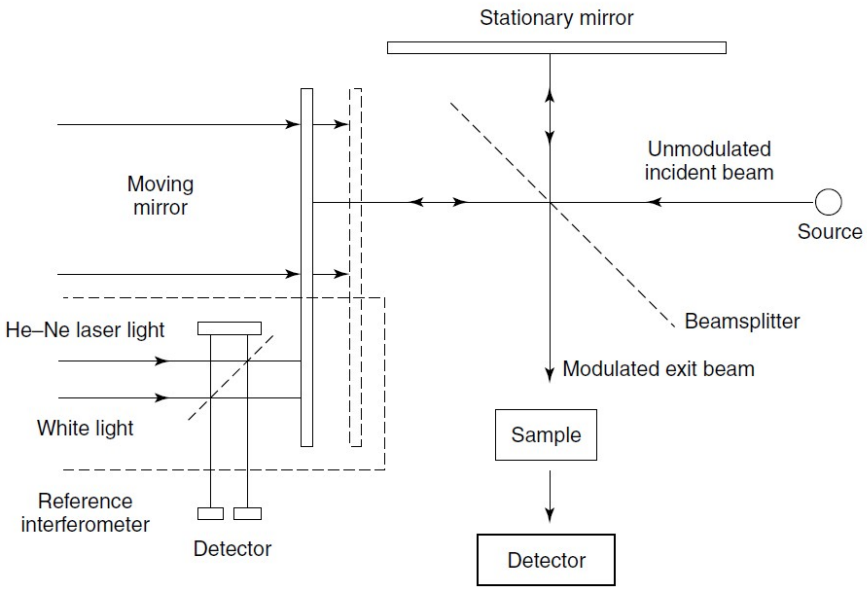

Figure 6.2: Schematic of the Michelson interferometer with a moving mirror. Taken from [70].

in 1:3 ratio followed by rinsing in pure IPA for 30 s and demineralized (DeMi) water for 60 s.

In the next step, developed samples were metallized. We used an ion beam assisted deposition (IBAD) to deposit 3nm-thick film of titanium and 60nm-thick gold film. A titanium buffer film improves the adhesion of a gold film to the substrate. Metallized samples were put into a beaker with acetone and left overnight for a lift-off process. On the next day, the samples were rinsed by acetone, IPA and DeMi water from wash bottles. In several cases, an ultrasonic bath was also applied to improve the resist stripping.

6.2 Fourier Transform Infrared Spectroscopy

The Fourier transform infrared spectroscopy has become a widely used technique for rapid microscopic analysis with the accuracy and sensitivity impossible to achieve by classic wavelength dispersive spectrometers [71]. A conventional dispersive method is based on dispersion of the incident light on a prism or grating. The energy of the incident radiation is varied over a desired range and a response is plotted as a function of frequency of the incoming radiation.

In Fourier transform spectroscopy, the Michelson interferometer (shown in Figure 6.2) with a suitable beamsplitter (made of potassium bromide (KBr) for near- and mid-IR spectral regions) is usually employed. The sample is exposed to a short pulse of incoming broadband radiation (for near- and mid-IR range usually coming from a heated silicon carbide bar, usually called Globar[1]) [70].

[1]The term *Globar* originates from the term *glowing bar* and in fact, it is a registered mark of the Swedish Sandvik engineering group, which refers to its silicon carbide heating elements as to Globar.

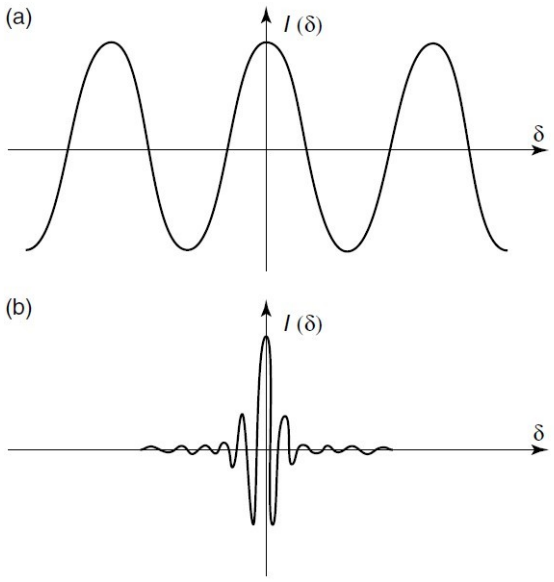

Figure 6.3: Interferograms $I(\delta)$ (Eqs. (6.2) and (6.3)) obtained for (a) radiation from monochromatic source and (b) polychromatic source. Taken from [70].

A moving mirror is situated in one arm of the interferometer. By movement of this mirror, it is possible to change the optical path difference (OPD) δ of interfering beams. When OPD is equal to an integer multiple of wavelength ($\delta = n\lambda$, where n is integer) the beams interfere constructively and the detected intensity is at its maximum. For $\delta = (n+\frac{1}{2})\lambda$ the beams interfere destructively and the detected intensity is minimal. The intensity of the monochromatic light of wavelength λ at the exit of the interferometer can be described as [72]

$$I(\lambda, \delta) = \frac{1}{2} I_0(\lambda) + \frac{1}{2} I_0(\lambda) \cos\left(\frac{2\pi\delta}{\lambda}\right), \tag{6.1}$$

where I_0 is the irradiance of the light source coming into the interferometer. This equation consist of two terms, the first one is independent of OPD and thus is always present, the other one is modulated by harmonic function with OPD as its argument. The latter term is called *interferogram*, $I(\delta)$

$$I(\delta) = \frac{1}{2} I_0(\lambda) \cos\left(\frac{2\pi\delta}{\lambda}\right). \tag{6.2}$$

When polychromatic light source is employed the interferogram has following form

$$I(\delta) = \int_{-\infty}^{+\infty} I_0(\lambda) \cos\left(\frac{2\pi\delta}{\lambda}\right) \mathrm{d}\lambda. \tag{6.3}$$

During the measurements, the mirror in the interferometer moves and the detector records the intensity of the light as a function of δ. For the detection of infrared radiation, photoelectric MCT (Mercury-Cadmium-Telluride, HgCdTe) detectors cooled down by liquid nitrogen (LN_2) are usually employed. When computer links the detected intensity with the corresponding position of the moving mirror, i.e. with the corresponding OPD, the signal in a form of the interferogram $I(\delta)$ is retrieved.

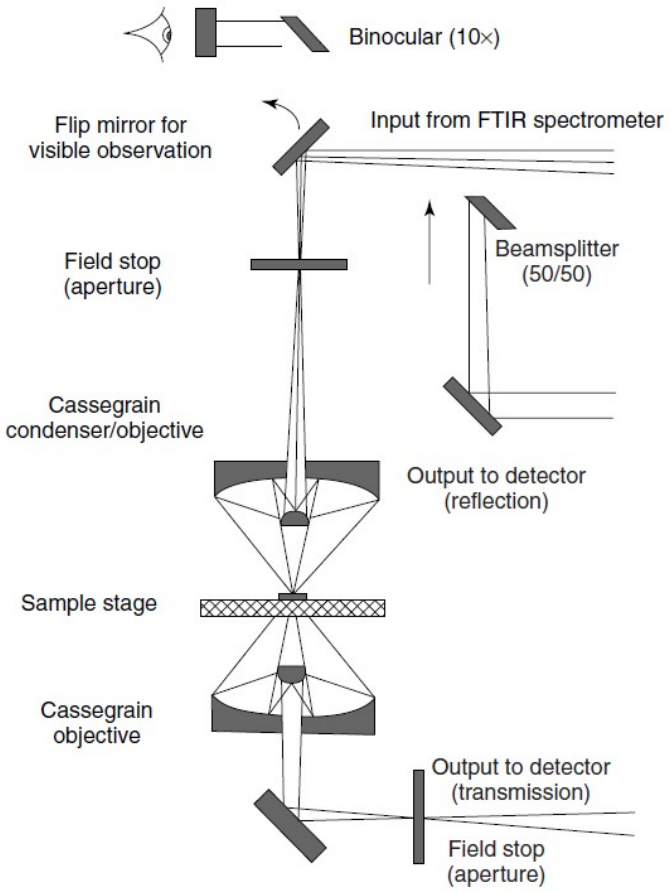

Figure 6.4: Schematic of the microscope part of a typical FTIR microspectrometer. Taken from [70].

To obtain the spectral dependence of the light intensity (spectral irradiance) following Fourier transform is applied to the interferogram [72]

$$I(\lambda) = \int_{-\infty}^{+\infty} I(\delta) \exp\left(\frac{-\mathrm{i}2\pi\delta}{\lambda}\right) \mathrm{d}\delta. \tag{6.4}$$

In the experimental measurements the sample is inserted into the optical path, so the detected signal $I(\delta)$ is modulated by the spectral response function[2] of the sample $R(\lambda)$

$$I(\delta) = \int_{-\infty}^{+\infty} I_0(\lambda) R(\lambda) \cos\left(\frac{2\pi\delta}{\lambda}\right) \mathrm{d}\lambda. \tag{6.5}$$

Our interest in the resonant properties of infrared plasmonic antennas means that we look for the spectral response function $R_\mathrm{a}(\lambda)$ of these antennas. As the antennas are located in very small areas, the FTIR spectrometer has to be connected with an infrared microscope (the schematic is shown in Figure 6.4) which focuses light into these small areas. First, the

[2]When the measurement is taken in reflection configuration the response function of the sample corresponds to the reflectance, when the transmission configuration is employed the response function corresponds to the transmittance.

reference measurement is taken for a part of the sample without antennas. The detected signal is

$$I_{\mathrm{s}}(\delta) = \int_{-\infty}^{+\infty} I_0(\lambda) R_{\mathrm{s}}(\lambda) \cos\left(\frac{2\pi\delta}{\lambda}\right) \mathrm{d}\lambda, \tag{6.6}$$

where $R_{\mathrm{s}}(\lambda)$ is the spectral response function of the substrate. Then the measurements are taken at a part with the antennas. In this case, the detected signal $I(\delta)$ is modulated by response functions of the substrate $R_{\mathrm{s}}(\lambda)$ and antennas $R_{\mathrm{a}}(\lambda)$

$$I_{\mathrm{s,a}}(\delta) = \int_{-\infty}^{+\infty} I_0(\lambda) R_{\mathrm{s}}(\lambda) R_{\mathrm{a}}(\lambda) \cos\left(\frac{2\pi\delta}{\lambda}\right) \mathrm{d}\lambda. \tag{6.7}$$

The spectral response function of the antennas $R_{\mathrm{a}}(\lambda)$ is then obtained by dividing the Fourier transforms of $I_{\mathrm{s,a}}$ and I_{s}.

From the foregoing text, the main advantage of this technique should be obvious. One can get an optical response at a wide range of frequencies simultaneously. The frequencies can range from the ultraviolet to far infrared even using the same instrument, changing only the beam splitter in the interferometer and the detector. No traditional dispersive technique is capable of such wide frequency range [71].

To measure the infrared resonant properties of the arrays of plasmonic antennas we use FTIR spectrometer Bruker Vertex 80v with Globar infrared radiation source and a beam-splitter made of germanium on potassium bromide. The spectrometer was connected to Hyperion 3000 infrared microscope equipped of 36× Cassegrain objective and condenser and MCT and focal-plane array (FPA) detector.

6.3 Substrate materials

6.3.1 Silicon

Commercially available (manufactured by ON Semiconductor) silicon (Si) substrates are widely used at Institute of Physical Engineering (IPE). As a substrate for the EBL, we usually choose low doped Si(100) with a resistivity between 6 and 9 $\Omega \cdot$cm. An advantage of using this substrate in EBL process is its relatively good conductivity, so no charging effects are observed. Also the adhesion of a PMMA resist to the Si substrate is good and there is usually no special need for using MCC Primer 80/20 to enhance the PMMA adhesion.

On the other hand, the doping of Si substrate causes increased absorption of IR light in the otherwise IR-transparent Si substrate. This makes IR transmission measurements impractical or almost impossible. By calculation of Fresnel coefficients for reflectance R and transmittance T in the mid-IR region for the normal angle of incidence, based on data from [73], the reflectance R of pure Si interface is 0.30 and transmittance T is 0.70. For the transmission through substrate (2 interfaces) that means the relative transmitted intensity $I_{\mathrm{T}} = 0.54$ and the relative reflected intensity $I_{\mathrm{R}} = 0.46$(native oxide layer is neglected). These values correspond well with the material sheet from a commercial optical supplier [74]. However, our experimental FTIR measurements showed that for Si

substrates we used, the relative transmitted intensity value is $I_T = 0.10$ and the relative reflected intensity $I_R = 0.35$, so more than half of the incident power is absorbed by the dopants or scattered by them outside the area of detector.

Another disadvantage of this substrate is also connected with its high refractive index $n = 3.42$ in mid-IR region. As LSPR wavelength of antennas is approximated by Equation 4.1, the antenna size has to be smaller than for other used substrates. Smaller antenna sizes means higher requirements on the precision of fabrication, as shifts from nominal sizes cause bigger shifts in LSPR wavelengths due to the high refraction index of Si.

6.3.2 Nanocrystalline diamond film

Nanocrystalline diamond (NCD) is composed of diamond dust crystallites [75]. One of the widely used techniques for fabrication of NCD films is plasma-enhanced chemical vapour deposition (PE-CVD) from $CH_4/H_2/Ar$ plasma. The minimal thickness of deposited NCD film is governed by the size of NCD grains. It is also possible to prepare thin diamond films with a grain size below 10 nm (such diamond is usually called as ultra-nanocrystalline – UNCD), but optical properties (i.e. the dielectric function or the complex refractive index) of such films are more similar to metals [76], i.e. UNCD layers show high absorption.

The optical properties of NCD films [20] deposited by PE-CVD are very similar to the properties of commercially available polycrystalline diamond substrates [77] or to the properties stated in literature [78]. NCD is transparent in wide range of wavelengths and has almost no absorption in VIS and NIR spectral region. NCD films also have low surface roughness and mechanical properties similar to a monocrystalline diamond [79]. NCD is also chemically inert and highly biocompatible. Also a beneficial effect on cell growth and organic tissues were observed, when the presence of NCD blocked some otherwise toxic reactions [75].

Due to its suitability as a substrate for plasmonic antennas, quite good optical properties and biocompatibility, NCD represents a suitable material for a biosensor based on plasmonic antennas. With index of refraction $n \doteq 2.3$, NCD films represent a compromise between silicon and calcium fluorite substrate. For LSPR at a specific wavelength the fabricated structures have to be larger than on silicon, so the fabrication precision is a slightly less important task than for Si substrates.

NCD films for the purposes of IPE were prepared at Institute of Physics, Academy of Sciences of the Czech Republic by PE-CVD, usually using silicon as a substrate; rarely fused silica was used. During imaging of NCD films in SEM, some minor charging effects were observed. Nevertheless, results of EBL showed that this charging has a negligible effect on a lithographic mask and the quality of fabricated structures, so for EBL the coating of PMMA by a conductive film was not necessary. On the other hand, conductive coating by the polymer Espacer 300z was used for the observation of fabricated structures in a SEM, where the exposition to the electron beam was much longer.

6.3.3 Calcium fluoride

Superior optical properties, specifically a low refraction index and more than 90% transparency in the region from 0.2 to 9.0 μm with no absorption, makes calcium fluoride (CaF_2) an ideal substrate for plasmonic antennas from VIS to mid-IR. The refraction index n varies from 1.33 to 1.42 in MIR [80], [81]; this enables to fabricate relatively large structures with not so important fabrication precision.

On the other hand, CaF_2 substrates are very brittle and approximately a one third of them was mechanically damaged or broken during our antennas fabrication process. Even with MCC Primer 80/20 film, the resist adhesion is the worst of all used substrates; PMMA film thickness was often variable for the same spincoating conditions. This made difficult to estimate the optimal electron doses for the EBL; EBL masks were often overexposed and sometimes good structures were fabricated for doses even as low as 140 $\mu C/cm^2$. CaF_2 is nonconductive, so the Espacer 300z film had to be used during EBL and SEM observation to prevent the substrate charging.

7 Influence of NCD film on resonant properties of antennas

As has been stated in Section 4.3, LSPR wavelength depends on the optical properties of the surrounding medium. This makes plasmonic structures (like antennas) suitable for sensing applications. In Section 6.3.2 which is devoted to nanocrystalline diamond (NCD), the high biocompatibility of this material was mentioned. By combining the NCD film as a substrate and a plasmonic antenna as a sensor, we can obtain a biosensor exploiting LSPR. However, it is necessary to investigate the influence of NCD film on resonant properties (resonant wavelength, scattering cross section, local field enhancement) of plasmonic antennas first. Therefore this chapter deals with this investigation.

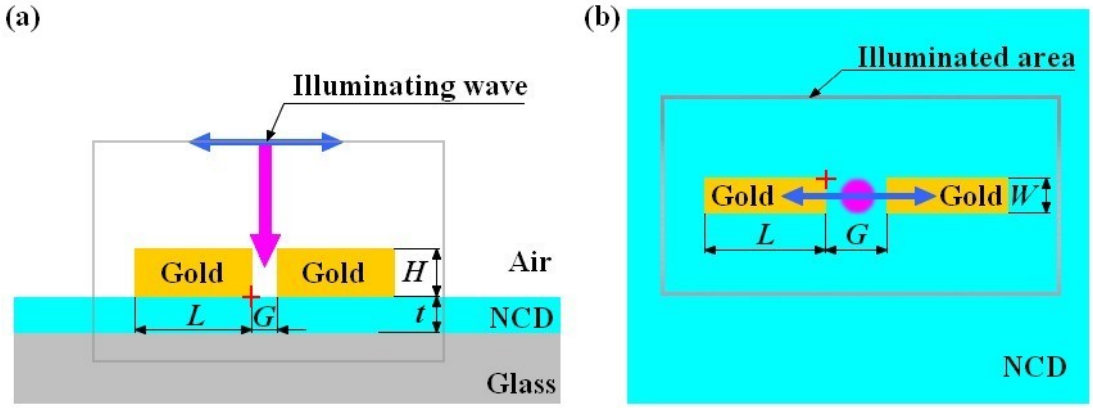

Figure 7.1: (a) Schematic side-view and (b) top-view of a simulated (Lumerical FDTD Solutions) dimer antenna situated on a NCD film of thickness t. Gold antenna rods of length L, width W and height H are separated by the gap G. The purple arrow shows the direction of propagation of the illuminating light wave and the blue arrows show the light polarization. The red cross marks the place, where the maximum value of the local field enhancement is recorded.

Author of this thesis performed series of numerical calculations in Lumerical FDTD package [64] to evaluate resonant properties of gold dimer and single antennas situated on a glass substrate coated with a NCD film and compared to the results with the case without NCD. In addition, the antennas were optionally surrounded by NCD segments, the shapes, dimensions and positions of which is described below in proper sections. A scheme of the simulation geometry for a dimer antenna is shown in Figure 7.1.

7.1 Dielectric function of simulated materials

In Figure 7.1, one can see that our system consists of three various materials – gold, glass (SiO_2) and NCD. The optical properties, (i.e. the dielectric function) of first two are included in Lumerical internal material database. This database is based on handbooks of optical constants like [82] and [83].

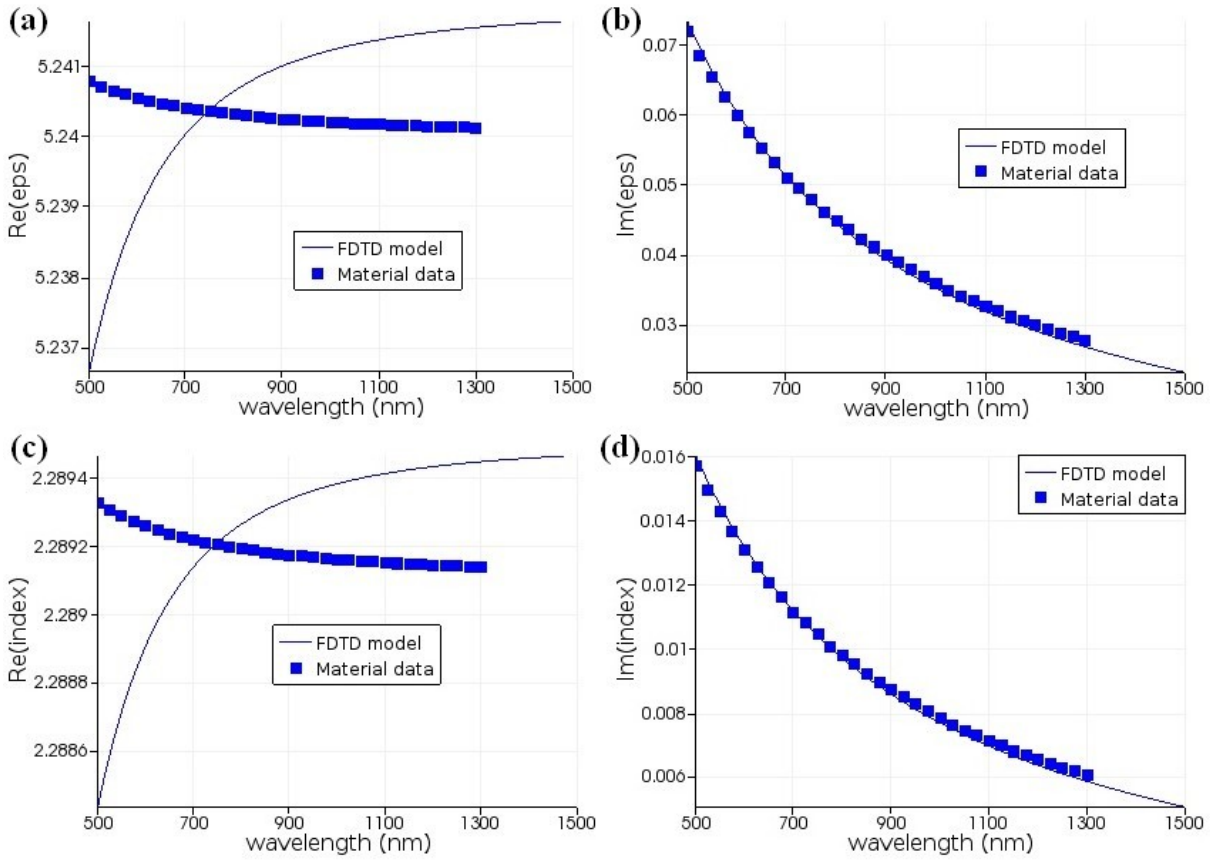

Figure 7.2: Optical properties of nanocrystalline diamond (exported from the Lumerical material explorer) used in the simulation, (a) the real part and (b) the imaginary part of the NCD dielectric function, (c) the real part and (d) the imaginary part of the NCD refractive index. A *Material data* set corresponds to the average of the Sellmeier-equation-fitted experimental data from [20], a blue curve *FDTD model* corresponds to a Lumerical fit of the *Material data* which was then used in the simulations. Note the small range of panels (a) and (c).

Dielectric function of NCD is not the part of Lumerical material database. Also in Handbook of Optical Constants [82], there are only data for refraction index of bulk monocrystalline cubic carbon. To determine the dielectric function of NCD we used the data from [20], where optical properties of several NCD thin films, which varied in fabrication conditions, were experimentally investigated using ellipsometry and reflectometry. The experimental data were later fitted using the Sellmeier equation (2.82). The data and therefore also Sellmeier coefficients in [20] mildly differed for each thin film, mainly in the value of absorption constant C (see Eq. (2.82)).

As the dielectric function of NCD differs for different fabrication conditions, we decided to estimate an *average* dielectric function of NCD. So first, we had calculated the dielectric functions for every NCD thin film mentioned in [20] using the Sellmeier equation (2.82), then we constructed an arithmetic mean (average) dielectric function. The resulting average dielectric function of NCD was then imported to Lumerical material database. Imported data were fitted by a curve which satisfied Kramers-Kronig relations. The optical properties (dielectric function and refraction index) of NCD film used in simulations is shown in Figure 7.2.

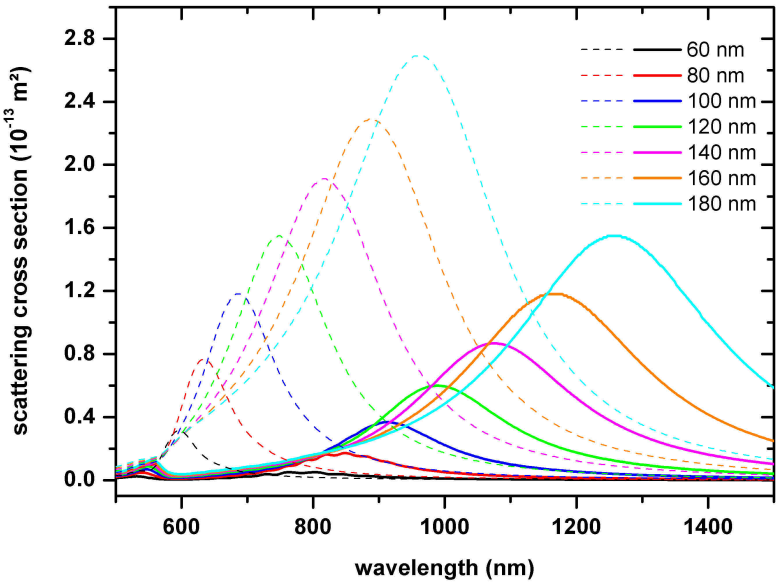

Figure 7.3: Spectral distribution of the scattering cross section of gold dimmer antennas of different lengths situated on a bare glass substrate (dashed curves) and on a glass substrate covered by a 60 nm-thick film of NCD (solid curves) obtained from FDTD simulations. Widths and heights of the antennas were fixed at 60 nm and the size of the gap between the dimer rods was set to 40 nm .

7.2 Influence of antenna dimensions

Series of simulations were run for different dimensions of antennas. The length L of a single antenna (or a single antenna rod in case of dimer) was varied from 60 to 200 nm, width W and height H were varied from 20 to 100 nm. To investigate the influence of antenna dimensions on its resonant properties for all simulations in the series, the thickness of NCD film (when present) was fixed at 60 nm and the gap between the rods of dimer antenna was fixed at 40 nm. When length varied, the width and height of the antenna was fixed at 60 nm. When width or height varied, the length was fixed at 130 nm and the remaining dimension was set to 60 nm. The antennas were illuminated from the top under the normal incidence by white light continuous wave[1] in spectral range from 500 to 1600 nm using Lumerical TFSF light source[2].

The investigated features were the localized surface plasmonic resonant (LSPR) wavelength[3], scattering cross section and local near-field enhancement upon the antenna resonance in the close vicinity of the antenna. The spectral response of the antenna (LSPR wavelength and scattering cross section) to the incoming light was recorded by a set of six plane monitors placed all around the antenna outside the area illuminated by TFSF light source. The local near-field enhancement was recorded by monitors placed in the close vicinity of antenna walls and the antenna-NCD interface. As a measure of the electric

[1]See Section 5.2.1 on normalization of light pulse to continuous wave.
[2]See Section 5.2.2 on total-field scattered-field light source in Lumerical.
[3]The wavelength, where scattering cross section reaches its maximum.

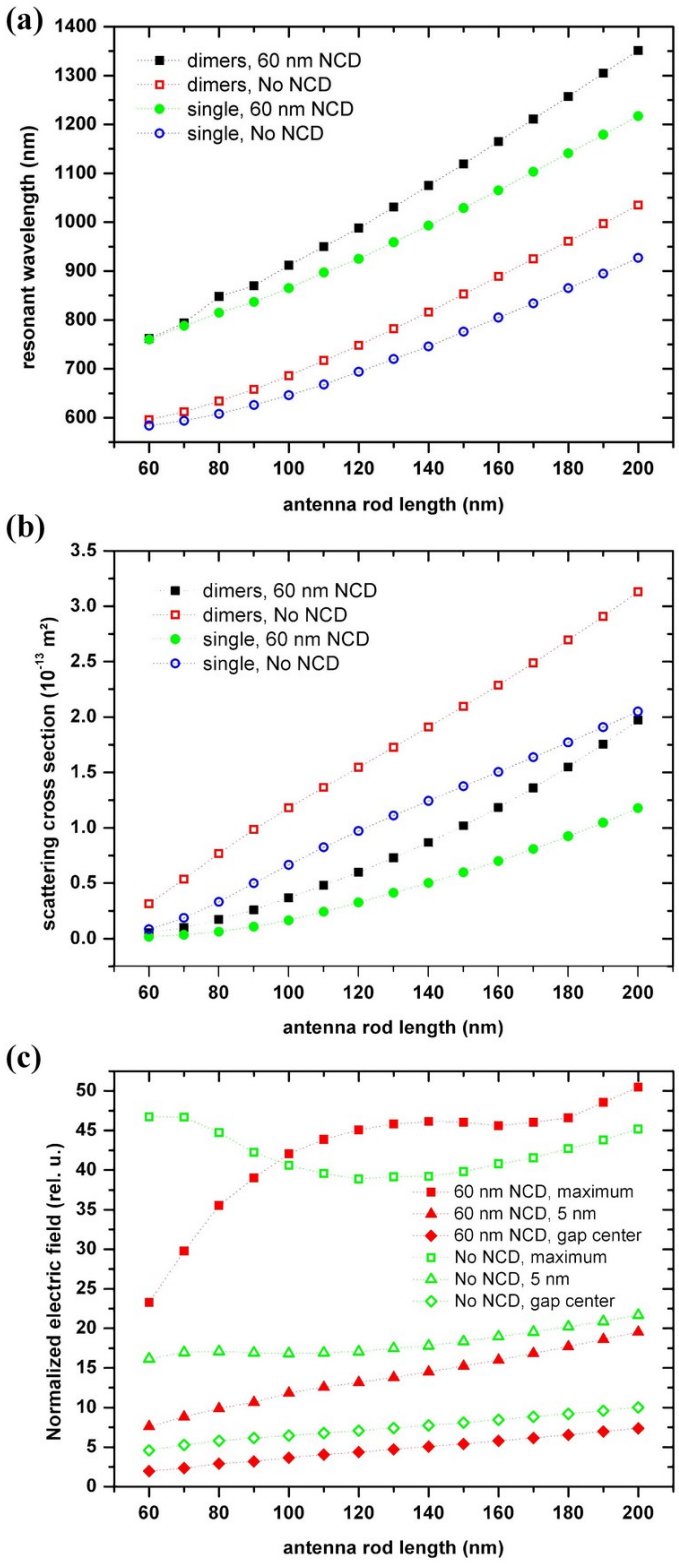

Figure 7.4: (a) Calculated wavelength of LSPR, (b) resonant scattering cross section, (c) resonant local field enhancement for several lengths of gold plasmonic antennas situated on a bare glass substrate and on a glass substrate covered by a 60 nm-thick film of NCD. Antennas widths and heights were fixed at 60 nm and the gap between the dimer rods was 40 nm. The field enhancement was recorded at the vertices of the dimer antenna rods, 5 nm from the vertex towards the centre of the gap and in the gap centre.

field enhancement upon antenna resonance we used the maximum of local electric field in the vicinity of the antenna normalized to the incident field.

The size of mesh cells in simulations was set automatically by the software and was in the range of a few nanometres. In the vicinity of the antenna as well as at the antenna-NCD or antenna-glass interface, the size of the mesh was manually set to 1.0 nm. Every simulation was limited to one single or dimer[4] antenna only and the simulation area was surrounded by Perfectly Matched Layer (PML) absorbing boundary conditions[5].

In Figure 7.3, the spectra of several gold plasmonic dimer antennas on a bare glass substrate and on a glass substrate covered by 60 nm-thick NCD film are shown. Results of the simulations with various lengths of antennas are summarized in Figure 7.4. As can be seen from Figure 7.4a, where the resonant wavelengths of gold plasmonic dimer and single antennas is shown as a function of antenna length, the resonant wavelength of antennas is linearly scaled with its length. This is not surprising, as all the theoretical approaches for the determination of the localized surface plasmon resonance wavelength which have been presented in Chapter 4 (Eqs. (4.1), (4.22)[6] and (4.23)) expect this linear scaling with the antenna length.

Also the differences between the LSPR wavelength of antennas situated on glass and NCD film can be easily explained by the aforementioned models. Antennas are sensitive to the refractive index of their surroundings, which means that in the presence of the material of higher index, the resonant wavelength shifts to higher wavelengths. Therefore, the resonant wavelength of antennas on NCD film is red-shifted with respect to the antennas on bare glass.

The last feature noticeable in Fig. 7.4a is a difference of LSPR wavelength between the single and dimer antennas of same length and substrate. It is known from the literature (e.g. [84]) that when antennas are placed close to each other their plasmon modes hybridize and their resonant wavelength shifts. The dimer antenna consist of two rods and under the illumination the identical electric dipole emerges in both of them. When the distance between the rods is small enough, the dipoles interact with each other which leads to the shift of the dimer antenna resonant wavelength. Depending on the polarization of excited mode, the resonant wavelength is either red-shifted for longitudinal modes of blue-shifted for transversal modes [15, p. 82]. As the modes excited in the dimer antennas are longitudinal with respect to the orientation of antenna rods, the resonant wavelength is red-shifted.

The scattering cross section of the antenna also scales linearly with its length, as can be seen from Figure 7.4b. Naturally, dimer antennas scatter more light than single ones, because there are two antenna rods in dimer antenna instead of one. In comparison to single antenna, the geometrical cross section of the dimer antenna is double. But with the exception of the smallest antennas, the scattering cross section of dimer antennas is lower than double value of the scattering cross section of single counterparts.

[4] One dimer antenna consists of two antenna rods.

[5] PML absorbing boundary conditions are impedance matched to the simulation region and its materials, so they absorb propagating and evanescent light waves leaving the simulation area with almost no reflections. An ideal PML boundary should produce no reflections, however, in practice, there will always be some reflections due to the mesh discretization, like in the case of TFSF boundary (Section 5.2.2).

[6] Antenna geometry is *hidden* in the coefficients a_1 and a_2.

The scattering cross section of antennas situated on NCD film is significantly lower then the cross section of the antennas of the same length on glass substrate. The relation for scattering cross section of a sphere (Eq. 4.19) can now serve us for the explanation of this feature[7]. According to this equation, the value of the antenna scattering cross section is governed by the second power of its polarizability α and the fourth power of wavelength λ, which in equation (4.19) is hidden in the wavenumber k. As was discussed in foregoing text, the presence of NCD film below the antennas shifts their resonant wavelength to higher values. It can be seen from Figure 7.4a that the resonant wavelength of antennas on NCD is approximately 30 % bigger than for corresponding counterpart on bare glass substrate ($\lambda_{\mathrm{r,NCD}}/\lambda_{\mathrm{r,glass}} \approx 1.3$). The fourth power of this ratio yields $1.3^4 \doteq 2.86$. Therefore, due to the shift of the resonant wavelength, the scattering cross section of antennas on NCD film should be 2.86 times smaller than the cross section of their counterparts on bare glass substrate. The recorded data shows that this ratio of scattering cross sections varies between 1.66 for the largest antennas and 5.42 for the smallest ones. The deviation from calculated ratio 2.86 is caused by a different geometry and also by the change of the antenna polarizability α. The influence of the polarizability change will be discusses in the following text on local electric field enhancement.

The maximum value of local field enhancement was recorded at the antenna vertex on the interface between air, antenna and substrate (in Figure 7.1 marked by red cross). The field enhancement was also recorded at the point situated 5 nm from the antenna vertex in the direction towards the gap centre and in the centre of the gap. The differences in the values of field enhancement between the antennas on NCD and glass counterparts can be seen from Figure 7.4c. To explain the differences, we will use the relation for the expression of electric near-field around the spherical particle (Eq. 4.15) together with the relation for dipole moment (Eq. 4.7). When we substitute (4.7) into (4.15) and when we neglect the imaginary part of dielectric functions[8], then we get

$$\vec{E} = \frac{\varepsilon - \varepsilon_{\mathrm{m}}}{\varepsilon + 2\varepsilon_{\mathrm{m}}} a^3 [3\vec{n}(\vec{n} \cdot \vec{E}_0) - \vec{E}_0] \frac{1}{r^3}. \tag{7.1}$$

It can be seen from this equation, that the electric near-field is given by the value of fraction $(\varepsilon - \varepsilon_{\mathrm{m}})/(\varepsilon + 2\varepsilon_{\mathrm{m}})$. In the spectral region under consideration, ε_{m} is almost constant ($\varepsilon_{\mathrm{m,glass}} \approx 2.14$, $\varepsilon_{\mathrm{m,NCD}} \approx 5.24$), but the dielectric function of gold varies significantly with wavelength. Therefore, the main reason for differences of field enhancement is the variability of gold dielectric function with wavelength. The difference in substrate dielectric function (when glass is replaced by NCD) causes the slight change of the wavelength, for which the Fröhlich condition (Eq. 4.10) is satisfied.

It can be seen from Figure 7.4c that for antennas on NCD film which are shorter than 100 nm, the maximum of the field enhancement is smaller compared with the corresponding counterparts on glass substrate. For longer antennas the maximum of the field enhancement is slightly bigger than for the antennas on glass. Nevertheless, when field enhancement is recorded further away from the antenna vertex, the values for antennas

[7] We expect that this feature is qualitatively shape independent, i.e. the results we would get for spherical particles of similar dimension might differ in the absolute values, but the observed trend in the data would be similar.

[8] After the substitution we get $\vec{n} \cdot \vec{p} = \vec{n} \cdot \hat{C}\vec{E}_0$, where complex $\hat{C}$ can complicate the scalar product and also the approximation. By neglecting of imaginary parts of dielectric functions, $\hat{C}$ becomes real.

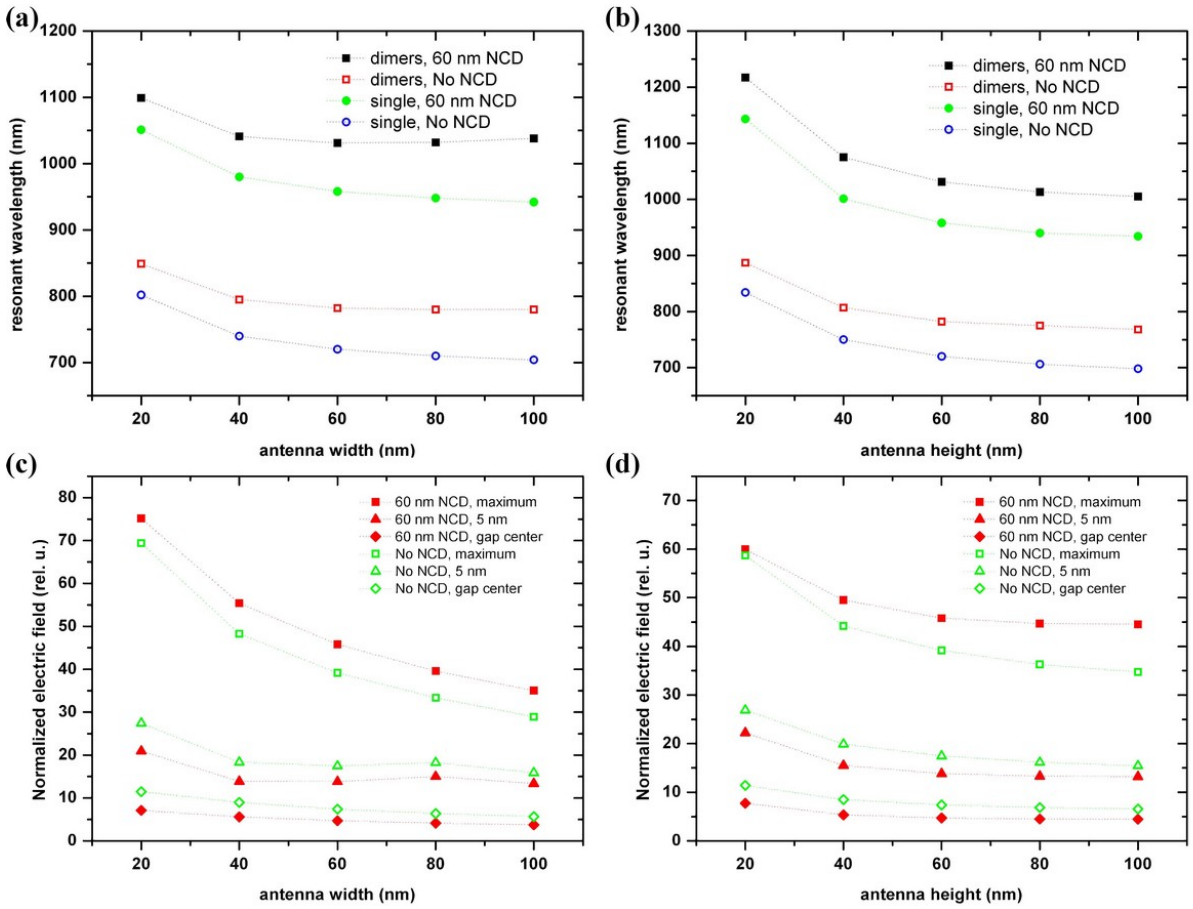

Figure 7.5: Influence of antenna width and height on resonant properties of gold plasmonic antenna (length 130 nm, gap between the antenna rods 40 nm) situated on a bare glass substrate and a glass substrate coated with 60 nm of NCD. (a) Wavelength of LSPR and (c) local resonant field enhancement for antennas of fixed height 60 nm. (b) Wavelength of LSPR and (d) local resonant field enhancement for antennas of fixed width 60 nm. The field enhancement was recorded at the vertices of the antenna rods, 5 nm from the vertex towards the centre of the gap and in the gap centre.

on NCD are always smaller then for antennas on glass. This means that the field is more confined to the antenna-air-NCD interface than to antenna-air-glass.

In the foregoing text, we have discussed the influence of the antennas length on their resonant properties and tried to explain the observed features. Now, it is time to mention the influence of other two dimensions – width and height. The results of simulations are summarized in Figure 7.5. As it can be seen from this figure, the change of antenna width and height results in similar effects. When the antenna becomes narrower or lower, its resonant wavelength shifts to higher values and the field in the antenna vicinity is further enhanced.

To explain the shift of the resonant wavelength, we look back at the analytical model of Kalousek [54] for rod-like antennas we mentioned in Section 4.3.2. The resonant wavelength of rod-like antenna is expressed by equation (4.23). According to this equation, the resonant wavelength is proportional to the ratio between antenna length and radius L/R. Therefore, the resonant wavelength increases (red-shifts) with the decreasing radius. In

case of slab-like antennas we supposed in the simulations, we can approximate the radius R of rod-like antenna with half of height or width of slab-like antenna. Therefore, the recorded shifts of the antenna resonant wavelength with their width and height correspond to Kalousek's model[9,10].

The bigger field enhancement is caused by the decreasing distances between the places of high field enhancement. We known that the highest field enhancement is at the vertices of the antennas and with increasing distance from the vertices the field enhancement significantly drops. However, as it can be seen in Figure 7.4c, even when the distance from vertices is several tens on nm (corresponding to the gap centre), the field enhancement is still noticeable. With decreasing width and height of the antennas, the adjacent vertices gets closer to each other and the field in the vicinity of the vertices is therefore *boosted*. The scattering cross section of antennas remains constant with the change of antenna width and height and therefore it is not plotted into the graph.

7.3 Influence of NCD film thickness

To determine the influence of the NCD film thickness on resonant properties of plasmonic antennas, another series of simulations was designed. In this series the length of antenna was fixed at 130 nm, width and height at 60 nm and gap between antenna rods of dimer was 40 nm. The thickness of the NCD film between the antenna and glass substrate varied from 10 to 190 nm. The results of the simulations are summarized in Figure 7.6. Again, the resonant wavelengths of dimer antennas in Figure 7.6a are red-shifted with respect to their single counterparts. It can be seen from this figure that the presence of an NCD film as thin as 10 nm on a glass substrate causes huge red-shift (approximately 150 nm) of the antenna resonant wavelength. With further growth of NCD film, the resonant wavelength is further red-shifted, but the rate of the red-shift gradually decreases with film thickness. When the thickness of the NCD film changes by 10 nm from 10 nm to 20 nm, the resonant wavelength is red-shifted by approximately 50 nm. When the thickness of NCD film changes from 60 nm to 70 nm the corresponding red-shift of resonant wavelength is as low as 4 nm.

In Figure 7.6b one can see that the resonant scattering cross section of the antennas varies greatly with the thickness of NCD film and reaches its minimum for range of NCD thicknesses 80–90 nm. The drop in cross section is present for both single antennas and dimers. The values of cross sections in the minimum are only about one third of the maximum values. Similar drop also occurs for the resonant field enhancement (Figure 7.6c). From Figure 7.6a, we can see that for NCD film thicknesses bigger than 60 nm the resonant wavelength varies only slightly. Therefore, dielectric functions of gold and NCD do not significantly change with the NCD film thickness and such drop in scattering cross section (see Eq. (4.19)) cannot be explained neither by the change of antenna polarizability α

[9] It also corresponds to the model of Novotny [53] (Eq. 4.22), but the geometry of the antennas is hidden in the values of coefficients a_1 and a_2 in this model and the shift of the resonant wavelength is not evident at the first glance.

[10] In Equation (4.23), the ratio L/R appears also in $\left[\ln\left(\vartheta\frac{L}{R}\right)\right]^{-1/2}$, where the effect of change of R on the shift of the resonant wavelength is opposite, but smaller.

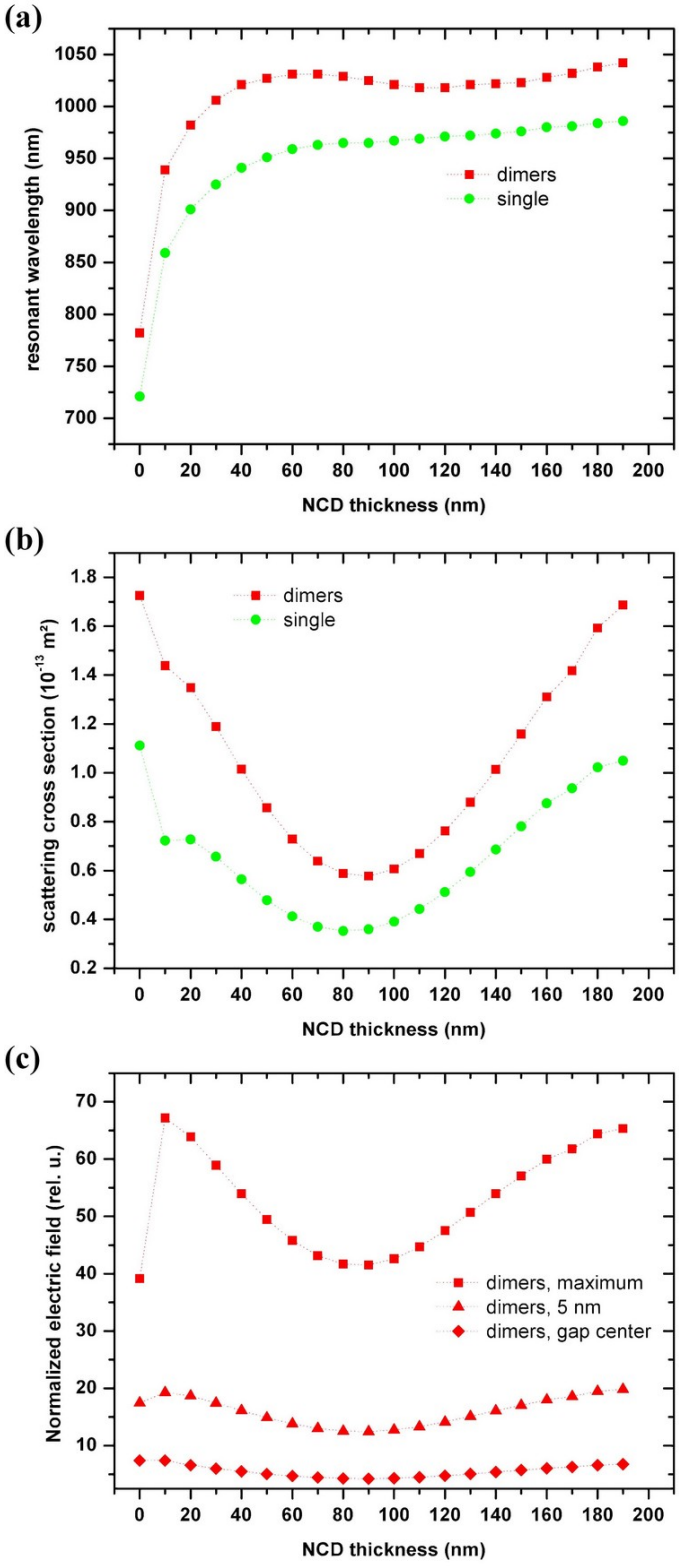

Figure 7.6: (a) Calculated wavelength of LSPR, (b) resonant scattering cross section and (c) resonant local field enhancement of single and dimer gold plasmonic antennas (dimensions 130 × 60 × 60 nm^3, gap between rods of dimer 40 nm) situated on a glass substrate covered by a NCD film of various thickness. The field enhancement was recorded at the vertices of the antenna rods, 5 nm from the vertex towards the centre of the gap and in the gap centre.

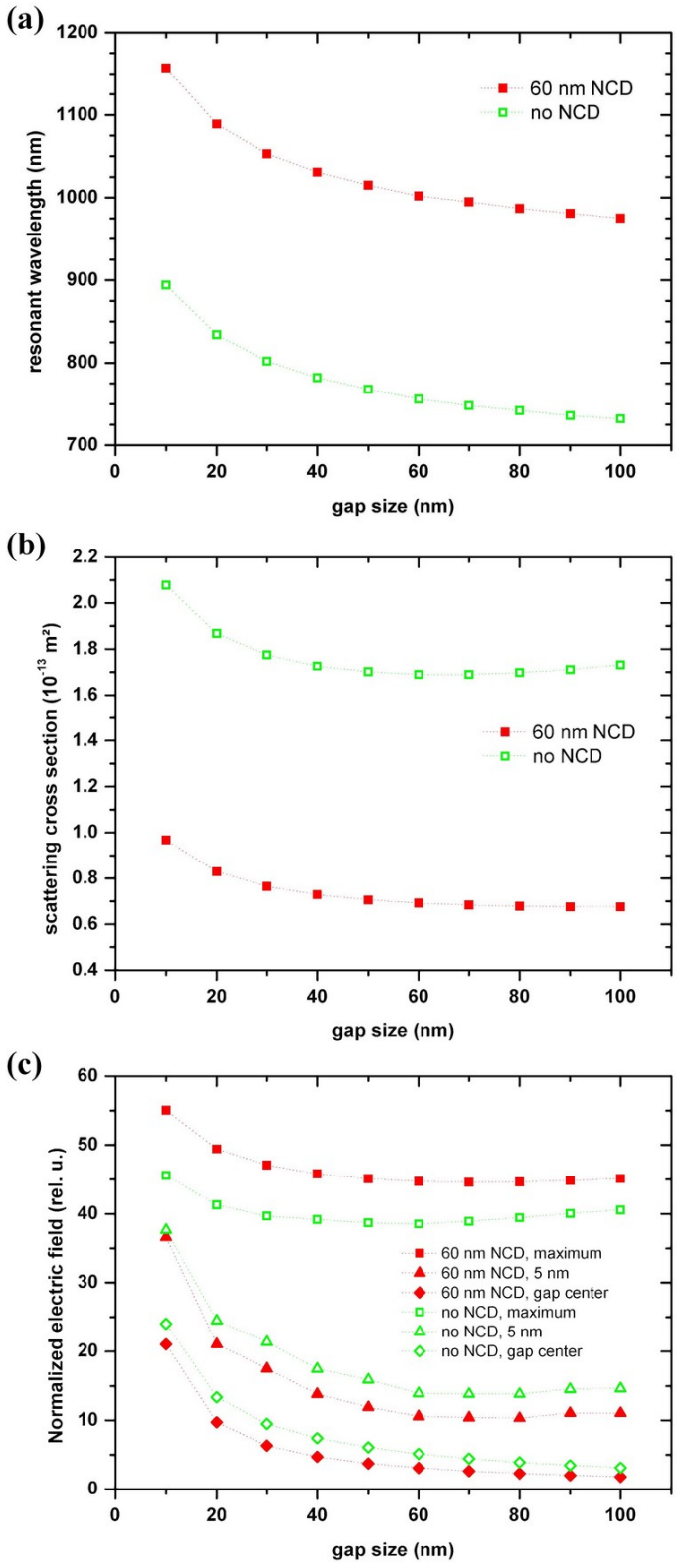

Figure 7.7: (a) Calculated wavelength of LSPR, (b) resonant scattering cross section and (c) resonant local field enhancement of a dimer gold plasmonic antenna (dimensions $130 \times 60 \times 60\,\mathrm{nm}^3$) situated on a bare glass substrate and on a glass substrate covered by the 60 nm-thick NCD film. The gap between the dimer rods varies. The field enhancement was recorded at the vertices of the antenna rods, 5 nm from the vertex towards the centre of the gap and in the gap centre.

nor by the pronounced change of resonant wavenumber $k = 2\pi/\lambda$. Therefore, this feature is the most probably connected with the thickness of the NCD film.

7.4 Influence of gap size in dimer antennas

To investigate the influence of the size of the gap between the antenna rods in dimer antennas, we designed the series of simulations, where dimensions of the antenna rods ($130 \times 60 \times 60\,\mathrm{nm}^3$) as well as the thickness of the NCD film (60 nm, when present) were fixed and the size of the gap was varied from 10 to 100 nm. The results of the simulations are summarized in Figure 7.7. As we can see from this figure, the antenna resonant wavelength is red-shifted as the size of the gap between the rods decreases. The reason for this red-shift is the same as for spectra of dimers (see Section 7.2 for the explanation). Under the illumination, the identical electric dipoles emerge in both antenna rods. When the distance between the antenna rods is small enough, dipoles interact with each other. For longitudinal modes in the antennas, this interaction leads to red-shift of the resonant wavelength. The red-shift of the resonant wavelength increases with stronger dipole interaction, thus with decreasing distance between the antenna rods.

It can be seen from Figure 7.7c that with smaller size of the gap, the enhancement of electric field is even bigger. The enlargement of the field value in the gap centre can be easily explained. With the smaller size of the gap, the gap centre is located closer to the antenna and the field enhancement is therefore bigger. The enlargement of the field at the antenna inner vertices is caused by smaller distances to the vertices of the other antenna rod. Therefore the field at the antenna-air-NCD interface (e.g. at the antenna vertex) is *boosted* by the field of dipole in the other antenna rod. The same explanation applies for the case of point located 5 nm from the antenna vertex in the direction towards the gap centre.

Also the resonant scattering cross section of the dimer antenna is enhanced when the size of the gap becomes smaller, despite that the geometrical antenna cross section does not change and the red-shift of the resonant wavelength should lead to smaller wavenumber k and therefore to decrease of the scattering cross section.

7.5 Influence of mutual position of NCD and antenna

The next series of simulations studied how resonant properties of the antennas vary with the mutual position of the antenna and NCD film or elements. Three different configurations, shown in Figure 7.8a–c, were studied. The dimensions of the antenna were fixed (length 130 nm, width and height 60 nm) and the thickness of the NCD film varied from 10 to 140 nm.

As NCD thin film could be used to accommodate organic species on its surface whose presence would be sensed by plasmonic structures, the near-field enhancement at the air-NCD interface in the close vicinity of the resonant antenna was the subject of our interest. This means that for the setup with the NCD film between the glass substrate and the

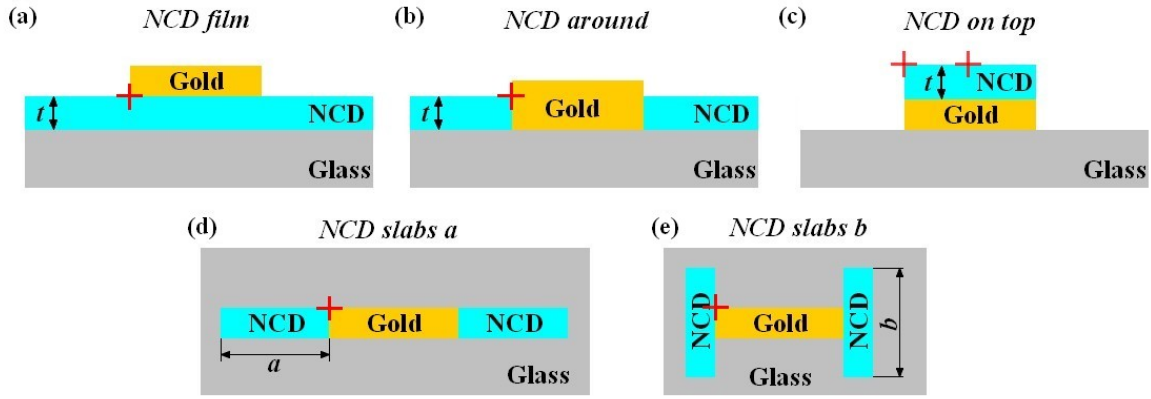

Figure 7.8: (a)–(c) Schematic side-view of simulation designs with a different mutual position of the NCD film of thickness t and the antenna. (d), (e) Schematic top-view of simulation designs of a single antenna with two types of NCD slabs placed at the antenna forehead. The red crosses mark the points where the electric near-field enhancement was recorded.

single gold antenna (Figure 7.8a) the field enhancement was monitored near the base of the antenna. When the NCD film was located around the antenna (Figure 7.8b), the electric field was recorded at the interface between the antenna, NCD film and air. When a segment of NCD was placed only on the top of the antenna (Figure 7.8c), the field enhancement was monitored on the top of the NCD segment, above the antenna vertex (for thinner NCD segments) or above the centre of antenna (for thicker segments).

Figure 7.9 summarizes the results of this series of simulations. The data for NCD film (configuration can be found in Figure 7.8a) are those already presented in Figure 7.6 as *single*.

In Figure 7.9a, the evolution of the antenna resonant wavelength with increasing thickness of NCD is shown. From this figure it is apparent that the antenna sensitivity to the presence of NCD film significantly varies with the mutual position of the antenna and NCD. When no NCD is present, the resonant wavelength of the antenna is 722 nm. The antenna is the least sensitive to the presence of NCD segment on its top. In such case, the red-shift of resonant wavelength, caused by the presence of NCD segment, saturates for the 60nm thickness of the NCD segment at 830 nm. When NCD film is located between the antenna and glass substrate, the sensitivity of the antenna is higher, i.e. the red-shift of the resonant wavelength with the thickness of NCD is bigger than in the previous case; the resonant wavelength reaches its maximum of 960 nm for the NCD thickness of 60 nm. Similarly to the previous case, no further red shift is observed for the NCD film thicknesses above 60 nm. We can assume that the antennas can sense[11] the presence of investigated material (e.g. organic species) at the distances comparable to the saturation of the resonant wavelength red-shift, i.e., 60 nm.

The sensitivity to the presence of NCD film is the strongest for the antenna laying directly on bare glass substrate (Figure 7.8b). The red-shift of the antenna resonant wavelength with increasing thickness of NCD film is biggest of all the investigated configurations.

[11]The sensitivity of antennas will also be affected by the size of the surface area covered with the investigated material.

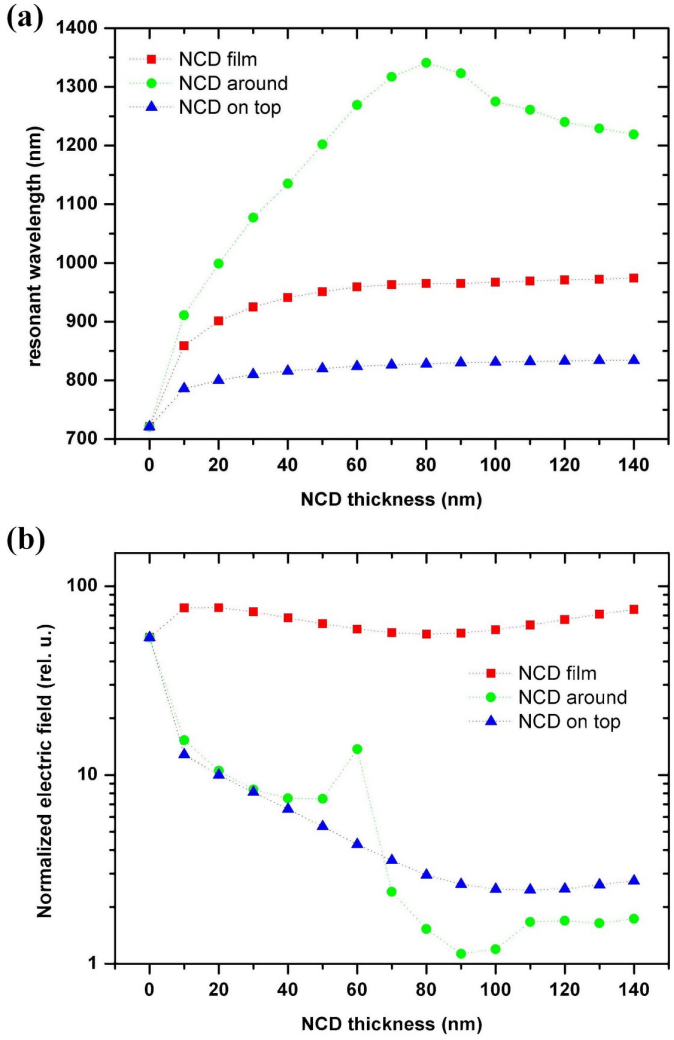

Figure 7.9: (a) Wavelength of LSPR and (b) resonant local field enhancement of single gold plasmonic antenna (dimensions $130 \times 60 \times 60\,\mathrm{nm}^3$) on or in NCD as shown in Figure 7.8a–c.

As the thickness of the film grows up to 80 nm, the corresponding average red-shift of resonant wavelength is approximately 70 nm for every 10 nm of NCD film thickness. For thicker films, the antenna resonant wavelength exhibits slight blueshift with the increasing thickness.

For sensing methods, like surface enhanced Raman spectroscopy (SERS) [33], surface enhanced infrared absorption spectroscopy (SEIRA) [37] and surface enhanced infrared spectroscopy (SEIRS) [38], which are all based on signal amplification by enhanced near-field, the quantification of this field enhancement becomes important. The maximum values of field enhancement in points of our interest (marked by red crosses in Figure 7.8) are shown in Figure 7.9b. When the antenna is placed on the glass substrate and either surrounded by NCD film or covered by NCD segment from the top (Figure 7.8b,c), the point of interest shifts with the thickness of NCD. The highest fields related to the LSPR occur at the upper and lower antenna interfaces and they drop rapidly with increasing distance from the antenna interface. Therefore, the highest values of the field enhancement are found at the absence of NCD or when the thickness of surrounding NCD film is the

same as the thickness of the antenna. The former corresponds to the case, when the monitoring point is at the glass-air interface close to the base of the antenna (configuration in Figure 7.8b) or close to the top of the antenna (configuration in Figure 7.8c). The latter corresponds to the case, when the monitoring point is in the vicinity of upper antenna interface.

Contrary to our previous investigations, we will not discuss the differences in scattering cross section for particular configurations. Due to the way, how this cross section is computed in Lumerical FDTD Solutions, the results obtained for particular configurations (Figure 7.8a–c) are not comparable with each other.

Spatially localized NCD slabs at the antenna foreheads

In the last series of simulations, two different types of NCD slabs were placed at the forehead of the antennas. One type, marked as *NCD slabs a* (Figure 7.8d), had the same width and height as the antenna (60 nm) and its length a varied in the direction parallel both to antenna longitudinal axis and polarization of the incident wave. The length b of the other type of slabs, marked as *NCD slabs b* (Figure 7.8e), varied in the direction perpendicular both to the antenna longitudinal axis and polarization of the incident wave. Width and height of these slabs were fixed at 50 and 60 nm, respectively.

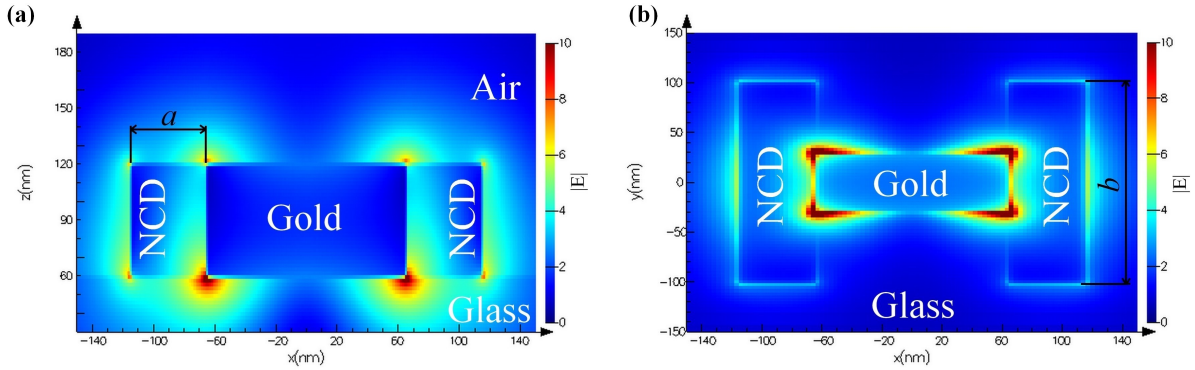

Figure 7.10: (a) Side- and (b) top-view of the calculated local field enhancement in the vicinity of a single gold antenna located on the glass substrate with *NCD slabs b* (Figure 7.8e). The antenna was excited by a plane wave (TFSF source) impinging from top, the magnitude of the electric field is expressed in units of the amplitude of the excitation field.

A visualization of the resonant local near-field enhancement around the antenna with NCD slabs at its foreheads is shown in Figure 7.10. As it can be seen from this figure, the electric field is not only enhanced in the vicinity of antenna interface, but also at the interface between the NCD slabs and air. From this point-of-view, it is possible to declare that the presence of the slabs increases the area around the antenna, where the electric field is enhanced. The enhancement of the electric field around the NCD-air interface results from the necessity of meeting the electric field boundary conditions (Eqs. (2.26) and (2.28)) at the material interface.

The resonant wavelength of these antennas, scattering cross section and maximum field enhancement upon resonances shown as a function of varying dimensions of the slabs (a, b)

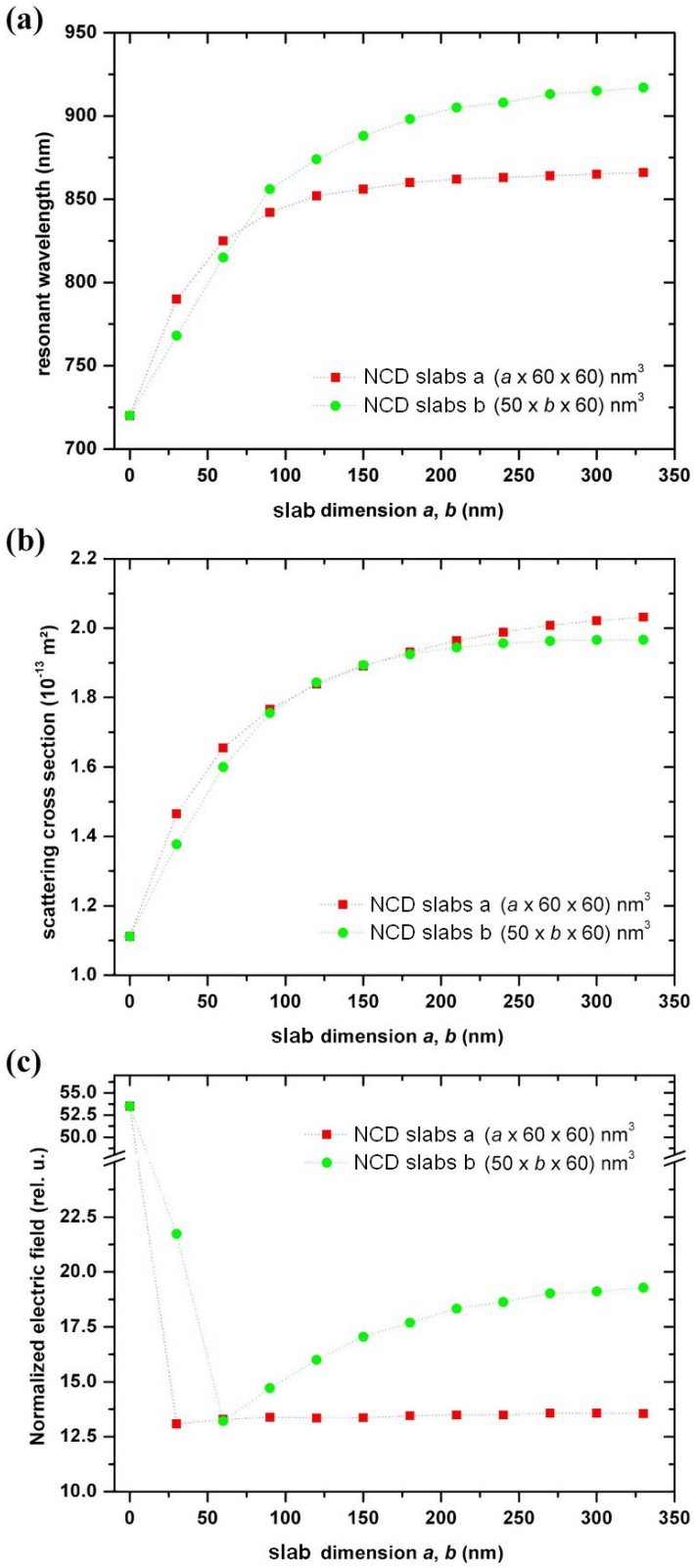

Figure 7.11: (a) Wavelength of LSPR, (b) resonant scattering cross section and (c) resonant local field enhancement of a single gold plasmonic antenna (dimensions 130 × 60 × 60 nm^3) with the NCD slabs at the antenna forehead (for geometry, see Figure 7.8d,e).

can be seen in Figure 7.11. The red shift of the resonance wavelength (Figure 7.11a) with increasing dimensions of the slabs is in accordance with the higher index of refraction of NCD compared to the air and tends to saturate for the larger slab dimensions.

The scattering cross section significantly increases with both the dimensions of NCD slabs. The recorded increase of cross section is mainly attributed to the method of cross section calculation using the illumination of the antenna by TFSF source. NCD slabs near the antenna present another pair of scattering structures inside the space illuminated by TFSF radiation source (i.e. inside the space where total field is calculated). Therefore, rather than the scattering cross section of a single gold antenna, the cross section in Figure 7.11b corresponds to a scattering cross section of a multi-structure system of a single gold and two NCD slabs.

7.6 Experiment

As our fabrication capabilities were limited in both availability and precision, we were not able to fabricated all the antenna configurations presented in the foregoing text. Also the experimental detection of LSPR resonance in the near-infrared (NIR) spectral region was impossible to perform for a long time due to lack of a suitable detector and beamsplitter in FTIR setup. Eventually, we fabricated a small series of single antenna arrays only. These served mainly to compare the resonant wavelength position with the results of simulations.

We had been provided with several substrates of fused silica coated by a film of NCD. The coating was done by plasma enhanced chemical vapour deposition at Institute of Physics, Academy of Sciences of the Czech Republic. The thickness of the coating was 200 and 600 nm. Using spincoating, the substrate with 200 nm NCD film was covered by PMMA (4000 rpm, 30 s) and Espacer 300z (2000 rpm, 30 s). Afterwards, a mask for the antenna arrays ($50\,\mathrm{x}\,50\,\mu\mathrm{m}^2$, antenna length $0.1-1.0\,\mu$m, spacing $0.5\,\mu$m in both directions) was drawn into PMMA by electron beam using Tescan Vega2[12] (30 keV, $275\,\mu\mathrm{C/cm}^2$). The sample was then metallized (IBAD, 3 nm adhesion film of Ti and 60 nm Au). As the dimensions of the fabricated antennas were relatively small, no ultrasonic bath was applied during lift-off process.

The shape and dimensions of fabricated structures were studied using mainly the scanning electron microscopy (SEM). In Figure 7.12, the dark-field optical microscope and scanning electron microscope large-scale images of the array of antennas are shown. The detail of the antenna array acquired by SEM using both the detector of secondary electrons (SE detector) and the in-beam detector of backscattered electrons (inBeam BSE) is shown in Figure 7.13. There is a noticeable difference in contrast of the images taken by SE and inBeam BSE detectors. Emissivity of the secondary electrons from NCD and gold seem to be similar, therefore when the image is taken by SE detector (Figure 7.13a,c), it usually is not easy to distinguish between these two materials. On the other hand, it is known [85] that when BSE detector is used for imaging gold and diamond have a very good material contrast, as the electron backscattering coefficient is proportional to the atomic number

[12]Due to the limited resolution of used lithography device, the dimensions of fabricated antennas are bigger than intended. Nevertheless, the antennas still have LSPR wavelength in NIR region.

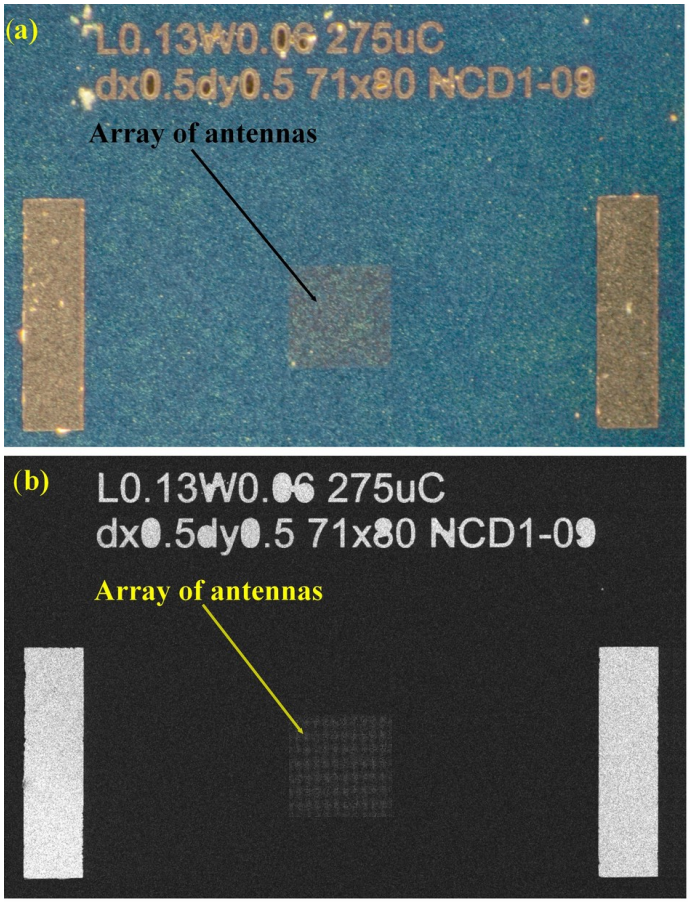

Figure 7.12: Large-scale images of an array of gold plasmonic antennas fabricated on a fused silica substrate with a 200 nm-thick film of NCD. (a) Dark-field microscope image (Olympus MX51, 50× objective) and (b) image from the scanning electron microscope (Tescan Lyra3, in-beam backscattered electron detector). To prevent substrate charging effects, the sample was coated by Espacer 300z conductive polymer. The black lines over the antenna array in the SEM image are caused by imaging artefacts.

of the target material. Thus, the resulting images (Figure 7.13b,d) show the antennas rather clearly, including the defects (missing antennas) in the array. Missing structures were most likely removed during lift-off process. Their number is rather low and we do not expect any significant impact to the resonant properties of the antennas.

An image of 1μm dimer gold antennas on NCD film is shown in Figure 7.14. During the imaging the sample was tilted by 75° with respect to the incident electron beam. Tilt of the sample allows to visualize the surface roughness of the NCD film.

The resonant properties of fabricated structures in near-infrared spectral region were measured using microscopic FTIR in reflection configuration. As the spectral region below 1250 nm is out of the usual detection limit of available FTIR device, following modifications were made:

- VIS/NIR halogen source of unpolarized light was use instead of MIR Globar source.
- LN_2 cooled MCT detector (detection range from 1.25 μm to 16 μm) was replaced by the Peltier cooled InGaAs detector (detection range from 0.8 μm to 2.5 μm).

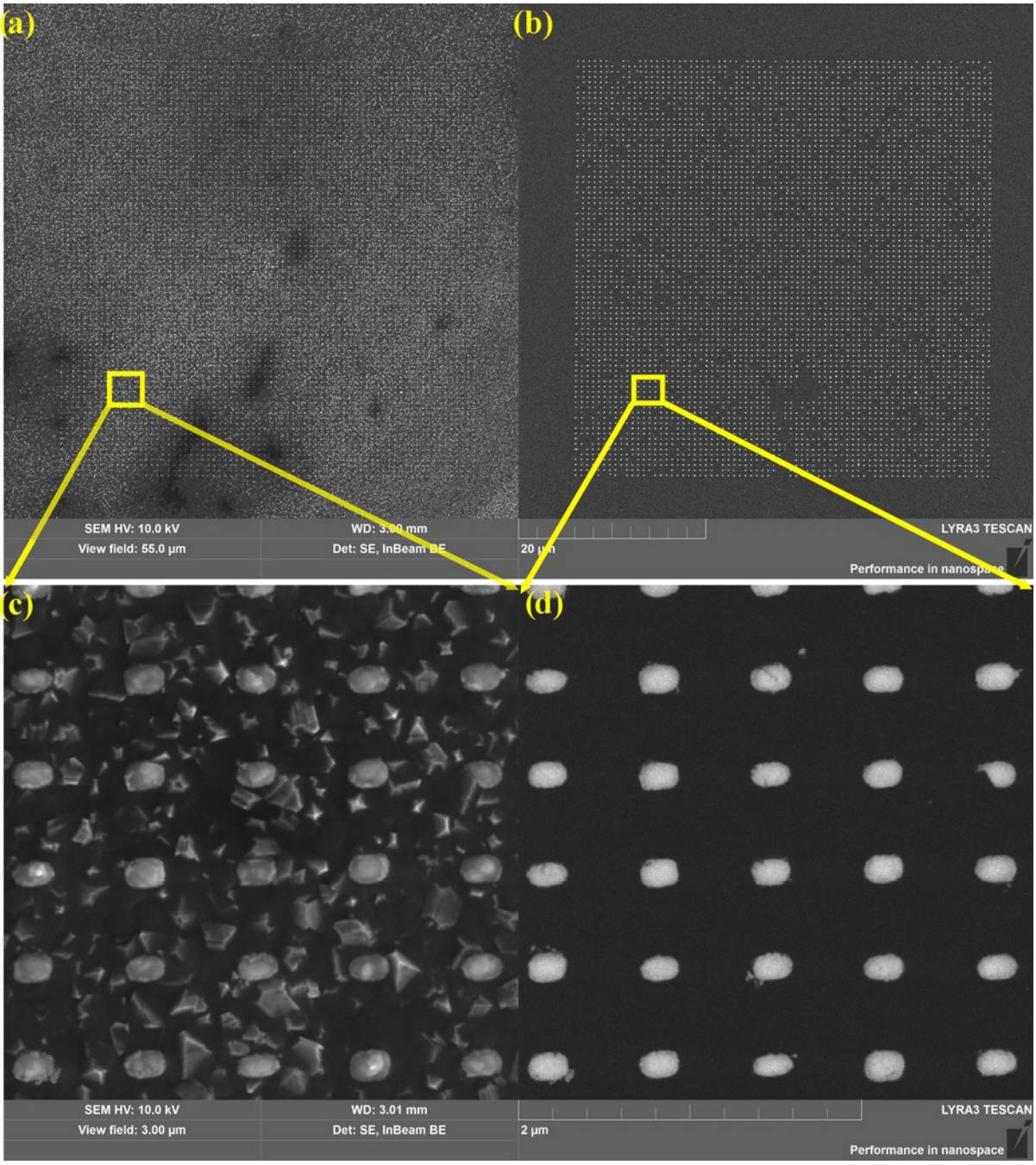

Figure 7.13: Scanning electron microscope image (Tescan Lyra3) of an array of gold plasmonic antennas fabricated on a fused silica substrate with 200 nm-thick film of NCD using (a,c) a SE detector and (b,d) an inBeam BSE detector. (c), (d) Details of the antennas in the array. The sample was covered by a thin film of a conductive polymer Espacer 300z to prevent sample charging during imaging.

- Germanium on a potassium bromide (Ge on KBr, 1.0 – 25 μm spectral range) beamsplitter was replaced by a calcium fluoride beamsplitter (CaF_2, 0.2 – 2.5 μm spectral range).

The measured FTIR reflectance spectra of fabricated antenna arrays are shown in Figure 7.15a. The green arrow in the figure indicates the shift of the resonant peak with the length

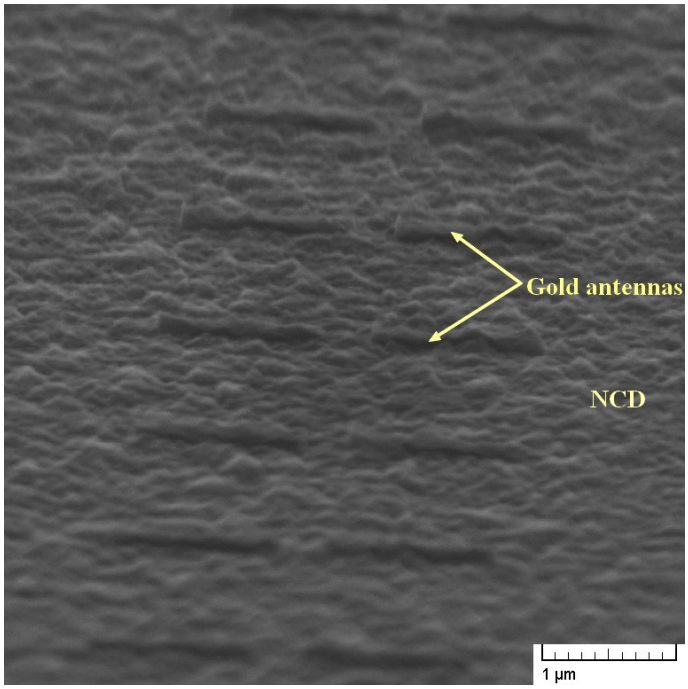

Figure 7.14: Scanning electron microscope image (Tescan Vega2) of gold antenna dimers fabricated on the NCD film. During the imaging, the sample was tilted by 75 ° with respect to the incident electron beam.

of antennas in the array. The resonant wavelengths of antenna arrays are then compared (Figure 7.15b) with the results of simulations for single antenna of similar dimensions. As the dimensions of the antennas are small and the resonant peaks are weak and broad, the measurement uncertainty of both the antenna dimensions and resonant wavelength is relatively big. However, one can still see that the measured resonant wavelength of the antenna arrays is red-shifted by approximately 100 nm with respect to resonant wavelength of single counterparts. Such a large difference cannot be attributed to the limited accuracy of the calculations. As the spacing in both directions between the antennas in the array is 0.5 μm, which corresponds to approximately to half of the resonant wavelength, the red-shift is partly contributed by the mutual interactions of antennas in the array. Further, non-zero angle of incidence of illuminating light also contributes to the red-shift [86].

Another interesting feature of the reflectance spectra in Figure 7.15a is the intense peak around 930 nm. Its position does not change with the length of the antennas, therefore this peak is not related to longitudinal LSPR.

Polarization properties of that peak can give us more information on its nature. Therefore, we put an NIR polarizer into the collection arm of the infrared microscope. In Figure 7.16 the resonant spectra of an antenna array (antenna length 187 nm) are shown for different polarization of the light reflected from the sample. When the light is polarized longitudinally, the LSPR peak is visible in the spectrum. The ratio between the peak at 930 nm and LSPR peak is significantly smaller then in the case when the light is not polarized. When the polarization is transverse, LSPR peak vanishes and the peak at 930 nm is higher and narrower. The peak at 930 nm is present for both longitudinal and transversal polarization. However, the intensity of reflected light at 930 nm is significantly higher for transverse (TE) polarization.

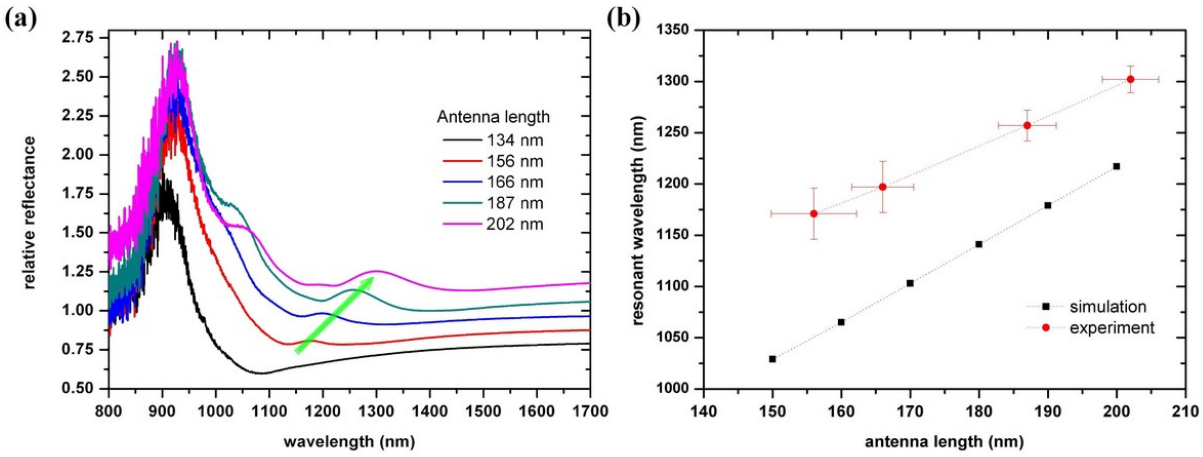

Figure 7.15: (a) Spectra of relative reflectance of gold plasmonic single antenna arrays of various antenna lengths fabricated by EBL on a fused silica substrate coated by a 200 nm-thick film of NCD. The light green arrow shows the position of the LSPR wavelength. The spectra were measured using microscopic FTIR (Bruker Vertex 80v + Hyperion 3000, InGaAs detector, CaF_2 beamsplitter). (b) Comparison of the experimental data with the results of FDTD simulations.

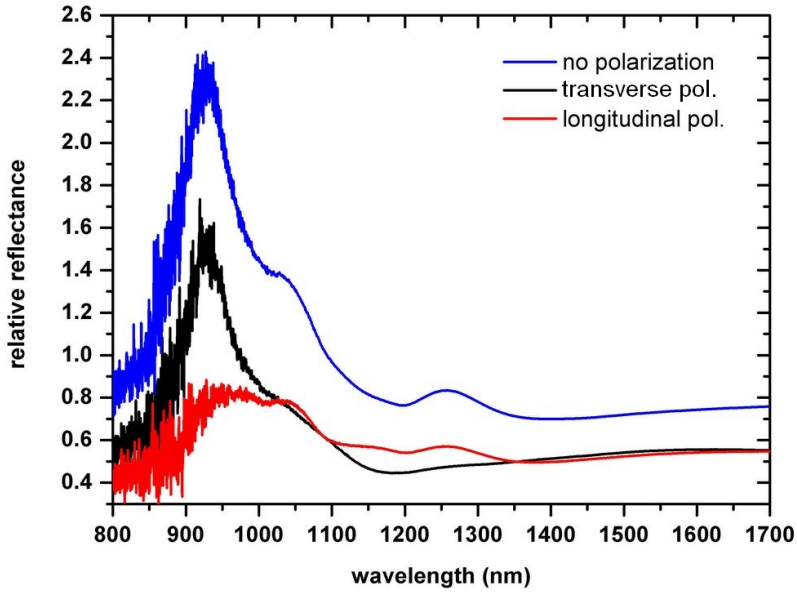

Figure 7.16: Relative reflectance spectra of an antenna array (antenna length 187 nm) for different states of light polarization.

Now, it will be shown that the peak at 930 nm is caused by the light interference in the NCD film. The refractive index of NCD film is higher than the refractive index of air, therefore, the light reflected from this film is phase-shifted by π. This phase shift corresponds to optical path difference (OPD) $\delta_1 = \lambda/2$. Under normal angle of incidence, the light reflected from the interface NCD-glass (see the inset in Figure 7.17) has OPD

$$\delta_2 = 2n_{\mathrm{NCD}}t, \tag{7.2}$$

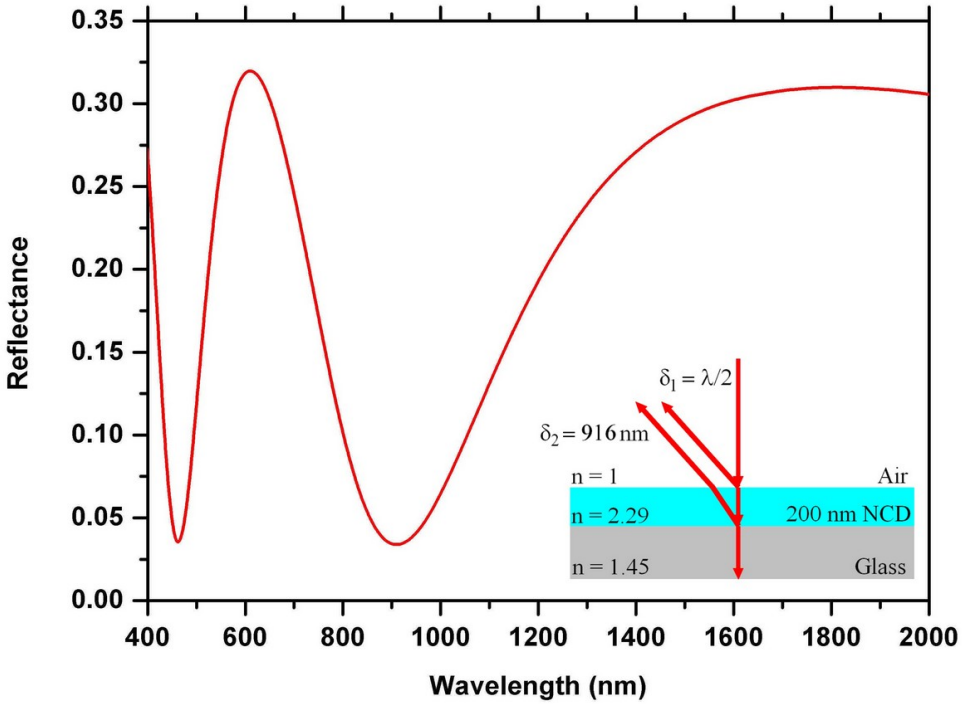

Figure 7.17: Calculated reflectance spectrum of a 200 nm-thick NCD film on the fused silica substrate under the normal angle of light incidence.

where $n_{\mathrm{NCD}} \approx 2.29$ is the real part of NCD refractive index and t is thickness of the film. In case of 200 nm-thick NCD film, $\delta_2 = 916\,\mathrm{nm}$. The light beams (the one reflected from air-NCD interface and the other from NCD-glass interface) interfere with each other. In case of interference minimum, the condition for the path difference Δ between the interfering light beams is following:

$$\Delta = \delta_2 - \delta_1 = (2m-1)\frac{\lambda}{2}, \tag{7.3}$$

where $m = 1, 2, 3, \ldots$ is the order of interference minimum. The solution of this equation yields

$$\lambda = \delta_2/m \tag{7.4}$$

$$\lambda = \delta_2 = 916\,\mathrm{nm}, \text{for } m = 1. \tag{7.5}$$

Therefore, for $\lambda = 916\,\mathrm{nm}$, the reflectance of the substrate reaches its minimum. The calculated reflectance spectrum of a glass substrate coated with 200 nm on NCD for normal angle of incidence is shown in Figure 7.17. The quantity measured by FTIR is a spectral response function of antennas which in reflection configuration of FTIR setup corresponds to relative reflectance R_{a} of antennas (which is shown in Figure 7.15a). To get this quantity, two measurements of the reflected light spectral intensity are taken by FTIR microspectrometer. One measurement is realized in the part of the sample, where no antennas are situated (I_{s}), and the other is realized on the array of antennas (I_{a}). The resulting relative reflectance R_{a} is given by its ratio

$$R_{\mathrm{a}}(\lambda) = I_{\mathrm{a}}(\lambda)/I_{\mathrm{s}}(\lambda). \tag{7.6}$$

At $\lambda = 916\,\text{nm}$ the reflectance of the substrate drops to its minimum; at this wavelength the intensity of reflected light reaches only 3 % of incident light intensity and the value of I_s can be consider as very small. On the other hand, the intensity of the reflected signal can be increased, when particles of a good reflector, like gold ones, are placed on the substrate surface. The gold antennas, which are sparsely[13] situated on the NCD film are clearly out of the resonance at $\lambda = 916\,\text{nm}$. Nevertheless, the antennas act as simple mirrors and their presence increases the reflected signal I_a. And since, I_s is relatively small around $\lambda = 916\,\text{nm}$, the value of relative reflectance R_a (Eq. 7.6) quite high around this wavelength.

In the experimental spectra of relative reflectance of antenna arrays (Figure 7.15a), we found a large peak at 930 nm and we explained its origin in the foregoing text. However, according to our theory, the peak position should be at 916 nm. This difference can be caused by a combination of several factors. First, the refractive index of NCD could be slightly higher (up to $n_\text{NCD} = 2.32$). Second, the NCD film could be thicker. A change of NCD film thickness by 3 nm to 203 nm would shift the peak position to 930 nm. Last, but not least the influence of the angle of light incidence has to be mentioned.

In the theory, we operate with normal incidence of the light. However, the geometry of Cassegrain 36× objective (see Figure 6.4), which we used in the measurements, prohibits the normal incidence of the light. Actually, the secondary mirror of the objective blocks the light which would hit the sample under the angle smaller then 10 ° [86]. Non-zero angle of incidence means that the OPD δ_2 is bigger than in our calculations and so has to be the wavelength, where the relative reflectance reaches its minimum. The angle of incidence 15° would result in the shift of the peak posiiton from 916 nm to 922 nm.

Chapter conclusion

This chapter dealt with the investigation of the resonant properties of gold plasmonic slab-like antennas situated on a glass substrate coated by a nanocrystalline diamond thin film. The investigation were mostly done by numerical calculations in Lumerical FDTD Solutions software. Simulations investigated the antenna resonant wavelength, scattering cross section and near-field enhancement upon the localized surface plasmon resonance. Where possible, the resonant properties of antennas on NCD film are compared with the properties of antennas situated on a bare glass substrate.

Despite the fact that none of the analytical models presented in Chapter 4 can be used to describe the exact resonant properties of slab-like antennas under our investigation, these models can still provide us with the information on the general trend in the resonant properties upon the change of antenna parameters. Equation (4.23) can give us information on the relative change of the antenna resonant wavelength upon the change of the antenna dimensions, Equation (4.19) gives us information about the relative intensity of the light scattered by the antenna and Equation (4.15) about the enhancement of the antenna near-field.

[13] The coverage goes from approximately 4 % for the smallest antennas to approximately 6 % for the biggest ones.

Simulations with varied antenna dimension showed that the antenna resonant wavelength as well as antenna resonant scattering cross section are scaled linearly with antenna geometrical length (Figure 7.4a, b) which both corresponds well to the models (Section 4.3.2) . Also the blue-shift of the antenna resonant wavelength with the increase of antenna width and height (Figure 7.5a, b) is in good agreement with the model (Eq. 4.23).

The resonant wavelength of antennas located on NCD film (refraction index 2.3) is significantly red-shifted with respect to the resonant wavelength of the same antennas on a bare glass substrate (refraction index 1.45). This corresponds well to the sensitivity of the antenna to the optical properties of surrounding media as shown, for example, in Equation (4.1). The resonant cross section of the same antennas on NCD and glass also differs significantly. Due to red-shifted resonant wavelength the antennas on NCD have smaller scattering cross sections, because according to Equation (4.19) the antenna scattering cross section is proportional to $1/\lambda^4$.

The resonant wavelength of dimer antennas is red-shifted with respect to the resonant wavelength of single counterparts (Figure 7.4a). This is consistent with the literature [84] and the shift is caused by the mutual interaction of longitudinal dipole modes of the dimer antenna rods, which are separated only by a gap of several tens of nanometres. As the size of the gap decreases, the interaction of the dipoles gets stronger and the red-shift of the antenna resonant wavelength increases (Figure 7.7). Smaller distance between the antenna rods of dimer leads to higher field enhancement in the antenna gap, as the dipole field from one antenna rod is *boosted* by the presence of the same field from the dipole in the other antenna rod.

The investigation how the antenna resonance is affected by the thickness of NCD film beneath the antenna showed that all the resonant properties and especially the antenna resonant scattering cross section are significantly sensitive to the thickness of the NCD film (Figure 7.6).

As the NCD interface in the close vicinity of the resonant antenna became the subject of our interest due to possible biosensing application, we also investigated how the antenna resonance is influenced by the mutual position of antenna and the NCD film or segment (configurations are shown in Figure 7.8). From Figure 7.9a, it can be seen that the antenna is most sensitive to the presence of NCD film, when the antenna is placed directly on glass substrate and the NCD film is grown around the antenna (Figure 7.8b). On the other hand, when NCD segment is placed on the top of the antenna only (Figure 7.8c), the antenna spectral sensitivity is the worst from all the investigated configurations. However, when a detection technique based on near-field enhancement (all the surface enhanced spectroscopic techniques) is used, the figure-of-merit is not the antenna spectral sensitivity, but the value of near-field enhancement and therefore, the most suitable configuration for these techniques is the one, where NCD film is situated between the substrate and the antenna (Figure 7.8a).

For the experiment, single gold plasmonic antenna arrays were fabricated by EBL on a fused silica substrate coated by 200 nm-thick film of NCD. Measurements of antennas resonance spectra (microscopic FTIR, InGaAs detector, CaF_2 beamsplitter) showed the antenna LSPR wavelength red-shifted by approximately 100 nm with respect to the resonant wavelength of simulated antennas of similar dimensions. As the main reason of the

red-shift we estimated the mutual interaction between the antennas in the arrays and the non-zero angle of light incidence in the experimental setup. Both shift the resonance into higher wavelengths.

The preliminary results, similar to those showed in this chapter, were presented by the author in form of poster presentation at two conferences – at Diamond 2011, International Conference on Diamond and Carbon Materials in September 2011 (Garmisch-Partenkirchen, Germany) and NFO 12, Near Field Optics conference in September 2012 (San Sebastian, Spain). Soon, the manuscript covering this topic will be submitted to a peer-reviewed journal.

8 Functionalization of antennas for biosensing

A LSPR wavelength sensitivity to the changes of the refractive index of the surrounding medium makes plasmonic antennas ideal for sensing. The presence of a material around antennas results in changes of the effective refractive index and therefore in a shift of LSPR wavelength. To ensure that antennas will detect only the presence of the specific agents, samples with antennas have to go through the process of functionalization. In this process, the surface of antennas is modified by substances which bond to as a few other substances as possible, but which had a strong bond to an agent which presence should be detected. Ideal for the role of such mediator between antennas and detected agent are bio-molecules. Main advantage of bio-molecules usage is their highly-specific interaction (e.g. antigen-antibody interaction) and a possible tuning of molecular length and topology [87]. The main goal of our work in this field was to use the antennas to sense the presence of streptavidin in their vicinity.

8.1 Functionalization techniques and modes

The functionalization of nanoparticles with bio-molecules has been widely studied for its application in inorganic-organic interfaces. Following functionalization techniques have been developed [88]:

electrostatic binding – This is a nonspecific straightforward binding technique, when positively charged bio-molecules are bound to nanoparticles which surface is stabilized with negatively charged molecules, like sodium citrate.

specific affinity interactions – The nanoparticles are functionalized by bio-molecule which specifically interacts with other bio-molecule. One of the most typical cases of this type of functionalization is the binding between biotin and streptavidin.

covalent binding – This can occur with relatively specific chemistry between the surfaces and functional group. The typical case of the covalent binding is the chemisorption of thiol derivatives onto the surface of gold particles, where rather stable Au-S bonds are formed.

The functionalization takes place at one of the following spatial modes:

N:1 – The most typical spatial mode in which the surface of the nanoparticles is functionalized by bio-molecules. It occurs when no control mechanism over the bio-molecule deposition is employed. A single particle is covered by a random number (N) of bio-molecules, hence the label N:1.

1:1 – A nanoparticle binds with a single bio-molecule only. This is usually achieved only by using very small nanoparticles.

anisotropic – By employing a suitable geometrical restriction the binding of bio-molecules to specific parts of nanoparticles is blocked. The bio-molecules are then bound to specific particle regions only.

8.2 Samples and methods

Author of this thesis fabricated several samples with arrays of gold plasmonic dimer antennas (length 0.6–2.0 μm, width 0.4 μm, height 0.06 μm, gap between the rods of dimers 0.2 μm) on Si(100) substrates by EBL. In Figure 8.1, there is a dark-field image of a fabricated sample with antenna arrays depicted together with a detail of a single array and a single dimer antenna. These samples were brought to Elettra synchrotron facility in Trieste, Italy, where they were functionalized (covalent binding technique, N:1 spatial mode) in cooperation with Nano-Innovation Laboratory of Dr. Loredana Casalis. The mid-IR optical response of functionalized antennas was measured at SISSI beamline with the assistance of Dr. Lisa Vaccari. The response was measured before and after each of the functionalization steps by micro-FTIR Bruker Vertex 70 connected with infrared microscope Hyperion 3000 using conventional reflection setup (Globar light source, Ge on KBr beamsplitter, LN_2 cooled MCT detector).

8.3 Functionalization process

At first, the samples were cleaned off any possible organic contamination in an oxygen plasma (75 % Ar, 25 % O_2, 120 s, 30 Pa). O_2 plasma treatment also made the surface of Si hydrophilic which is crucial for the successful functionalization. The functionalization process consisted of three major steps which are schematically shown in Figure 8.2. The

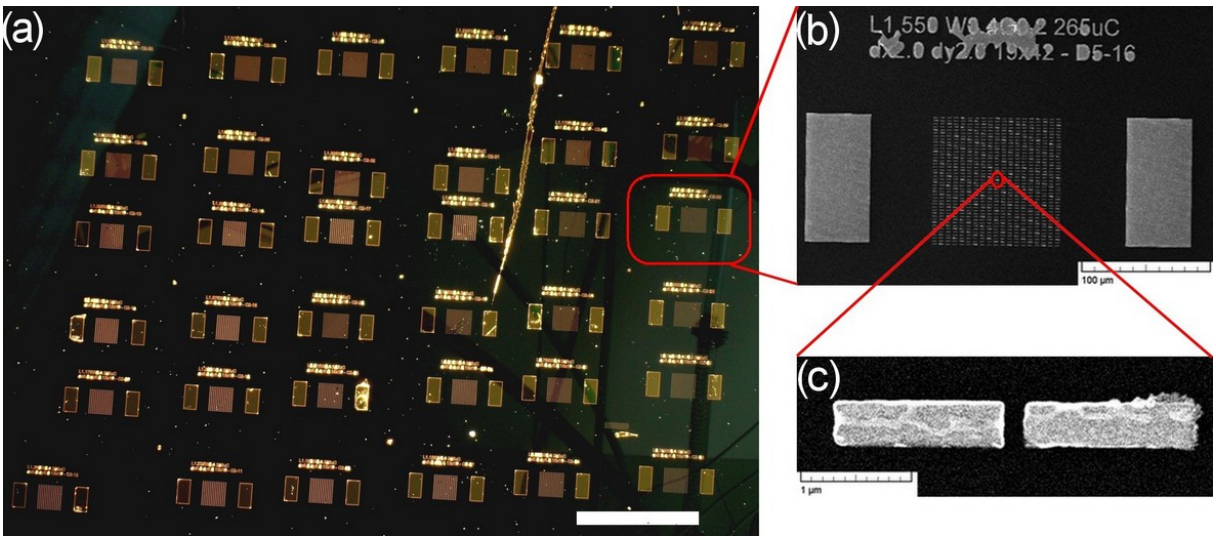

Figure 8.1: A sample with gold plasmonic antenna arrays fabricated by EBL on a Si substrate. (a) The dark-field image from an optical microscope (Olympus MX51); the white bar corresponds to 500 μm, (b) an array of dimer antennas imaged by SEM (Tescan Vega2), (c) a detail of a single dimer antenna.

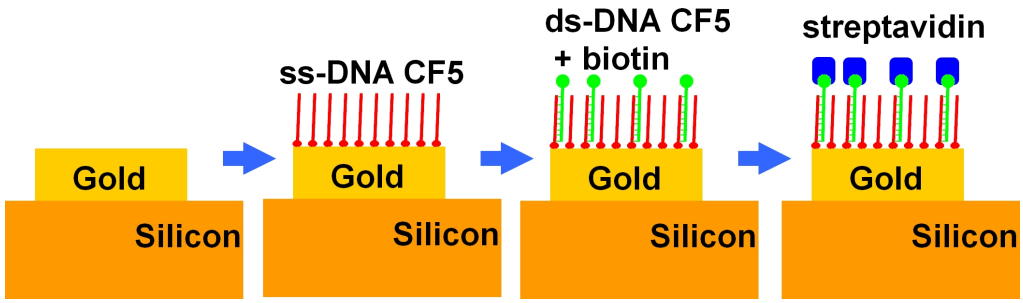

Figure 8.2: A simple scheme of functionalization steps. The first step is to bind thiolized 24-basis-single-strand (ss) DNA chains of the coagulation factor 5 (CF5), the second one to hybridize the bound CF5 strands with a complementary CF5 ss-DNA basis with biotin molecules at the end of the chains, and the final step was to bind streptavidin from an investigated solution to biotin molecules.

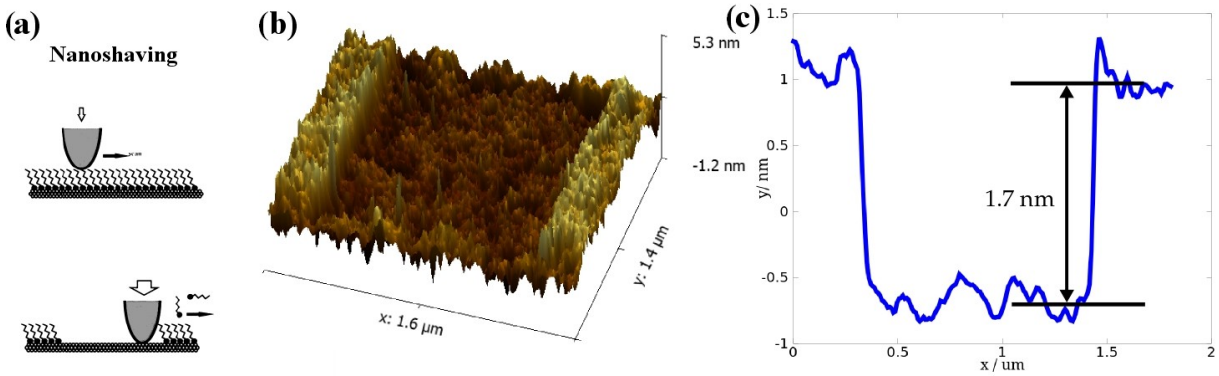

Figure 8.3: (a) Schematic of the nanoshaving principle, taken from [89], (b) a topographic AFM measurement taken after AFM nanoshaving of the gold antenna after the first functionalization step and (c) the height profile of the shaved area. A drop in the height profile means that organics were removed from this area by nanoshaving. Therefore, the drop confirms the success of the first functionalization step.

first functionalization step was to bind thiolized 24-basis-single-strand (ss) DNA chains of coagulation factor 5 (CF5) from phosphate buffer saline (PBS) solution to gold antennas by the chemisorption of thiol molecules to gold. This covalent coupling of ligands to nanoparticles is a reliable and robust route to add both the function and chemical stability. After that, the CF5 strands which were bound to the gold by the physisorption (instead of intended chemisorption) were removed using a solution of ethylene-glycol-terminated alkylthiol (TOEG6).

The success of this first functionalization step was proved by the atomic force microscope (AFM) nanoshaving. In this technique an AFM tip exerts high local pressure which induces a high shear force acting on the adsorbed. As the Au-S bond is the weakest in the molecular chain [89], the pressure eventually leads to the displacement of thiol molecules from their adsorption sites and therefore, to the displacement of whole adsorbents. In Figure 8.3 one can see a schematic of the nanoshaving (a), topography (b) and a height profile of shaved part (c). The drop in the height profile shows the area from which the organics were removed by nanoshaving; this indicates the presence of the CF5 strands.

The second step was to hybridize the CF5 strand at the antennas by a complementary CF5 ss-DNA basis with biotin molecules at the end of its chains. Biotin binds strongly to streptavidin, therefore it mediates binding of streptavidin to antennas in the case of its presence in investigated solutions. The binding between biotin and streptavidin is the strongest known non-covalent and completely reversible bond [87]. The final step was to drop an ethanol solution with streptavidin over the antennas and rinse it by DeMi water after an hour.

8.4 Streptavidin detection

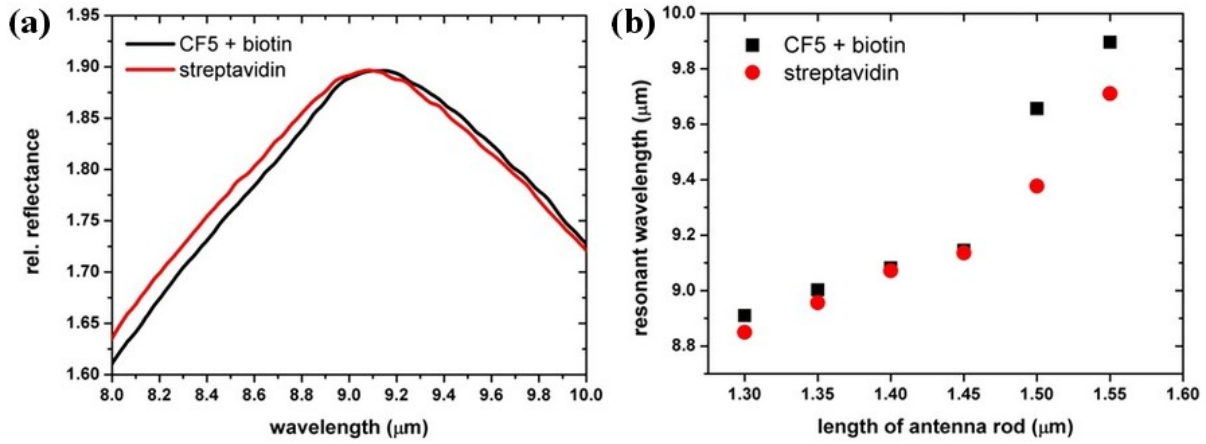

Figure 8.4: (a) Localized surface plasmon resonant peaks of a gold dimer antenna array (length of antenna rods 1.40 μm) functionalized by a double stranded DNA chain CF5 with the biotin molecule (black) and streptavidin bound to biotin (red), and (b) the wavelengths of the resonant peak maxima for the arrays of the rods with the length between 1.30 and 1.55 μm.

FTIR measurements (in reflection configuration only) were performed after each functionalization step. However, the most important was the difference in spectra which were taken before and after last step (i.e. without and with streptavidin). The slight shift in spectra measured before and after adding streptavidin on the sample (Figure 8.4) shows that we have successfully indirectly detected its presence. However, this spectral shift is relatively small in comparison with the results which were achieved in visible spectral region and presented, for example, in [24].

8.5 Influence of graphene layer

From the aforementioned results, we know that the antennas are capable to detect the presence of a single layer of self-assembly molecules on their surface. To find if the antennas are capable to sense the presence of a single atomic layer on their surface, we decided to cover the already functionalized antennas by a single layer of graphene.

The graphene was prepared (CVD) on a substrate of copper foil from CH_4/H_2 plasma of 22:13 sccm ratio, the pressure of approximately 10 Pa and the temperature of 1000 °C.

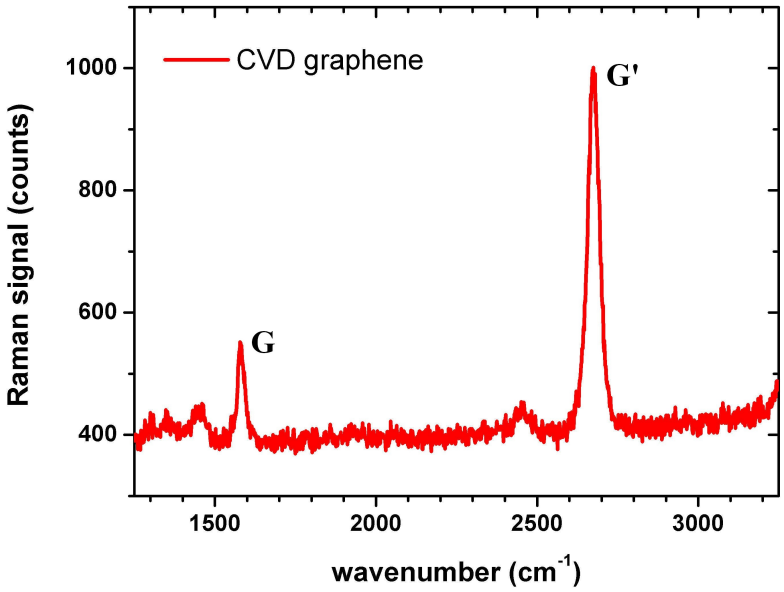

Figure 8.5: Raman spectrum of a graphene layer placed over the plasmonic antennas. The Raman G' peak at 2687 cm^{-1} is very narrow and its intensity is significantly higher than the intensity of the G peak. According to [90], these two features are specific for the Raman signal of the single-layer graphene.

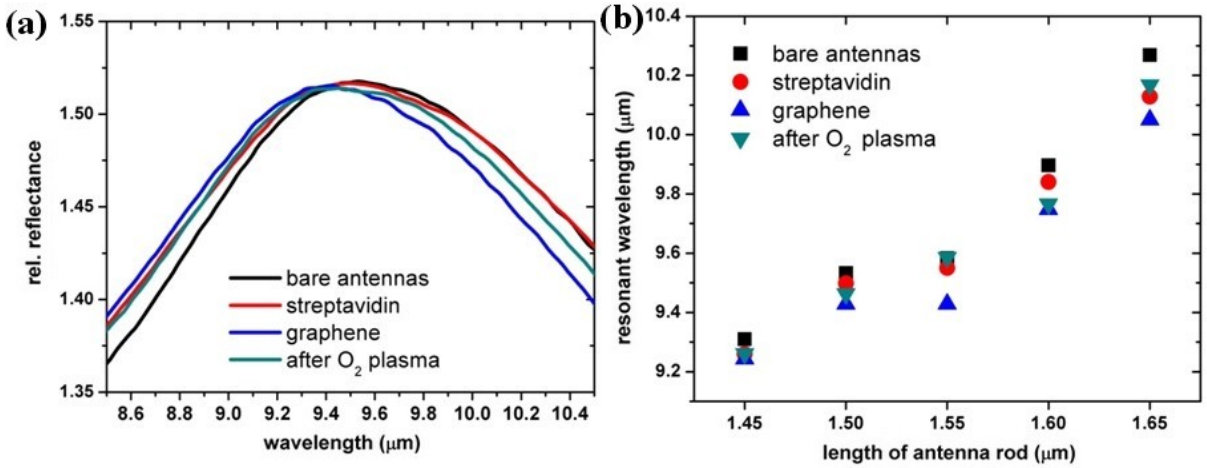

Figure 8.6: (a) Localized plasmon resonant peak of a gold dimer array of antenna rods with the length $L = 1.50\,\mu$m (black) and its shift caused by the presence of streptavidin at the antennas (red), by covering the antennas by a single layer of CVD graphene (blue), and after the removal of graphene and organics in oxygen plasma (turquoise), and (b) the wavelength of the resonant peak maxima for arrays of gold dimer antennas with the rod lengths between 1.45 and 1.65 μm.

Later, it was transferred from the copper foil on the sample with functionalized antennas. The Raman spectrum of this graphene layer (NT-MDT Ntegra Spectra, laser wavelength 532 nm) in Figure 8.5 shows a very narrow Raman G' peak of graphene which has significantly higher intensity than G peak. This unique feature confirms that it is indeed a single

layer of graphene. FTIR measurements of relative reflectance of plasmonic antennas covered by this graphene single layer showed (Figure 8.6) shift of the resonance wavelength caused by the presence of graphene. After these measurements the samples were cleaned again in O_2 plasma which removed graphene and organics (DNAs, streptavidin, ...). The FTIR measurement of antenna resonant spectra taken after O_2 plasma cleaning showed a back-shift in antenna resonant wavelength. Despite that the shifts of resonant wavelength were relatively small, these measurements showed that the antenna arrays are capable to sense the presence of materials as thin as single atomic layer in the close vicinity of the antenna arrays.

Antennas as nucleation centres

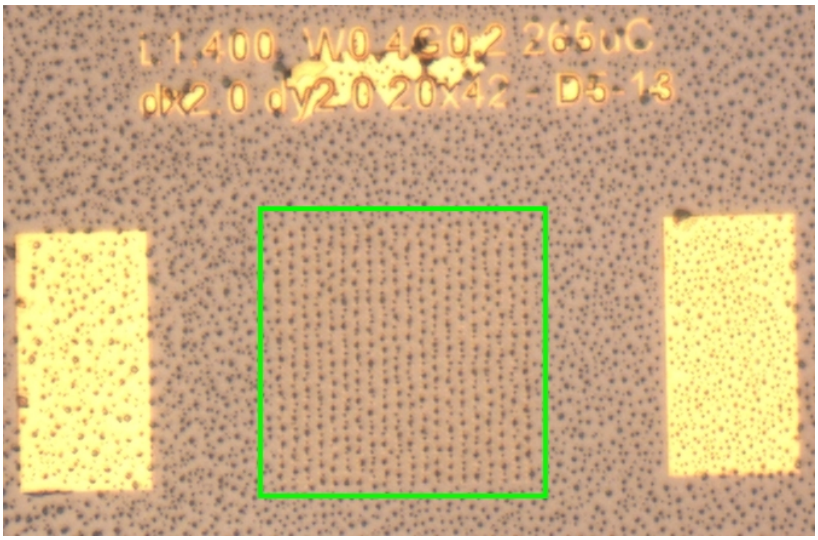

Figure 8.7: Salt (most probably NaCl) crystals (dark spots) formed after the insufficient removal of the functionalization solution (PBS) from the sample. The location of the crystallites seems arbitrary, with the exception of an area inside the green square, where an array of plasmonic antennas is fabricated. In this area the crystallites are well-ordered. The antennas probably serve as a matrix of sites for nucleation of crystallites.

A side-result of the aforementioned study is that we found that antennas or the gaps between antenna rods, can serve as nucleation centres for crystallization. For one of the samples a film of phosphate-buffered saline (PBS) on its top persisted the rinsing after the functionalization and was dried by N_2. As one can see in Figure 8.7, the salt crystallites started to nucleate from PBS preferably in the gaps between the antennas. Therefore, due to ordered arrangement of arrays, the crystallites are also ordered in matrix-like arrangement in comparison to areas without antennas, where no ordering was observed.

Chapter conclusion

This chapter dealt with the functionalization of gold plasmonic dimer antennas in order to sense the presence of specific agent. Functionalization was done by binding the thiolized single strand DNA chains of coagulation factor 5 to the antennas and their following

hybridization with complementary chains terminated by biotin molecules. The sensed agent was streptavidin.

By comparison of antennas resonant spectra before and after the binding of streptavidin, one can see that the binding of streptavidin to biotin caused a slight shift of the LSPR wavelength. Similar shift was observed also for covering the antennas by a single layer of graphene. The shift was reversible; after the removal of the sensed agents by oxygen plasma cleaning, the antenna resonant wavelength shifted back.

As the presence of material around the antennas resulted in shift of resonant wavelength and its removal to back-shift of resonance, we can declare that the antennas are sensitive even to single atomic layer of material. However, the relative shifts of antenna resonant wavelength are very small in comparison with the results obtained for antennas in visible spectral region [24].

Results shown in this chapter were presented as the oral contribution by the author in Paris, at IVC 19, International Vacuum Congress, in September 2013.

9 Unidirectional antennas

As shown in [47] and [48], plasmonic antennas can serve for coupling the light into optical waveguides. Let us imagine a plasmonic antenna on top of an optical channel or rib waveguide. Refractive index of the waveguide has to be higher than the index of the bottom cladding and surrounding air serves as a side- and top-cladding. Plasmonic antennas preferentially scatter the incoming light in the medium of a higher refractive index [47]. Therefore, the light coming from air is partially *redirected* by the antennas into the waveguide. When illuminated under a normal angle of incidence, straight rod-like antennas scatter the same amount of light in both waveguide directions [91]. When specific configuration (e.g. Yagi-Uda) [47] or geometry (e.g. V-shape) [91] of rod-like antennas is used, the light scattering can be highly directional at specific wavelengths.

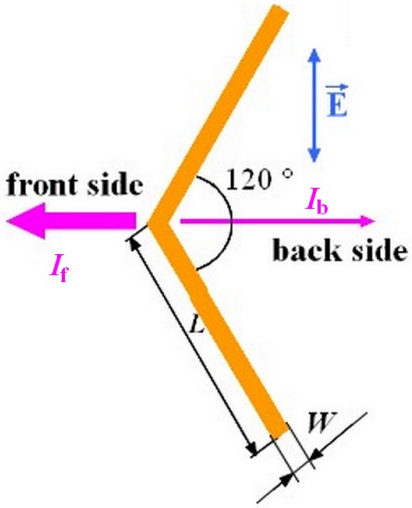

Figure 9.1: A schematic top-view of a V-shaped plasmonic antenna. The blue arrow shows the polarization of the electric component of the incoming electromagnetic wave. All the V-antennas which are presented in this thesis have the inner angle between the antenna rods 120 °. According to [91], the directional effects of V-antennas are the biggest for this value of the inner angle. We label the region of the outer part of the V-antenna (left) as the *front side*, and the inner part (right) as the *back side*.

In this chapter, we will deal with the plasmonic V-shaped antennas. The V-shaped antenna (or shorter V-antenna) consists of two identical antenna rods of length L, width W and height H which enclose an angle 120 °. The geometry of the V-antenna is shown in Figure 9.1.

In the theory of antennas, the figure-of-merit for an antenna is represented by antenna directivity D. There exist several definitions of this quantity [92, p. 44–56]. For our needs, we adopted the definition from [91], where the directivity D is defined by following relation as a ratio between the light intensity scattered by V-shaped antenna into the front side (I_f) and back side (I_b):

$$D = 10 \log_{10} \frac{I_f}{I_b} \text{ [dB]}. \tag{9.1}$$

According to [91] and [93], where the principles of V-antenna directivity are explained, the directivity of V-shaped antennas on planar substrate can reach up to 20 dB for wavelengths close to the that of the antenna quadrupole mode.

9.1 V-shaped antennas for visible and near-infrared region

During his internship in IMEC research institute in Leuven, Belgium, the author of this thesis joined the project of experimental evaluation of the directivity of V-shape antennas on silicon nitride waveguides, where the FDTD simulations showed that the V-shape antenna placed on a waveguide is less directional than the antenna on the planar substrate, but the directivity still can be as high as 10 dB. In Figure 9.2, one can see a scheme of the antenna on the silicon nitride waveguide as it was designed in IMEC.

The fabrication process was following. A silicon substrate with a 2μm-thick film of the thermally grown silicon dioxide and 180 nm of silicon nitride (Si_3N_4) was coated by a 10nm-thick film of sputtered titanium and 50 nm of gold. The gold film was then coated by a film of ma-N 2403 negative resist. Using the EBL, a mask of V-shape antennas of the rod length L ranging from 180 to 250 nm and the inner angle between rods of 120 ° was drawn into the coated resist film. After the development, the pattern of the mask was transferred to the gold film by Xe-ion milling, which removed all the gold, but the parts covered by the resist. Then, samples were coated by FOx-12, a hydrogen silsesquioxane (HSQ) based negative resist, and another EBL process was used to draw a mask of waveguides. After the development, the mask pattern was transferred to Si_3N_4 by SF_6/C_4H_8 inductive coupled plasma reactive ion etching (ICP/RIE) that removed all

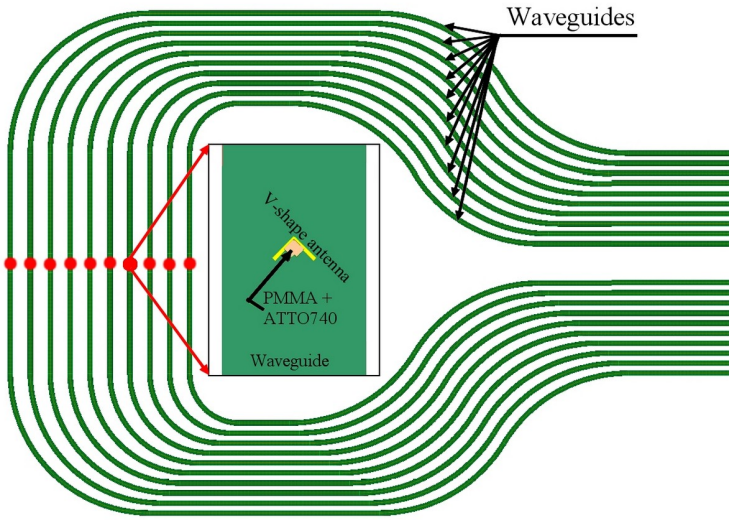

Figure 9.2: A part of the EBL mask with a set of channel waveguides as was designed in IMEC, Belgium. A single gold antenna (or an array of antennas up to 5 × 5) is situated on top of the waveguides in the middle of their length. A mixture of PMMA and the ATTO740 NIR fluorescent dye is located in the antenna inner part. The red dots mark the places, where the antennas are placed.

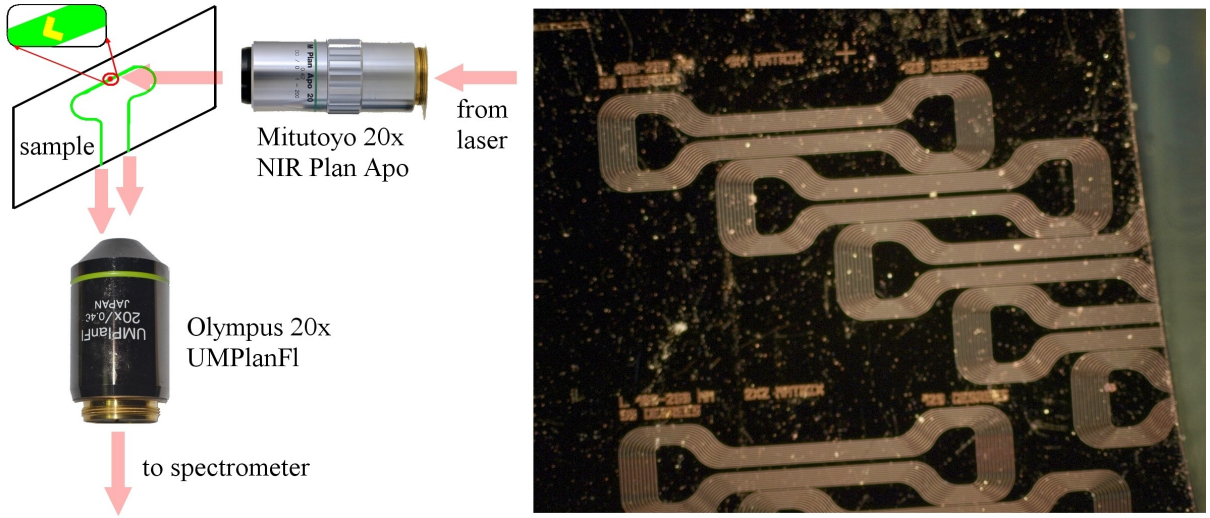

Figure 9.3: Schematic of an experimental optical setup (left) and a dark-field microscope image of Si_3N_4 channel waveguides (right).

Si_3N_4 with the exception of parts covered by FOx-12. The last fabrication step was the coating of samples by a mixture of the PMMA positive resist and the ATTO740 fluorescent dye. After the EBL and the development, the PMMA with ATTO740 molecules was removed from Si_3N_4 waveguides and from the vicinity of antennas with the exception of specific area in the inner part of V-antenna (see Figure 9.2).

For the measurements, the samples were diced to several pieces which were attached to the sample holder by a two-side duct-tape. For the illumination of antennas, Spectra physics Tsunami pulse laser at 730 nm was used. The light from the laser (optical power 700 mW, 80 MHz repetition rate) passed through a set of attenuators and was coupled to a multimode optical fiber. At the experimental setup, the laser light was outcoupled from the fiber and focused by 5× objective on a pinhole with the diameter of 5μm, which acted as a spatial filter. Light from the pinhole passed through 750 nm short-pass filter and was collimated and directed into the objective (Mitutoyo NIR 20×, NA 0.40), which focused the light on antennas located on the top of a single waveguide. The light (both laser light and fluorescence of ATTO740) was partially coupled by the antennas to the waveguide. The power of the light illuminating antennas was estimated to be in units of mW due to high losses in the excitation path.

A collection objective (Olympus UMplanFl 20×, NA 0.46) was focused on the edge of the sample part, collected the light coming out of the waveguides and directed it through 750 nm long-pass filter (to filter laser light from the detected signal) into an imaging spectrograph (Newport MS260i). A simple schematic of experimental configuration is in Figure 9.3.

During the measurements of the fluorescence coupling into the waveguide a serious issue arose. As PMMA with ATTO740 molecules was left everywhere on the sample, but waveguides and regions with antennas, the ATTO740 molecules in PMMA acted as optical inhomogeneities. These inhomogeneities caused both the scattering of incoming laser light and the photoluminescence emission from illuminated area. Some of the light was scattered or emitted almost parallel with the sample surface, directly to the collection

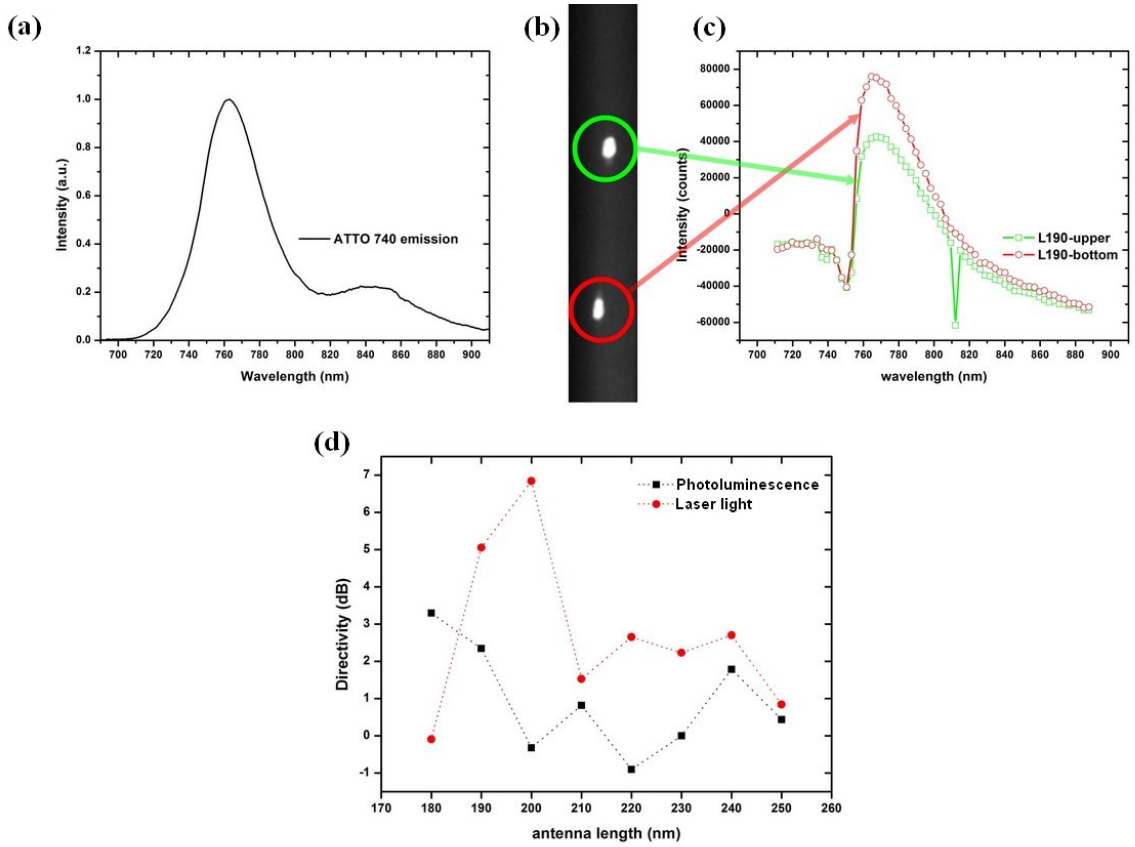

Figure 9.4: (a) Emission spectrum of the ATTO740 luminescent dye, (b) photoluminescent signal of ATTO740 as detected by a CCD camera of the spectrograph, (c) spectral analysis of the bright spots from (b) shoving emission from ATTO740 and the long-pass filter cut-off wavelength at 750 nm, (d) directivity of antennas based on the ratio between the intensities of light coming out from both waveguide ends.

objective and spectrograph. These signals were much more intense than the light coming out of the waveguides. Therefore, it was practically impossible to focus the collection objective on the sample edge. To reach the reliable detection of the signal from waveguides this issue had to be solved. By a change of the collection objective, a precise mutual alignment of both objectives and a correction of sample tilt, together with a modification of white light illumination part of the experimental setup, we were able to get much better images of the sample edge and therefore, we were able to stay in focus on the sample edge.

Measurement parameters were the same for measurements of background and the photoluminescence signals – 60 s acquisition time and 10 accumulations using 750nm long-pass filter. Background signal was later subtracted from the photoluminescence signal.

Measurements obtained during author's stay in IMEC show that V-shaped antennas successfully couple incident light as well as the light from emitters situated nearby the antennas into waveguides. Due to the low-symmetry of the antenna shape this coupling is directional with the directivity up to 7 dB (Figure 9.4) for the excitation laser but much smaller the fluorescence signal, where the directivity oscillates from 2 dB to -1 dB. Nevertheless, such low directivity has been reported for similar antennas by Vercruysse in [93].

Despite the achieved results, the presented measurement technique was proved to be very impractical. First, the measurements are very time-consuming. One measurement (setup alignment, background and photoluminescence signal measurement) took usually more than 40 minutes, one set of waveguides then usually took whole day. The second issue is connected to cleanness of the sample. Dust particles on the top of the waveguides can outcouple the guided light. When these particles are located in the gap between the waveguides, then the guided light leaks into neighboring waveguides. Both can distort the detected signal. To eliminate this issue, the sample must be as clean as possible. As the detected photoluminescence signal is very weak, the measurements are very sensitive to the change of the ambient light and even mechanical conditions (e.g. vibrations from footfalls or conversations).

9.2 Infrared V-shaped antennas

Due to the availability of IPE BUT fabrication and detection capabilities, further investigation of V-shaped antennas resonant properties were done in mid-infrared spectral region.

9.2.1 Analytical model

Author of this text supervised a bachelor thesis [94], where Kalousek's model [54] were successfully expanded to determine not only the wavelength of V-shaped antenna dipole and quadrupole mode, but also the planar antenna radiation pattern at specific wavelengths. The author of this text run a series of simulations (Lumerical FDTD Solutions) to study the properties of the V-shaped antennas in the infrared spectral region. This enabled to compare the results of numerical computations with the newly developed analytical model. The results of both models were in a good agreement (see Figure 9.5).

9.2.2 FDTD calculations

Series of numerical computations were run in Lumerical FDTD Solutions to determine the resonant properties of the V-shaped gold plasmonic antennas. To reduce the time complexity of the simulations, the model of free-standing antennas (no substrate) was used. As the simulations were done in mid-IR spectral region, where metals are good conductors and both Si and CaF_2 substrates have negligible absorption, it was then very easy to estimate the resonance of antenna on substrate from the results for free-standing antenna. The *nature* of this conversion consists in multiplication of the wavelength scale by substrate index of refraction. The resonant spectrum of free-standing gold V-antenna of length $L = 2.5\,\mu$m is shown in Figure 9.6. In this spectrum, peaks of both the dipole and quadrupole mode are clearly visible.

The dipole and quadrupole mode differ by charge distribution over the antenna and therefore, by the electric field in the antenna vicinity, as it can be seen in Figure 9.7a,b. These

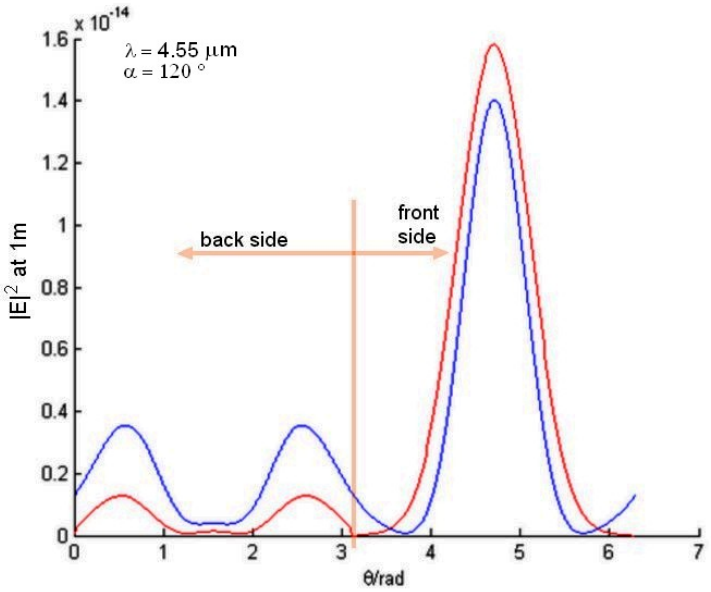

Figure 9.5: Planar V-antenna angular dependence of the electric field (square of the amplitude) scattered by the antenna in a distance of 1 m from the antenna for wavelength $\lambda = 4.55\,\mu$m calculated analytically by expanded Kalousek's model (blue curve) and numerically by Lumerical (red curve). Parameters of the free-standing antenna are: $L = 2.5\,\mu$m, $W = H = 50\,$nm. Taken from [94].

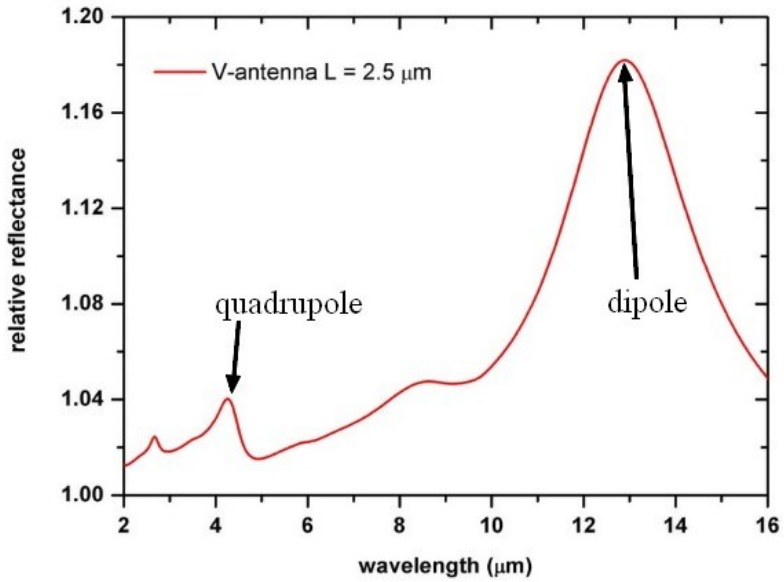

Figure 9.6: Calculated resonant spectrum of a free-standing V-shaped antenna ($L = 2.50\,\mu$m, $W = H = 50\,$nm).

differences in antenna near-field also affect the antenna far-field. While the angular radiation pattern of dipole mode is almost the same for both scattering directions (Figure 9.7c,e), the pattern of quadrupole (Figure 9.7d,f) differs significantly. It seems that at the wavelength of the quadrupole mode the most of the incident light is scattered to the

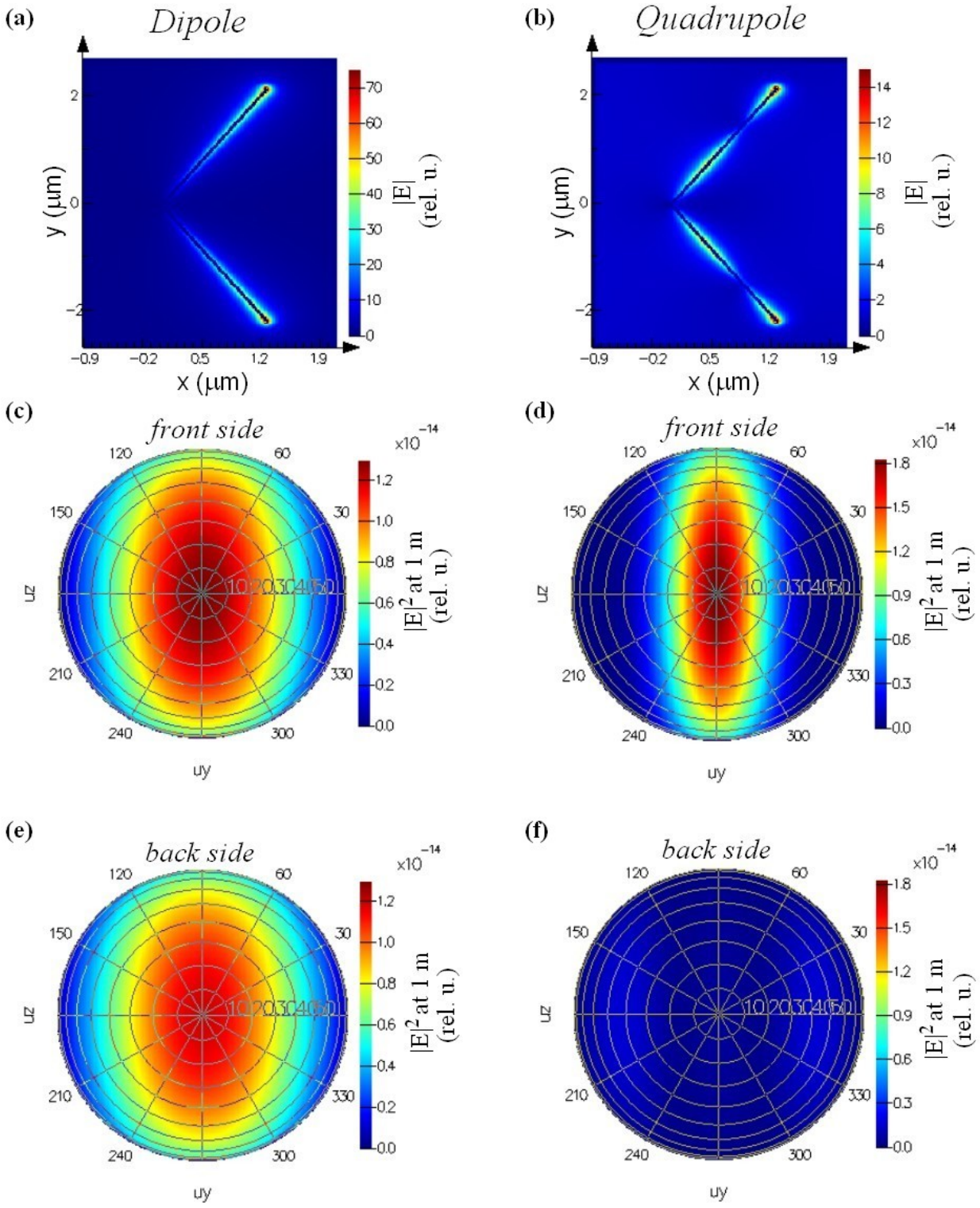

Figure 9.7: Visualization of the electric field around the antenna when the antenna dipole (a) or quadrupole (b) mode is excited. The angular dependence of intensity of light scattered by the antenna into the front side half-space when the dipole (c) or quadrupole (d) mode is excited. The angular dependence of intensity of light scattered by the antenna into the back side half-space when the dipole (e) or quadrupole (f) mode is excited.

half-space in front of the antenna, while at the wavelength of dipole mode, the antenna scatters approximately the same amount of light in both half-spaces.

By integration of light intensity distribution (like those shown in Figure 9.7c–f) in both half-spaces for different wavelengths, we calculated the intensity of the light scattered by the V-shaped antenna in each of the half-space. Then, we used Equation (9.1) to calculate the antenna directivity D. In Tables 9.1 and 9.2 there are shown calculated directivities for the wavelengths of the dipole mode, the quadrupole mode, and the wavelength at which the directivity reaches its maximum.

Table 9.1: Wavelength of modes and directivity of free-standing V-antenna ($L = 2.5\,\mu$m, $W = 0.05\,\mu$m, $H = 0.05\,\mu$m).

	dipole mode	quadrupole mode	maximum of directivity
wavelength (μm)	12.89	4.25	4.45
directivity (dB)	0.19	4.88	9.45

Table 9.2: Wavelength of modes and directivity of free-standing V-antenna ($L = 2.5\,\mu$m, $W = 0.4\,\mu$m, $H = 0.05\,\mu$m).

	dipole mode	quadrupole mode	maximum of directivity
wavelength (μm)	11.69	3.75	4.02
directivity (dB)	1.33	3.18	5.72

9.2.3 Experiments

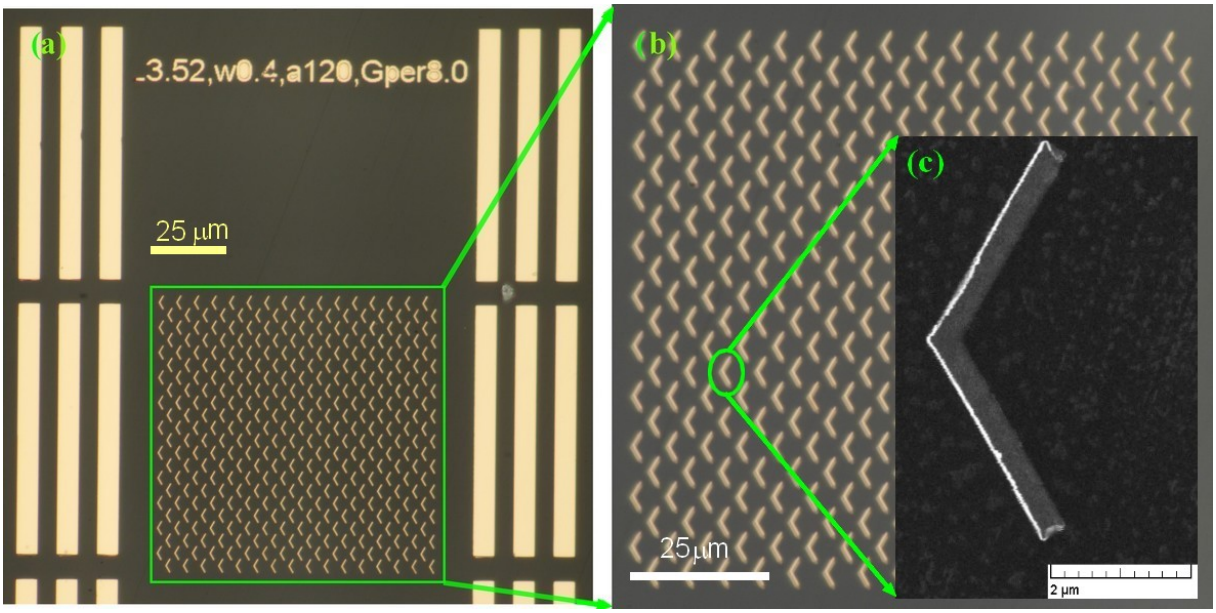

Figure 9.8: Bright field microscope (Olympus MX51) images (a) and (b) of fabricated gold plasmonic V-antennas on the CaF_2 substrate. (c) Detail of a single antenna (SEM, Tescan Vega2).

Series of V-shaped gold plasmonic antenna arrays ($100 \times 100\,\mu m^2$) were fabricated by EBL on substrates of Si(100) and CaF_2. Due to the limitation of our fabrication capabilities, the width of the antennas was set to $W = 0.4\,\mu m$. Optical microscope images of a fabricated antenna array and a SEM detail of a single antenna are shown in Figure 9.8.

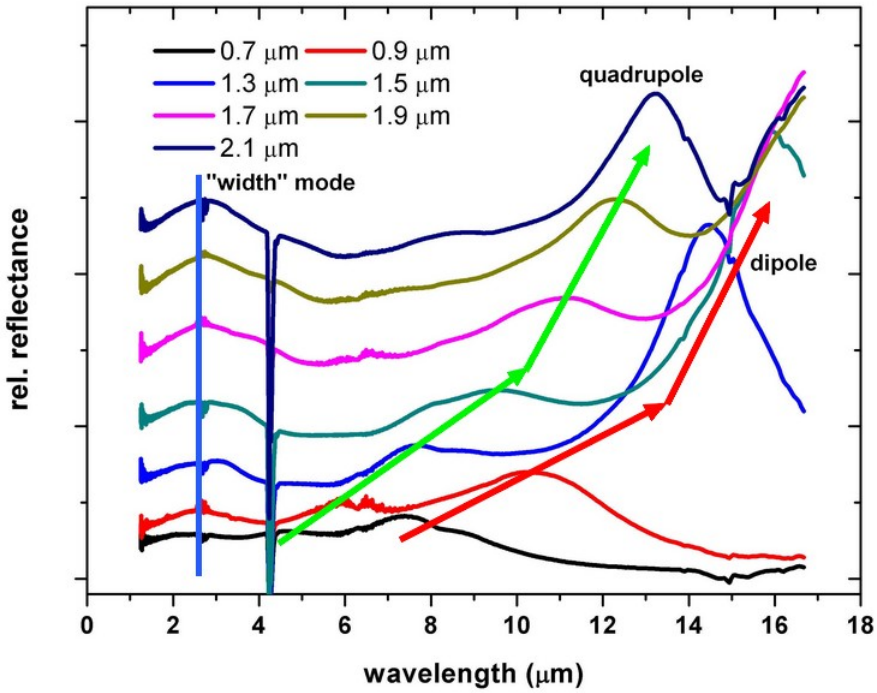

Figure 9.9: Experimental resonant spectra of gold V-antennas of various lengths (width $0.4\,\mu m$, height $0.06\,\mu m$) on a silicon substrate. The green and red arrows indicate the shift of the quadrupole and dipole antenna mode with the antenna length, respectively. As the antennas are relatively wide and a source of unpolarized light is used, the transverse resonant mode of the antenna is also visible at approximately $2.7\,\mu m$.

The mid-IR optical response of fabricated V-antenna arrays was measured by micro-FTIR (Bruker Vertex 80v + Hyperion 3000) in conventional reflection setup (Globar source of unpolarized IR radiation, Ge on KBr beamsplitter, MCT detector). The experimental resonant spectra of gold V-antennas on Si substrate are shown in Figure 9.9. In this figure, the red-shift of resonant wavelength with increasing arm length is indicated by arrows for both for dipole and quadrupole mode. As the width of the antennas is quite large, transverse *width* resonant mode is also visible in spectra. The intensity of the quadrupole-mode signal is very weak, this is especially apparent for antenna of length $1.3\,\mu m$, where the intensity of dipole and quadrupole peak can be directly compared.

The weak signal from quadrupole mode of antenna on silicon substrate is mainly caused by high reflectance of silicon substrate. Due to its high refractive index ($n \approx 3.42$ in mid-IR) silicon is relatively good reflector (see Section 6.3.1). Therefore, the presence of gold antennas on its surface enhance the reflectance only marginally. The solution of this issue consists in the change of the substrate.

Calcium fluoride (CaF_2) represents an ideal substrate for the detection of antenna quadrupole modes. Its low refraction index (n varies from 1.33 to 1.42 in mid-IR) makes it a bad

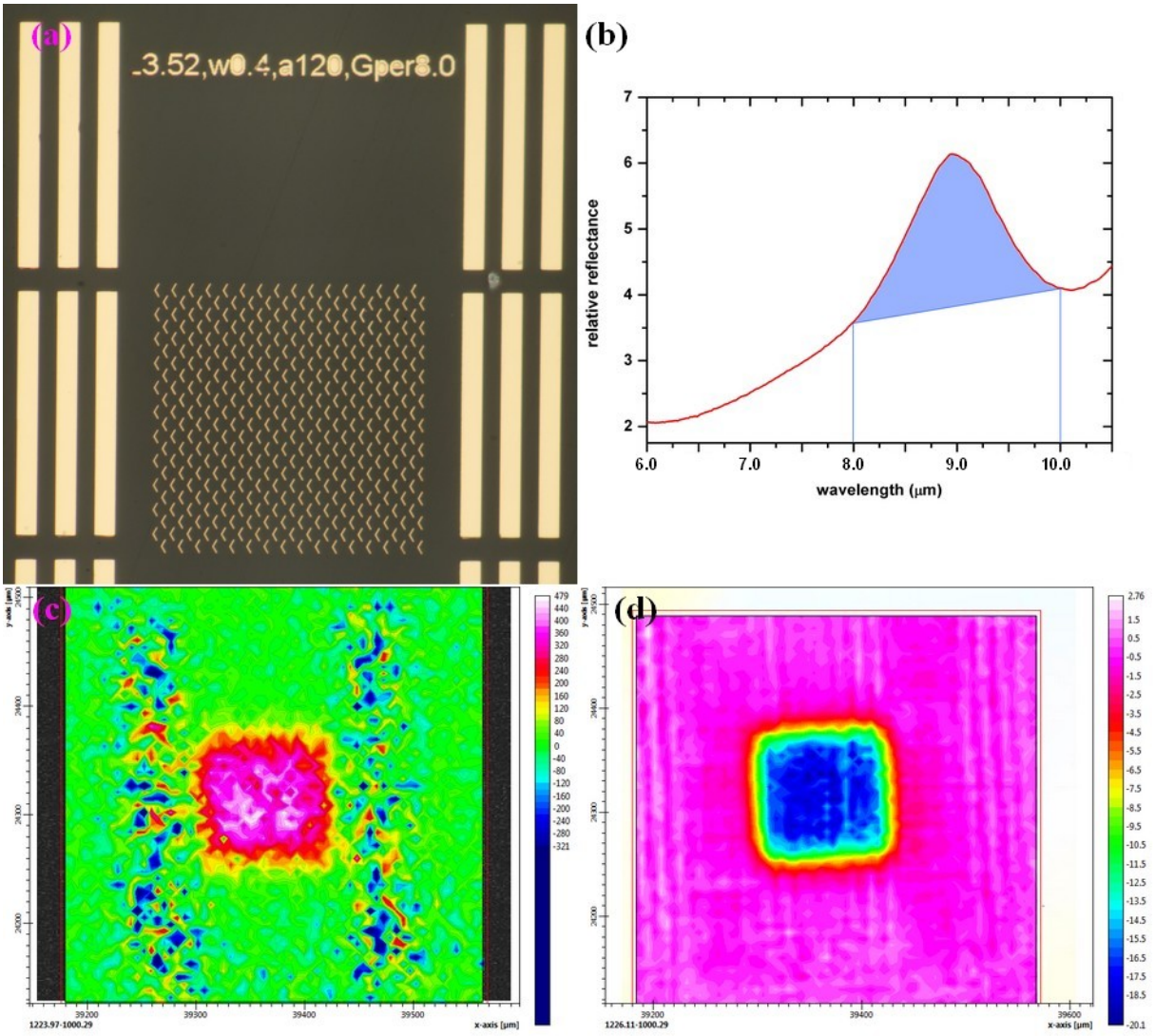

Figure 9.10: (a) Bright field microscope (Olympus MX51) image of a fabricated array of V-shaped antennas ($L = 3.52\,\mu$m) on the CaF_2 substrate. (b) Part of the experimental reflectance spectra of the array showing the peak of the antenna quadrupole mode, as recorded by an integral MCT detector. The blue area from 8 to 10 μm marks the integration range in the map of signal intensity for the quadrupole peak recorded by the focal plane array (FPA) detector of micro-FTIR in the reflection (c) and transmission configuration (d).

reflector. Due to the same reason, the antennas of the same resonant wavelength as their counterparts on silicon have to be longer. And longer antennas mean another increase of detected signal. A relative reflectance spectrum of gold antenna ($L = 3.52\,\mu$m) on CaF_2 substrate with clearly visible peak of quadrupole mode is shown in Figure 9.10b.

Consequently, we replaced the FTIR MCT detector with focal plane array (FPA) detector which is capable of sample mapping. After the measurements of antenna array response by FPA detector in both the reflection and transmission configuration we processed the recorded data and generate maps (Figure 9.10c,d) showing the area under the quadrupole peak corrected on baseline. The integration interval employed in the map generation

process was from 8 to 10 μm (Figure 9.10b). High intensity of the quadrupole peak makes the antenna array clearly visible in both maps.

These maps has given us an idea on the experimental determination of the directivity of the fabricated antenna arrays. A substrate of calcium fluoride will be covered with a thin film of higher refraction index. This film will act as multimode planar waveguide (similarly to silicon nitride in Section 9.1). V-shaped antennas fabricated on top of the planar waveguide will couple the incoming light into the waveguide and grating outcouplers, tuned for the wavelength, where the directivity of the antenna is the biggest (will be numerically calculated), will be fabricated all around the antenna array. The gratings will outcouple the scattered light from the planar waveguide and direct it into the collection objective and FPA detector. This procedure should enable us do directly map the planar radiation pattern of antenna arrays.

Chapter conclusion

Our theoretical and experimental studies showed that shape of plasmonic V-antenna causes the directional scattering of incoming light. The directional effects of scattering are the most pronounced at the spectral region close to the quadrupole plasmon resonance. Simulations run in Lumerical FDTD Solutions showed that the directivity of the narrow V-shaped antenna reaches up to 10 dB. As the antennas became wider, their directivity drops. Nevertheless, the directivity of V-antenna of width 0.4 μm is still approximately 5 dB.

In the first part of this chapter, the author showed the application of V-antenna in directional coupling of incident light into waveguide. Although the coupling was successful, the presented method for the assessment of its directionality showed to be very time consuming and impractical.

Based on the recorded maps shown in Figure 9.10c,d, the author proposes an experiment how to determine the directivity of V-shape antenna arrays in mid-IR using FTIR microspectrometer with focal plane array (FPA) detector capable of sample mapping. The main principle of the experiment represents the fabrication of metallic gratings, all around the antenna arrays. These gratings should *redirect* the light scattered by the antenna arrays out of the sample, ideally straight into the detector.

10 Conclusion

In this thesis, the resonant properties of plasmonic antennas were studied both theoretically and experimentally. Theoretical calculations were performed in the Lumerical FDTD Solutions software employing the finite-difference time-domain numerical method. For the measurements, antennas were fabricated by electron beam lithography. The resonant properties of fabricated antennas were studied mainly by Fourier transform infrared spectroscopy. In this thesis, three topics were studied. The first study was devoted to the resonant properties of gold plasmonic antennas situated on a nanocrystalline diamond film. The second one deals with the application of gold plasmonic antennas on a silicon substrate as a plasmon based sensor of streptavidin. Finally, the emission directivity of V-shaped antenna quadrupole mode was investigated.

Resonant properties of gold plasmonic antennas situated on the nanocrystalline diamond film were investigated in the near-infrared region. The samples consisted of a glass substrate, gold antennas, and several configurations of the nanocrystalline diamond layers or segments. The results can be summarized in the following way. Due to the higher refractive index of nanocrystalline diamond, the resonances of the antennas with diamond are red-shifted with respect to the case of the bare glass substrate. The red-shift is accompanied by the lower values of the antenna scattering cross section. The decrease in the scattering cross section can be partly negated by an appropriate tuning of the nanocrystalline diamond film thickness. The largest enhancement of the near field was obtained for a configuration with the antenna on a diamond film. The near-field is also more confined to the antenna-diamond interface and its decay from the boundary is faster than in the case of the antenna-glass interface. Preliminary results on this topic were presented by the author in the form of poster at Diamond 2011, International Conference on Diamond and Carbon Materials in September 2011 and at NFO 12, Near Field Optics conference in September 2012. Soon, a paper on this topic will be submitted to a peer-reviewed journal.

In the second study we have demonstrated that the plasmonic antennas are sensitive to the optical properties of their surroundings. The resonant wavelength of fabricated antenna arrays shifted in the presence of a single layer of self-assembled molecules and even in the presence of a single atomic layer of graphene. However, the measured shifts of the resonant wavelength are very small and more sensitive techniques have been presented in literature. Therefore, our technique requires significant improvements to become more practical. Nevertheless, our results in the field of biosensing were presented by the author in the form of oral contribution at IVC 19, International Vacuum Congress in September 2013.

Our simulations of V-shaped antennas have demonstrated highly directional scattering of light at the wavelengths close to the antenna quadrupole mode. In the experimental part of the study we have shown that these V-antennas can be used as directional couplers for coupling the incoming light into waveguides. In such configuration, we achieved the antenna directivity up to 7 dB in the near-infrared spectral region. Theoretical investigation of V-antenna directivity in the mid-infrared region has shown that for the narrow V-antennas their directivity reaches approximately 10 dB and drops with an increasing antenna width. We have also shown that a careful selection of the substrate can increase

the signal detected from the antenna quadrupole mode and facilitate its experimental detection.

In the present day, the author of this thesis continues in his work on the V-shaped antennas, where the experimental confirmation of V-antenna directional scattering in the mid-infrared using the FPA mapping detector of FTIR is his nearest goal.

References

[1] SOMMERFELD, A. Über die Ausbreitung der Wellen in der drahtlosen Telegraphie. *Ann. Phys.* 1909, vol. 333, iss. 4, 665–736.

[2] ZENNECK, J. Über die Fortpflanzung ebener elektromagnetischer Wellen längs einer ebenen Leiterfläche und ihre Beziehung zur drahtlosen Telegraphie. *Ann. Phys.* 1907, vol. 328, iss. 10, 846–866.

[3] WOOD, R. W. On a Remarkable Case of Uneven Distribution of Light in a Diffraction Grating Spectrum. *Proc. Phys. Soc. London*, 1902, vol. 18, 269–275.

[4] FANO, U. The Theory of Anomalous Diffraction Gratings and of Quasi-Stationary Waves on Metallic Surfaces (Sommerfeld's Waves). *J. Opt. Soc. Am.* 1941, vol. 31, 213–222.

[5] RITCHIE, R. H. Plasma Losses by Fast Electrons in Thin Films. *Phys. Rev.*, 1957, vol. 106, iss. 5, 874–881.

[6] RITCHIE, R. H., ARAKAWA, E. T., COWAN, J. J. et al. Surface-Plasmon Resonance Effect in Grating Diffraction. *Phys. Rev. Lett.*, 1968, vol. 21, iss. 22, 1530–1533.

[7] KRETSCHMANN, E., RAETHER, H. Radiative decay of non-radiative surface plasmons excited by light. *Z. Naturforchung.* 1968, vol. 23A, 2135–2136.

[8] OTTO, A. Excitation of nonradiative surface plasma waves in silver by the method of frustrated total reflection. *Z. Physik* 1968, vol. 216, iss. 4, 398–410.

[9] NOVOTNY, L. The History of Near-field Optics. In *Progress in Optics*, vol. 50. Amsterdam: Elsevier, 2007. ISBN 978-0-444-53023-3. Chapter 5, p. 137–184.

[10] MIE, G. Beiträge zur Optik trüber Medien, speziell kolloidaler Metallösungen. *Ann. Phys. (Berlin)*, 1908, vol. 330, no. 3, 377–445.

[11] HORVATH, H. Gustav Mie and the scattering an absorption of light particles: Historic developments and basics. *J. Quant. Spectrosc. Radiat. Transf.*, 2009, vol. 110, 787–799.

[12] BOHREN, C. F., HUFFMAN, D. R. *Absorption and scattering of light by small particles.* New York: Wiley, 1983, 530 p., ISBN 04-710-5772-X.

[13] JACKSON, J. D. *Classical electrodynamics.* 3rd ed. New York: Wiley, 1999, 808 p. ISBN 04-713-0932-X.

[14] KOMRSKA, J. *Fourierovské metody v teorii difrakce a ve strukturní analýze.* Skriptum VUT. Brno: CERM, 2007. 242 p. ISBN 978-80-214-3532-2.

[15] MAIER, S. A. *Plasmonics: Fundamentals and Applications*, 1st ed., New York: Springer, 2007. 224 p. ISBN 987-0-387-37825-1.

[16] SCHMIDT, E. et al. *Optické vlastnosti pevných látek.* Praha: SPN, 1986. 200 p.

[17] DRUDE, P. Zur Elektronentheorie der Metalle. *Ann. Phys. (Berlin)*, 1900, vol. 306, 566–613.

[18] LORENTZ, H. A. *The theory of electrons and it applications to the phenomena of light and radiant heat: A course of lectures delivered in Columbia University, New York, in March and April 1906.* 2nd ed., Leipzig: Teubner., 1916. 343 p.

[19] KITTEL, C. *Introduction to Solid State Physics*. New York: John Wiley & Sons, 1996. 665 p. ISBN 0-471-11181-3.

[20] HU, Z. G. et al. Optical properties of nanocrystalline diamond films from mid-infrared to ultraviolet using reflectometry and ellipsometry. *J. Mater. Sci.: Mater. Electron*, 2007, vol. 18, S37–S41.

[21] BARNES, W. L., DEREUX, A., EBBESEN, T. W. Surface plasmon subwavelength optics. *Nature*, 2003, vol. 424, , 824–830.

[22] BERINI, P. Long-range surface plasmon polaritons. *Adv. Opt. Photonics*, 2009, vol. 1, 484-588.

[23] CROZIER, K. B. et al. Optical antennas: Resonators for local field enhancement, *J. Appl. Phys.*, 2003, vol. 94, p. 4632–4642.

[24] KEDEM, O., TESLER, A. B., VASKEVICH A. et al: Sensitivity and Optimization of Localized Surface Plasmon Resonance Transducers. *ACS Nano* 2011, 5, 748–760.

[25] LI, J., YE, J., CHENM C. et al. Biosensing Using Diffractively Coupled Plasmonic Crystals: the Figure of Merit Revisited. *Adv. Optical Mater.* 2015, 3, 176–181.

[26] MÜHLSCHLEGEL, P. et al. Resonant optical Antennas. *Science*, 2005, vol. 308, 11607–11609.

[27] BHARADWAJ, P., DEUTSCH, B., NOVOTNY, L. Optical Antennas. *Adv. Opt. Photonics* 2009, 1, 438–483.

[28] NOVOTNY, L., HULST, N. v. Antennas for light. *Nature Photonics* 2011, vol.5, 83–90.

[29] BIAGIONO, P., HUANG, J., HECHT, B. Nanoantennas for visible and infrared radiation. *Rep. Prog. Phys.* 2012, vol. 75, 024402.

[30] TAUBNER, T., KEILMANN, F., HILLENBRAND, R. Nanoscale-resolved subsurface imaging by scattering-type near-field optical microscopy. *Opt. Express* 2005, vol 13, no. 22., 8893–8899.

[31] FARAHNI, J. N. et al. Bow-tie optical antenna probes for single-emitter scanning near-field optical microscopy. *Nanotechnology*, 2007, vol. 18, 125506.

[32] WANG, L., XU, X. High transmission nanoscale bowtie-shaped aperture probe for near-field optical imaging. *Appl. Phys. Lett.*, 2007, vol. 90, 261105.

[33] MOSKOVITS, M. Surface-enhanced Raman spectroscopy: a brief retrospective. *J. Raman Spectrosc.*, 2005, vol. 36, 485–496.

[34] BANHOLZER, M. J., MILLSTONE, J. E., QIN, L. et al. Rationally designed nanostructures for surface-enhanced Raman spectroscopy. *Chem. Soc. Rev.*, 2008, vol. 37, 885–897.

[35] LE, F. et al. Metallic Nanoparticle Arrays: A Common Substrate for Both Surface-Enhanced Raman Scattering and Surface-Enhanced Infrared Absorption. *ACS Nano*, 2008, vol. 2, No. 4, 707–718.

[36] STÖCKLE, R. M. et al. Nanoscale chemical analysis by tip-enhanced Raman spectroscopy *Chem. Phys. Lett.* 2000, vol. 318, 131–136.

[37] ADATO, R., ALTUG, H. In-situ ultra-sensitive infrared absorption spectroscopy of biomolecule interactions in real time with plasmonic nanoantennas. *Nat. Commun.*, 2013, vol. 4, 2154.

[38] NEUBRECH, F., PUCCI A., CORNELIUS, T. W. et al. Resonant Plasmonic and Vibrational Coupling in a Tailored Nanoantenna for Infrared Detection. *Phys. Rev. Lett.*, 2008, vol. 101, 157403.

[39] MAYER, K. M., HAFNER, J. H. Localized Surface Plasmon Resonance Sensors. *Chem. Rev.* 2011, vol. 111, 3828–3857.

[40] LIU, N. et al. Infrared Perfect Absorber and Its Application as Plasmonic Sensor. *Nano Lett.*, 2010, vol. 10, 2342–2348.

[41] SHEGAI, T. et al. Directional Scattering and Hydrogen Sensing by Bimetallic Pd-Au Nanoantennas. *Nano Lett.*, 2012, vol. 12, 2464–2469.

[42] ATWATER, H., POLMAN, A. Plasmonics for improved photovoltaic devices. *Nat. Mater.*, 2010, vol. 9, 205–213.

[43] DERKACS, D. et al. Improved performance of amorphous silicon solar cells via scattering from surface plasmon polaritons in nearby metallic nanoparticles. *Appl. Phys. Lett.*, 2006, vol. 89, 093103.

[44] CHOULIS, S. A., MATHAI, M. K., CHOONG, V. Influence of metallic nanoparticles on the performance of organic electrophosphorescence devices. *Appl. Phys. Lett.*, 2006, vol. 88, 213503.

[45] CUBUKCU, E. et al. Plasmonic laser antenna. *Appl. Phys. Lett.*, 2006, 89, 093120.

[46] OKAMOTO, K. et al. Surface-plasmon-enhanced light emitters based on InGaN quantum wells. *Nat. Mater.*, 2004, vol. 3, 601–605.

[47] ARANGO, B. F., KWADRIN, A., KOENDERINK, A. F. Plasmonic Antennas Hybridized with Dielectric Waveguides. *ACS Nano*, 2012, vol. 6, no. 11, 10156–10167.

[48] FÉVRIER, M. et al. Giant Coupling Effect between Metal Nanoparticle Chain and Optical Waveguide. *Nano Lett.*, 2012, vol. 12, 1032–1037.

[49] MERTENS, H., KOENDERINK, A. F., POLMAN A. Plasmon-enhanced luminescence near noble-metal nanospheres: Comparison of exact theory and an improved Gersten and Nitzan model. *Phys. Rev. B* 2007, vol. 76, 115123.

[50] NOVOTNY, L., BIAN, R. X., XIE X. S. Theory of Nanometric Optical Tweezers. *Phys. Rev. Lett.* 1997, vol. 79, 645–648.

[51] RIGHINI, M. et al. Parallel and selective trapping in a patterned plasmonic landscape. *Nature Physics* 2007, vol. 3, 477–480.

[52] HUANG, X., et al. The Potential Use of the Enhanced NonlinearProperties of Gold Nanospheres in Photothermal Cancer Therapy. *Lasers Surg. Med.* 2007, vol. 39, 747–753.

[53] NOVOTNY, L. Effective Wavelength Scaling for Optical Antennas. *Phys. Rev. Lett.*, 2007, vol. 98, 266802.

[54] KALOUSEK R. et al: Response of plasmonic resonant nanorods: an analytical approach to optical antennas. *Opt. Express*, 2012, vol. 20, no.16, 17916–17927.

[55] TAMINIAU, T. H., STEFANI, F. D., van HULST, N. F. Enhanced directional excitation and emission of single emitters by a nano-optical Yagi-Uda antenna, *Opt. express*, 2008, vol. 16, no. 14, p. 16858–16866.

[56] HOFMANN, H.F., KOSAKO, T., KADOYA, Y. Design parametres for a nano-optical Yagi-Uda antenna. *New J. Phys.*, 2007, vol. 9, 217.

[57] MAKSYMOV, I. S. et al. Optical Yagi-Uda nanoantennas. *Nanophotonics*, 2012, vol. 1, p. 65–81.

[58] *FDTD - The Yee Cell* [online]. [cit. 2015-09-27]. <http://fdtd.wikispaces.com/The+Yee+Cell>.

[59] TAFLOVE, A. Application of the Finite-difference time-domain method to sinusoidal steady state electromagnetic penetration problems. *IEEE Trans. Electromagn. Compat.*, 1980, vol. 22, no. 3, 191–202.

[60] YEE, K. S. Numerical Solution of the initial boundary value Problems involving Maxwell's equation in isotropic Media. *IEEE Trans. Antennas. Propag.* 1966, AP-14, 302–307.

[61] WARD, D. W., NELSON, K. A. Finite-Difference Time-Domain (FDTD) Simulations of Electromagnetic Wave Propagation Using a Spreadsheet. *Comput. Appl. Eng. Educ.*, 2005, vol. 13, 213–221.

[62] KUNZ, K. S., LUEBBERS, R. J. *Finite Difference Time Domain Method for Electrodynamics*. Boca Raton: CRC press, 1993. 433 p. ISBN 0-8493-8657-8.

[63] *Lumerical Knowledge Base* [online]. Lumerical Solutions, Inc. ©2003-2015, [cit. 2015-09-13]. <http://docs.lumerical.com/en/index.html>.

[64] *FDTD Solutions* [online]. Lumerical Solutions, Inc. ©2003-2015, [cit. 2015-09-12]. <http://www.lumerical.com/tcad-products/fdtd>.

[65] *Maxima, a Computer Algebra System* [online]. Version 5.23.2 ©2004-2010, [cit. 2015-09-29]. <http://maxima.sourceforge.net>

[66] SCHNEIDER, J. B., ABDIJALILOV, K. Analytic Field Propagation TFSF Boundary for FDTD Problems Involving Planar Interfaces: PECs, TE, and TM. *IEEE Trans. Antennas. Propag.* 2006, vol. 54, iss. 9, 2531–2542.

[67] LIŠKOVÁ, Z. *Tvorba nanostruktur a nanosoučástek pro oblast nanoelektroniky a spintroniky, výzkum jejich transportních vlastností.* Brno: Brno University of Technology, Faculty of Mechanical Engineering, Institute of Physical Engineering, 2013. Treatise to state doctoral exam.

[68] PARIKH, M. Corrections to proximity effects in electron beam lithography: I. Theory. *J. Appl. Phys.*, 1979, 50, 4371–4377.

[69] *NANO™ PMMA and Copolymer* [online]. Microchem Corporation, ©2001, [cit. 2015-09-27]. <http://microchem.com/pdf/PMMA_Data_Sheet.pdf>.

[70] STUART, B. *Infrared Spectroscopy: Fundamentals and Applications.* Hoboken: John Wiley & Sons, 2004, 224 p. ISBN 0-470-85428-6. Chapter 2, p. 15–24.

[71] YAGGI, N., VIJ, D.J. Fourier transform infrared spectroscopy. In *Handbook of Applied Solid State Spectroscopy.* New York: Springer, 2006, 741 p., ISBN 987-0-387-32497-5. Chapter 9, p. 410–450.

[72] DELEPORTE, T. *Quantitative infrared Fourier transform spectroscopy: Absolute line intensities for $^{13}CO_2$ and HOBr.* Brussels: Université Libre de Bruxelles, Faculté des Sciences, Département de Physique. Dissertation thesis. Chapter 2, 27–46.

[73] EDWARDS D. F. Silicon (Si). In *Handbook of optical constants of solids*, vol. 1., PALIK, E. D., San Diego, Academic Press, 1998. ISBN 0-12-544420-6. Part II: Critiques, subpart 2: Semiconductors, p. 547–570.

[74] *Silicon (Si) Optical Material* [online]. Crystran Ltd, ©2012, [cit. 2014-06-14]. <http://www.crystran.co.uk/optical-materials/silicon-si>.

[75] MITURA, S. et al. Nanocrystalline diamond, its synthesis, properties and applications. *J. Achiev. Mat. Manuf. Eng.*, 2006, vol. 16, no. 1–2, 9–16.

[76] WILLIAMS, O. A., NESLÁDEK, M. Growth and properties of nanocrystalline diamond films. *Phys. Stat. Sol. A*, 2006, vol. 203, no. 13, 3375–3386.

[77] *Diamond Optical Material* [online]. Crystran Ltd, ©2012, [cit. 2014-06-14]. <http://www.crystran.co.uk/optical-materials/diamond-cubic-carbon-c>.

[78] EDWARDS D. F., PHILIPP, H. R. Cubic Carbon (Diamond). In *Handbook of optical constants of solids*, vol. 1., PALIK, E. D., San Diego, Academic Press, 1998. ISBN 0-12-544420-6. Part II: Critiques, subpart 3: Insulators, p. 665–675.

[79] KROMKA, A. et al. Early stage of diamond growth at low temperature. *Diam. Rel. Mat.*, 2008, vol. 17, 1252–1255.

[80] *Calcium Fluoride Optical Material* [online]. Crystran Ltd, ©2012, [cit. 2014-06-30]. <http://www.crystran.co.uk/optical-materials/calcium-fluoride-caf2>.

[81] BEZUIDENHOUT, D. F. Calcium Fluoride (CaF_2). In *Handbook of optical constants of solids*, vol. 2., PALIK, E. D., San Diego, Academic Press, 1998. ISBN 0-12-544422-2. Part II: Critiques, subpart 3: Insulators, p. 815–836.

[82] PALIK, E. D. *Handbook of optical constants of solids*. vol. 1. San Diego: Academic Press, 1998. 804 p. ISBN 0-12-544420-6.

[83] WEBER, J. M. *Handbook of Optical Materials*. Boca Raton: CRC press, 2003, 512 p. ISBN 0-8493-3512-4.

[84] MAIER, S. A., KIK, P. G., ATWATER, H. A. Obseravation of coupled plasmon-polariton modes in Au nanoparticle chain waveguides of different lengths: Estimation of waveguide loss. *Appl. Phys. Lett.*, 2002, vol. 81 , 1714–1716.

[85] LLOYD, G. E. Atomic number and crystallographic contrast images with the SEM: a review of backscattered electron techniques. *Mineral. Mag.*, 1987, vol. 51, 3–19.

[86] MASS, T. W. W., TAUBNER, T. Incident Angle-Tuning of Infrared Antenna Array Resonances for Molecular Sensing. *ACS Photonics*, 2015, Article ASAP, DOI:10.1021/acsphotonics.5b00399.

[87] LUO, D. The road from biology to material. *Mater. Today*, 2003, vol. 6, no. 11., 38–43.

[88] CHENG, W. L. et al. Bio-Mediated Assembly of Ordered Nanoparticle Superstructures. In *Handbook of nanofabrication*. 1st ed. Amsterdam: Elsevier, 2010, 310 p. ISBN 978-0-12-375176-8. Chapter 2, p. 57–90.

[89] LIU, G., XU, S., QIAN, Y. Nanofabrication of Self-Assembled Monolayers Using Scanning Probe Lithography. *Acc. Chem. Res.*, 2000, vol. 33, 457–466.

[90] MALARD, L. M., PIMENTA, M. A., DRESSELHAUS, G. et al. Raman spectroscopy in graphene *Phys. Rep.*, 2009, vol. 473, 51–87.

[91] VERCRUYSSE, D. et al. Unidirectional Side Scattering of Light by a Single-Element Nanoantenna. *Nano Lett.*, 2013, vol. 13, 3843–3849.

[92] BALANIS, C. A. *Antenna Theory: Analysis and Design.* Hoboken: John Wiley & Sons, 2005. 1050 p. ISBN 0-471-66782-X.

[93] VERCRUYSSE, D. et al. Directional Fluorescence Emission by Individual V-Antennas Explained by Mode Expansion. *ACS Nano*, 2014, vol. 8, 8232–8241.

[94] FORMANOVÁ, V. *Směrové plazmonické antény*. Brno: Brno University of Technology, Faculty of Mechanical Engineering, Institute of Physical Engineering, 2015. 44 p. Supervisor Michal Kvapil.

List of abbreviations

AFM	atomic force microscopy
BSE	backscattered electrons
CF5	coagulation factor 5
CW	continuous wave
DeMi	demineralized
FDTD	finite-difference time-domain
FPA	focal plane array
HSQ	hydrogen silsesquioxane
IBAD	ion beam assisted deposition
ICP/RIE	inductive coupled plasma reactive ion etching
InGaAs	indium-gallium-arsenide
IPA	isopropanol
IPE BUT	Institute of Physical Engineering, Brno University of Technology
IR	infrared
KK	Kramers-Kronig
LN_2	liquid nitrogen
LSP	localized surface plasmon, localized surface plasmon polariton
LSPR	localized surface plasmon resonance
MCC	MicroChem
MCT	mercury-cadmium-telluride
MIBK	methyl isobutyl ketone
mid-IR	middle infrared, mid-infrared
NCD	nanocrystalinne diamond
NIR	near-infrared
PBS	phosphate-buffered saline
PMMA	poly(methyl methacrylate)
OPD	optical path difference

sccm	standard cubic centimeter
SE	secondary electrons
SEM	scanning electron microscope
SEIRA	surface enhanced infrared absorption spectroscopy
SEIRS	surface enhanced infrared spectroscopy
SERS	surface enhanced raman spectroscopy
SPP	surface plasmon polariton
ss	single strand
TE	transverse electric
TOEG6	ethylene-glycol-terminated alkylthiol, (11-Mercaptoundecyl)hexa(ethylene glycol)
TFSF	total-field scattered-field
TM	transverse magnetic
VIS	visible